

**Instrumentation for Multiaxial Mechanical Testing
of Inhomogeneous Elastic Membranes**

by

Ariel Marc Herrmann

B.S., Mechanical Engineering (2002)
Stanford University

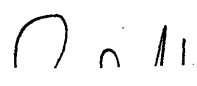

Submitted to the Department of Mechanical Engineering
in partial fulfillment of the requirements for the degree of
Master of Science in Mechanical Engineering

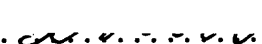
at the

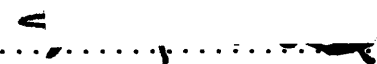
MASSACHUSETTS INSTITUTE OF TECHNOLOGY

February 2006

© Massachusetts Institute of Technology 2006. All rights reserved.

Author 
Department of Mechanical Engineering
 14 January 2006

Certified by 
Ian W. Hunter
Hatsopoulos Professor of Mechanical Engineering
Professor of Bioengineering
Thesis Supervisor

Accepted by 
Lallit Anand
Chairman, Department Committee on Graduate Students

Instrumentation for Multiaxial Mechanical Testing of Inhomogeneous Elastic Membranes

by

Ariel Marc Herrmann

Submitted to the Department of Mechanical Engineering
on 14 January 2006, in partial fulfillment of the
requirements for the degree of
Master of Science in Mechanical Engineering

Abstract

This thesis presents the design, development, and construction of an instrument for biaxial mechanical testing of inhomogeneous elastic membranes. The instrument incorporates an arrangement of linear motion stages for applying arbitrary deformation profiles on the material under test, purpose-built two-axis force transducers for high-resolution measurement of applied loads, and a digital imaging system for full-field strain measurement. The components described herein provide the foundation for a sophisticated biaxial testing platform for determining the mechanical properties of anisotropic, inhomogeneous membrane materials.

Thesis Supervisor: Ian W. Hunter

Title: Hatsopoulos Professor of Mechanical Engineering

Professor of Bioengineering

Acknowledgments

This thesis and the work that I have undertaken received support of many kinds and from many corners. I am grateful to all those who helped along the way and contributed to a learning experience without compare.

I thank my colleagues in the Bioinstrumentation lab and beyond for their support in every aspect of my work. Their willingness to lend a hand at any hour and under any circumstance has been amazing, and they have contributed volumes to my knowledge, understanding, and abilities.

I thank my advisor, Prof. Ian Hunter, for extending the invitation to work in the Bioinstrumentation lab, and for his abundant patience and confidence. The resources in the lab are truly astounding, and I am grateful that I have had the opportunity to make use of even the smallest portion while enriching myself and furthering my work.

I thank the administrative staff of the Mechanical Engineering department, the Institute, and the Bioinstrumentation lab, for their help in keeping track of all the details while navigating along my path.

I thank the administrators and supporters of the National Defense Science and Engineering Graduate Fellowship program, which made my research and education possible. The fellowship provided substantial support and personal and academic freedom for the first years of my work, and while the generosity of my sponsors may have helped extend my term as a Master's student, I have been fortunate to enjoy many incomparable experiences in its course.

I thank all the members of the MIT Cycling Team, for providing a great share of those incomparable experiences. It has been great to watch the team grow, to contribute to and share in some outstanding accomplishments, and to forge strong bonds and close friendships along the way.

Finally, I thank my family. My parents have instilled in me a love of learning, and from early on have shown unwavering confidence in all of my pursuits and decisions. My brother and they have always been open to discuss the big pictures and the smallest details of work and life.

Contents

1	Introduction	17
1.1	Mechanical testing of membrane materials	18
1.2	Approach and organization	19
2	Biaxial Material Testing	23
2.1	Membrane inflation method	23
2.2	Planar biaxial extension systems	26
2.2.1	Overview of prior work	26
2.2.2	Edge effects: attachment method and sample shape	29
2.3	Multiaxial multiple-1DOF-actuator systems	31
2.3.1	Charette / McGill system	31
2.3.2	Nielsen / Auckland system	32
3	Design Considerations	35
3.1	System concept	35
3.1.1	Flexible loading schemes	36
3.1.2	Full-field analysis	39
3.2	Instrumentation components and parameters	39
3.2.1	Actuator system	40
3.2.2	Optical system	40
3.2.3	Force measurement system	41
3.2.4	Instrument control system	46

4	System Design and Implementation	47
4.1	System overview	47
4.2	Optical subsystem	49
4.3	Motion subsystem	50
4.3.1	Motion stage parameter tuning	51
4.4	Force transducers	53
4.4.1	Transducer mechanical design	53
4.4.2	Strain gage selection	55
4.4.3	Analytical and numerical modeling	56
4.4.4	Transducer construction details	60
4.4.5	Transducer electrical connections	63
4.5	Data acquisition hardware	64
4.6	Software and integration	66
5	Testing and Validation	67
5.1	Force transducer characterization	67
5.1.1	Calibration results: prototype transducer	69
5.1.2	Calibration details and results: Final transducers	72
5.2	Biaxial testing experiment	77
5.2.1	Equibiaxial testing: physical experiment	77
5.2.2	Finite element analysis	82
5.2.3	Experiment / analytical comparison	84
5.3	Finite element considerations	87
6	Conclusion and Further Work	89
6.1	Limitations	89
6.2	Extensions and future work	91
6.2.1	Full-field strain measurement	91
6.2.2	High-speed testing	91
6.2.3	Environmental control	91
6.2.4	Integrated modeling and testing	92

References	93
Appendix A Mechanical drawings	101
Appendix B Motion system control loop	107
Appendix C Transducer design calculations	111
Appendix D Transducer calibration details	113
D.1 Computation of the transformation matrix	114
D.2 Calibration data	115
Appendix E Camera system comparison	125
Appendix F Software code	127
F.1 Position transfer function computation	128

List of Figures

1-1	Multiaxial materials testing system	21
2-1	Membrane inflation testing apparatus	25
2-2	Planar biaxial testing apparatus for biomaterials testing	28
2-3	Planar biaxial testing apparatus for electroactive polymer films	29
2-4	Charette multiaxial materials testing system	31
2-5	Biaxial testing apparatus developed by Nielsen <i>et al.</i>	32
3-1	Sample deformations with existing biaxial material testing systems.	37
3-2	Sample deformations available with two degrees of freedom at each attachment point	38
3-3	Simple bending beam transducer schematic	43
3-4	Two-axis cantilever beam transducer schematic	45
4-1	System overview and connection schematic	48
4-2	Optical subsystem components	49
4-3	Aerotech ANT-25 linear motion stage	51
4-4	Effect of parameter tuning on linear motion system frequency response.	52
4-5	Force transducer assembly: exploded view.	54
4-6	Transducer finite element simulation: Axial strain and displacement.	59
4-7	Transducer finite element simulation: Stress and strain fields.	59
4-8	Force transducer body after CNC machining	61
4-9	Strain gage bonding fixture	62
4-10	Strain gage bonding results	63

4-11	Transducer with wiring and bridge completion resistor board mounted	64
4-12	Transducer assembly, signal conditioning hardware, and mechanical components mounted on motion stage	65
4-13	Control software user interface	66
5-1	Transducer calibration assembly schematic—prototype transducer. . .	68
5-2	Prototype transducer calibration: output versus load	70
5-3	Prototype transducer calibration: output versus angle	71
5-4	Transducer calibration assembly schematic—final transducer.	72
5-5	Final transducer calibration: output versus applied load, unit 1 . . .	74
5-6	Final transducer calibration: output versus applied load, unit 2 . . .	75
5-7	Final transducer calibration: in-plane response vector plot	76
5-8	Layout of initial biaxial testing experiment	78
5-9	Biaxial testing: Membrane images	79
5-10	Vector displacement of markers in biaxial extension test.	80
5-11	Biaxial testing: Experimental force data	81
5-12	Finite element model: mesh, loading, and deformation.	82
5-13	Finite element simulation results: Displacement magnitude field. . . .	83
5-14	Finite element simulation results: Stress and strain fields.	84
5-15	Comparison of displacement results from biaxial extension test and finite element model.	85
A-1	Mechanical drawing: transducer body	102
A-2	Mechanical drawing: pin holder	103
A-3	Mechanical drawing: pin holder collet	104
A-4	Mechanical drawing: transducer holder	105
A-5	Mechanical drawing: strain gage mounting jig	106
B-1	Motion stage control loop configuration detail	108
D-1	Calibration data details: transducer 1, output 1, X axis load.	116
D-2	Calibration data details: transducer 1, output 1, Y axis load.	117

D-3	Calibration data details: transducer 1, output 2, X axis load.	118
D-4	Calibration data details: transducer 1, output 2, Y axis load.	119
D-5	Calibration data details: transducer 2, output 1, X axis load.	120
D-6	Calibration data details: transducer 2, output 1, Y axis load.	121
D-7	Calibration data details: transducer 2, output 2, X axis load.	122
D-8	Calibration data details: transducer 2, output 2, Y axis load.	123

List of Tables

3.1	Commercial force transducer specifications.	42
4.1	Comparison of foil and semiconductor strain gage properties.	55
5.1	Transducer performance parameters: Sensitivity components for on- and off-axis loading, resulting sensitivity axis, and sampling noise. . .	76
5.2	Mooney-Rivlin material constants for natural latex rubber, computed from inflation testing data by separate groups.	83
5.3	Comparison of experimental data and finite element model predictions of reaction forces at material attachment points	86
B.1	Motion control servo loop parameters before and after tuning for im- proved dynamic performance	109
C.1	Transducer dimension calculations	112

Chapter 1

Introduction

Mechanical testing of materials aims to establish the relationship between imposed stress and the resulting deformation. Knowledge of the material parameters on the continuum level allows the engineer to predict the response of macroscopic structures to imposed loads, and thus provides a foundation for analysis of existing structures and for the design of new ones.

Whereas many classical engineering materials are generally well characterized by isotropic material laws and are used in homogeneous form as structural components, in biological materials inhomogeneous, anisotropic material properties are the rule, not the exception [1]. Even biological tissues that appear uniform on a macroscopic scale are typically inhomogeneous on the microscopic scale due to spatial variations in the distribution and cross-linking of the component collagen fibers [2], which in turn affect the local material properties. Therefore, more sophisticated material laws and testing methods to ascertain their form are required for the accurate description of biological materials.

Many classes of polymer materials exhibit similarly complex mechanical behavior that likewise places particular demands on testing methodology. Anisotropic mechanical properties in polymers may result from manufacturing and processing techniques that affect the material structure on a microscopic scale; the material and molecular orientation typically have a substantial influence on mechanical properties [3]. Molecular anisotropy in conducting polymer materials in particular arises due to the

physical orientation of the material during polymerization via electrochemical synthesis [4]. Highly orientation-dependent electrical properties are common, including huge variations of electrical conductivity (several orders of magnitude) between different orientations. Similar effects have been reported after creating anisotropy *via* plastic stretching of conducting polymer films [5]. Although reports of anisotropy in conducting polymers properties have focused largely on electrical properties, the unique synthesis conditions and processing that these materials undergo may likewise yield significant orientation- and position-dependent variations in their mechanical properties.

Given the complex mechanical properties that characterize biological tissues and many engineered polymers, multi-axial material characterization is a prerequisite for a wide range of applications: Accurate modeling is a requirement for understanding normal and pathological biological function, for designing medical interventions and biomimetic systems, and for engineering simulation. Appropriate testing techniques are required to to elicit, observe, and analyze the complex material responses to gain a complete understanding of the materials in question.

1.1 Mechanical testing of membrane materials

Whereas classical uniaxial mechanical testing suffices to characterize the properties of homogeneous, isotropic materials, biaxial testing is necessary to fully describe the properties of anisotropic materials. Uniaxial testing requires relatively long thin strips of material to ensure a true uniaxial stress field, which is not a practical means of evaluating properties at various orientations in a single potentially unique sample. To accurately evaluate biaxial mechanical properties, simultaneous loads and displacements in both axes in the plane must be measured.

Biaxial mechanical testing has been developed extensively in the past 30 years, primarily as a means for elucidating the complex mechanical properties of biological membranes. Initial reports of a testing system for the biaxial mechanical analysis of rabbit skin were made in 1974 [6, 7]; while the development of refinements to

the techniques, application of the data [8], and debate over experimental methods continues to this day [9, 10].

Typical biaxial mechanical testing schemes reported in the literature provide only limited insight into the behavior of materials with substantial inhomogeneities of internal structural or mechanical properties. Stress and strain measurements are estimates whose validity relies on the uniformity of material properties over the area of interest, and which cannot account for variations in structure or material properties within the sample area. To accurately analyze the response of inhomogeneous materials, full-field strain sampling and more sophisticated modeling techniques must be used [11, 12]. A refinement of the instrumentation for these techniques was the focus of the present work.

1.2 Approach and organization

This thesis presents the design, development, and construction of an instrument for biaxial mechanical testing of inhomogeneous elastic membranes. The basic requirements of the system were analyzed, component parts were selected, and testing was performed to qualify the performance of key components. To verify system functionality, a proof-of-concept mechanical test was performed and the results compared with a finite element simulation. The remainder of the thesis documents this work and proceeds as follows:

Chapter 2 provides an overview of existing biaxial materials testing techniques. A brief historical review is included, including the unique characteristics, insights gleaned from, and shortcomings of various previous work.

Chapter 3 describes in greater detail the concept for the present instrument. Requirements and design parameters for several key components are discussed.

Chapter 4 details the specific implementation of the present testing system, component-by-component. The manufacturing and assembly of a precision two-axis force transducer is described in detail.

Chapter 5 presents the results of system calibration and describes an initial biaxial testing experiment. A finite element model of the experiment is developed to provide a comparison for the experimental data, and the results of the simulation and physical experiment are compared.

Chapter 6 summarizes the present work and expands on future directions for developing and expanding the capabilities of the testing system described in this thesis.

For reference, an overview image of the completed testing system with major components highlighted is shown in Figure 1-1.

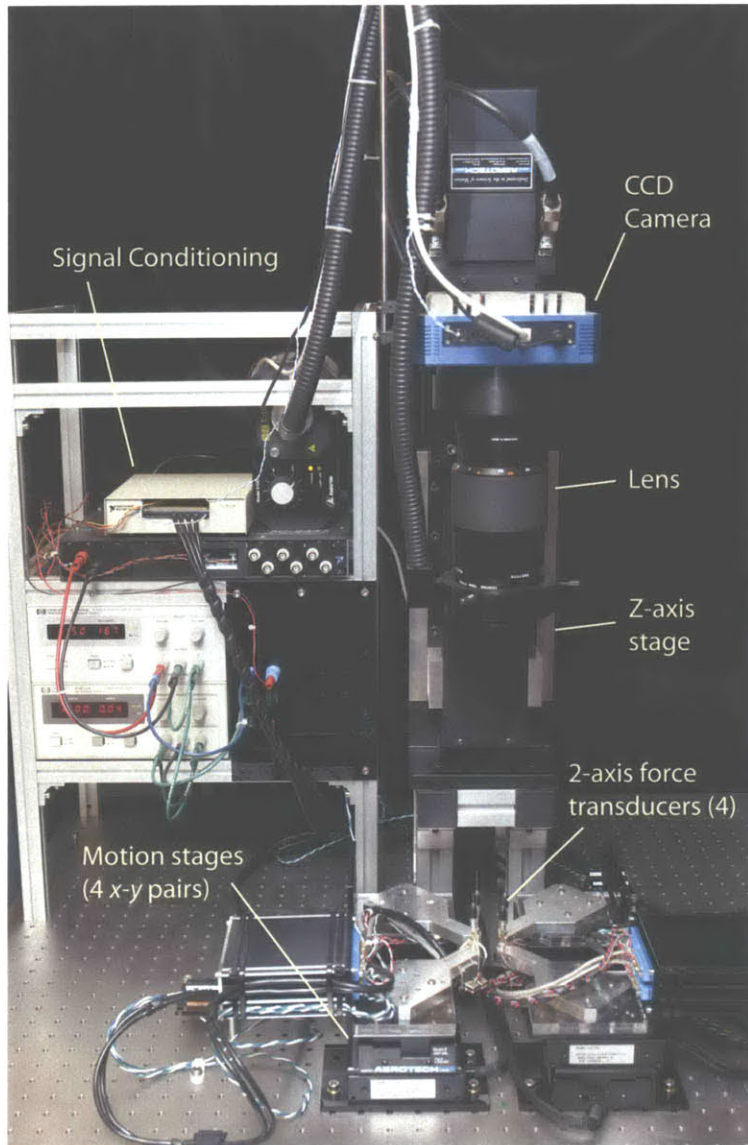


Figure 1-1. Multi-axial materials testing system hardware. Key components are labeled. (For a conceptual diagram, see Section 4.1.)

Chapter 2

Biaxial Material Testing

For incompressible materials, biaxial testing of thin membranes is sufficient to derive a general constitutive relationship: given two known principal strains, the orthogonal strain may be computed from the conservation of volume. The assumption of incompressibility is not valid for most engineering materials; however many biological materials are *nearly* incompressible to the extent that incompressibility is regularly assumed for modeling purposes. This simplification allows for the complete characterization of materials using biaxial testing, with only a 2D stress state imposed [13]. The assumption of incompressibility may introduce error when properties computed from 2D experiments are used for modeling thick structures; however, the testing protocols are substantially simplified and the results are fully valid for thin structures subject to loading analogous to that imposed in 2D tests.

A brief summary of past approaches to planar biaxial testing is presented below. Significant developments in testing instruments are introduced, and the limitations of these systems pointed out.

2.1 Membrane inflation method

Inflation testing has been used to determine material properties of elastomers and soft tissue biomaterials. Typically, a circular membrane is clamped in a device with a chamber that is pressurized on one side of the membrane. Deformation of the central

region of the specimen is measured by tracking markers on the specimen surface parallel to the plane of the specimen (potentially in two axes), from which the radius of curvature of the membrane under load may be estimated.

Given the known inflation pressure p and radii of curvature $R_{1,2}$, the components of stress ($\sigma_{1,2}$) in the plane of the membrane may be computed from the Laplace equation for an ellipsoid,

$$p = t_s \left(\frac{\sigma_1}{R_1} + \frac{\sigma_2}{R_2} \right). \quad (2.1)$$

The membrane thickness t_s in the deformed state is an unknown but for an incompressible material is simply related to the initial thickness of the membrane t_0 by the stretch ratio.¹ With no change in volume, $t_s = \frac{t_0}{\lambda_1 \lambda_2}$ for stretch ratios $\lambda_{1,2}$. Thus Equation 2.1 may be rewritten,

$$\frac{p \lambda_1 \lambda_2}{t_0} = \frac{\sigma_1}{R_1} + \frac{\sigma_2}{R_2}. \quad (2.2)$$

Pressure and initial thickness are controlled experimental data, and radius of curvature and stretch ratio are computed by measuring the deformed geometry, leaving only the stress terms to be computed. For an isotropic material, the stresses and stretch ratios in the two axes are equal, leaving only one in-plane stress term σ to be calculated directly.

Hildebrand *et al.* [16] used this method to test rubber and biological membranes in 1969. Further theoretical analysis was presented by Wineman *et al.* [17], who presented a theoretical framework for interpreting test results and suggested specific parameters for an experiment presented. The membrane inflation technique has been used subsequently for testing the strength and failure modes of blood vessels under quasi-static and dynamic loading conditions [18], and more recently to assess the mechanical properties of abdominal aortic aneurysm tissue [19].

In the scope of mechanical design, membrane inflation testing has been used for

¹The stretch ratio is a measure of deformation, defined as the ratio of deformed length to original length: $\lambda = l/l_0$. In large-deformation analysis, where the engineering strain, $\varepsilon = \Delta l/l = (l - l_0)/l$, becomes large, the stretch ratio is a more convenient quantity. For a detailed overview on the formulation of stress and strain measures with particular relevance to finite element methods see [14].

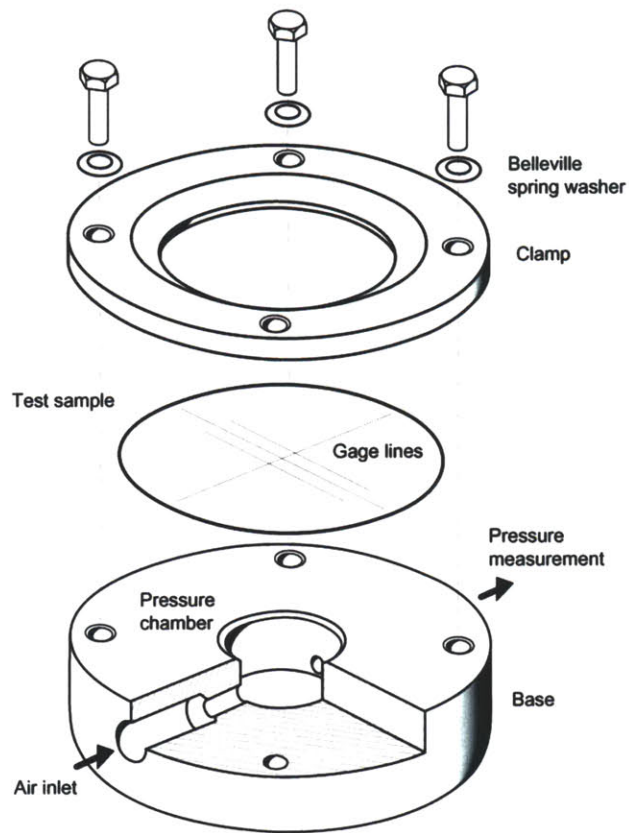


Figure 2-1. Schematic of membrane inflation testing apparatus (Image taken from Makino *et al.*[15])

characterization of natural rubber and a synthetic elastomer in the first step of a design study for pressure pads for microelectronics applications [15]. The experimental apparatus is shown in Figure 2-1. The length of the gage line in the center of the specimen was determined by measuring three-axis positions of three points along its length with a microscope. The inflation test data was used to define a finite element model, which was subsequently compared with experimental tests of another loading mode.

Membrane inflation has a number of attractive characteristics as a testing method: The apparatus and control required are relatively simple; it is easy to mount a specimen (provided that the area of tissue available and the size of the testing device are compatible) and to make geometric measurements at moderate stretch ratios ($\lambda \lesssim 2$); and the interpretation of data is straightforward. In addition, the technique allows for a wide range of applied strain rates, limited only by the capacity of the pressure control system and the measurement system used to determine the membrane curvature. However, it is limited to materials that are homogeneous and does not allow for independent control of the imposed load ratio between axes.

2.2 Planar biaxial extension systems

2.2.1 Overview of prior work

Biaxial mechanical testing of elastic membranes was pioneered in the context of rubber elasticity by Treloar [20] and Rivlin [21] in the middle of the last century. In parallel with experimental work, Rivlin developed a generalized strain energy formulation for rubber,

$$W = \sum_{i=0, j=0}^{\infty} C_{ij} (I_1 - 3)^i (I_2 - 3)^j, \quad C_{00} = 0, \quad (2.3)$$

where I_1 and I_2 are the first and second invariant measures of deformation which are uniquely defined by the deformation gradient \mathbf{X} . Limiting the number of terms in

the summation to n gives the n -term Mooney-Rivlin material constitutive relation;² this relation is used later in the present work in a finite-element model of a rubber membrane undergoing biaxial testing.

In general, biaxial mechanical testing seeks to determine the form and parameters that relate material strain response to the applied stresses. For conservative material laws (in which a single stress-strain curve holds for both increasing and decreasing stress, which requires, e.g., that plasticity effects be excluded) there exists a strain energy function $W = W(\mathbf{X})$, that completely describes the change in internal energy in a material due to applied forces.

Lanir and Fung in 1974 were the first to use planar biaxial testing for investigating biological soft tissue mechanics [6, 7]. In their experiments, a square sample (30 mm to 60 mm on a side) was attached with up to 17 sutures on each side to two fixed points and two linear actuators. A video dimensional analyzer (VDA, which generates a voltage proportional to the distance between contrast transitions along one axis in an analog video image) was used to measure stretch in the two orthogonal axes. Later biaxial testing studies of canine pericardium (the thin membrane that surrounds the heart, and a common focus of biaxial materials testing) demonstrated marked nonlinearity, anisotropy, and history dependence in the tissue mechanical properties [22, 23], and cross-axis coupling with strains in one axis affecting stresses in the orthogonal axis to varying degrees [24]. The testing system was further developed and used to measure the properties of lung tissue [25], and more recently canine pulmonary arteries [26].

Vito utilized a similar biaxial testing technique to investigate the mechanical properties of canine pericardium [27]. Humphrey *et al.* used finite element shape functions to fit the observed deformations in an experiment that appeared to show equibiaxial loading as sufficient to predict material response to nonequibiaxial loading [28]. Choi and Vito later developed a two-stage testing procedure to identify the material axes of

²In practice, the choice of n is determined by a compromise between computational efficiency and modeling accuracy. The linear (two-term) approximation is commonly used for natural rubber at moderate stretch ratios (up to $\lambda \lesssim 2 - 4$); larger deformations may require more terms to accurately model the material behavior, and for other materials entirely different forms of the strain energy function may be necessary.

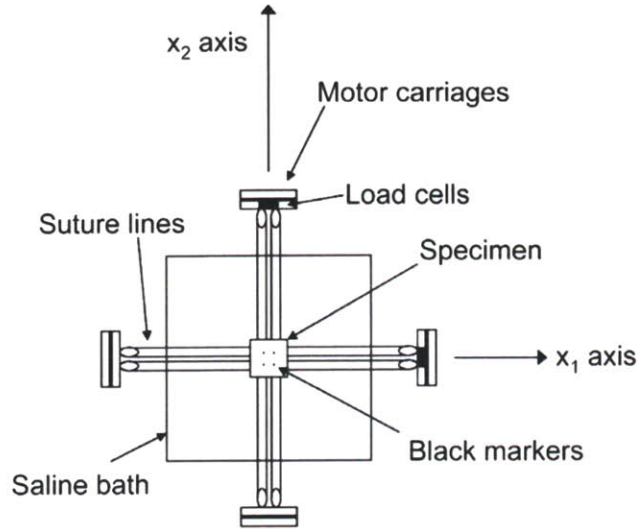


Figure 2-2. Diagram of a planar biaxial testing device for biological tissues and synthetic biomaterials. Four sutures are attached to each edge of the specimen via pulleys that allow for gross shearing of the specimen. (Image taken from Lu *et al.*[33])

anisotropic biological membranes [29]. This involved first stretching the specimen at successive increments of 15 degrees around the edges to identify the axes of greatest and least deformation by manual inspection and marking, and subsequently testing a subsample excised from the center of the original. More recently, Harris *et al.* reported an enhanced device integrating thermal control with mechanical loading [30, 31, 32] to evaluate the effects of thermal damage on the mechanical properties of biological tissues.

In 1999, Sacks developed a modified biaxial testing device that allowed the suture attachment pulleys at the actuators to rotate in the plane of the specimen as a means of imposing in-plane shear deformations (Figure 2-2) [34, 13]. For maximum shear to be imposed, however, the material axes must be known *a priori* before the specimen is loaded into the device. Sun *et al.* reported further development of this device by changing the strain-controlled protocol to stress-based control [35]. Tests on synthetic biomaterials have been reported using the same apparatus [33], and a testing system based on the work of this group is now commercially available [36].

Whereas biaxial testing on a larger scale has been used to some extent for the

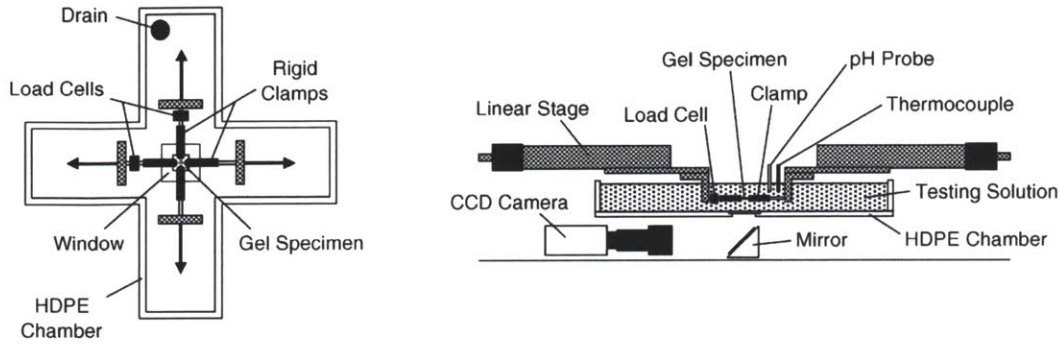


Figure 2-3. Planar biaxial testing device for electroactive polymer films. (Image taken from Marra *et al.* [37])

quantification of classical engineering material and textile properties, relatively fewer reports have been presented of biaxial testing for the mechanical evaluation of novel polymers. One recent example is the device developed by Marra *et al.* for testing active polyacrylonitrile gels [37]. General aspects of this device were similar to the biological testing systems above; a schematic is shown in Figure 2-3. Clamp-type attachments are used and marker points tracked to determine material deformation; and the device allowed for testing the polymer while immersed in various solutions.

2.2.2 Edge effects: attachment method and sample shape

The typical biaxial testing techniques described above involve analysis predicated on a uniform strain field in the center of the membrane, where the material is supposed to be sufficiently far removed from edge effects of attachment points (an application of the classic St Venant's principle). In 1991, Nielsen *et al.* conducted a study to evaluate the uniformity of strain imposed by such biaxial testing protocols [38]. The device incorporated 2-axis loading of a square membrane *via* four sutures per side, with each suture attached to the actuator with an individual force transducer. The study demonstrated that the central region of nearly uniform strain, which is broadly assumed to exist and taken as a basis for the material property calculations of the methods described above, is relatively small even for isotropic homogeneous materials in typical biaxial loading. For anisotropic and inhomogeneous materials it could be

expected to be even smaller.

In further analysis of edge effects on biaxial testing results, Waldman *et al.* presented a combination of analytical and experimental work on the effects of boundary conditions in planar-biaxial mechanical testing. Comparing the results of tests on bovine pericardium using clamped edges versus suture attachments demonstrated substantial effects of the sample gripping method. The computed mechanical properties differed substantially between the loading modalities [39], although collagen fiber orientation in the center of the sample, where the marker-based deformation measurements were made, was unaffected [40].

Recently, Sun *et al.* used finite element analysis to investigate the effects of edge clamping techniques on material biaxial extension tests, incorporating the effects of material anisotropy and attachment type (sutures vs. clamps) among the variables [9]. The results verified the earlier work of Nielsen *et al.* [38]; a nearly uniform stress level was found to be constrained to a small central region of the material. Both material axis orientation and attachment method were found to have significant effects on the stress distribution, with the clamp-type attachment demonstrating a stress-shielding effect and concentrating the stress at the edges for two non-suture geometries examined.

The results discussed above indicate that the precise means of load transmission do affect the distribution of stress and strain within membrane samples, often significantly enough to affect the reported mechanical properties from a typical biaxial testing protocol. From a theoretical standpoint, therefore, it is highly desirable to be able to rigorously specify the boundary conditions in a biaxial mechanical test and to fully account for the nonuniform distributions of stress and strain that arise in any attachment technique. In testing inhomogeneous samples this requirement becomes even more crucial in order to obtain meaningful results.

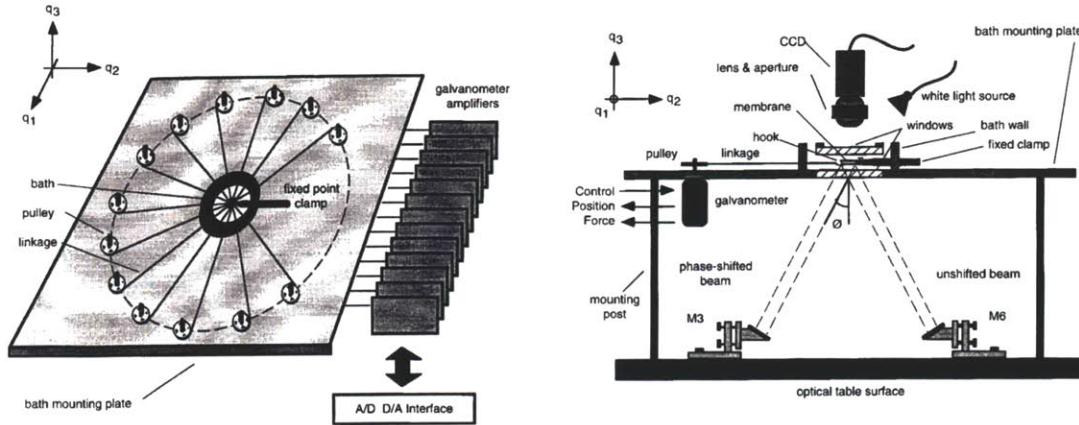


Figure 2-4. Biaxial materials testing system developed by Charette [11]. *Left*, schematic overview; *right*, cross-section with mechanical and optical layout. (Images taken from Charette [41])

2.3 Multiaxial multiple-1DOF-actuator systems

Addressing some of the limitations of classical planar biaxial testing apparatus, several investigators have developed multiaxial materials testing systems with a multiplicity of in-plane actuators, each with independent means of position control and force measurement. These refinements together provide for more flexible control of specimen loading compared to the typical planar biaxial testing systems, and additionally allow for the load/displacement boundary conditions on the entire test specimen to be measured precisely.

2.3.1 Charette / McGill system

Charette [11] first described a novel system with multiple independently-controlled attachment points designed for the testing of pericardium. The system utilized 16 galvanometers to simultaneously load the specimen, via hooks attached with fine chain and wire to fixed pulleys on each galvanometer axis, and to measure load on the specimen, using each galvanometer's well-quantified torque-current relationship. Speckle pattern interferometry augmented with a novel phase-unwrapping method was used to provide full-field deformation data at each motion step [11, 41].

To derive mechanical property estimates from the experimental data, a parameter

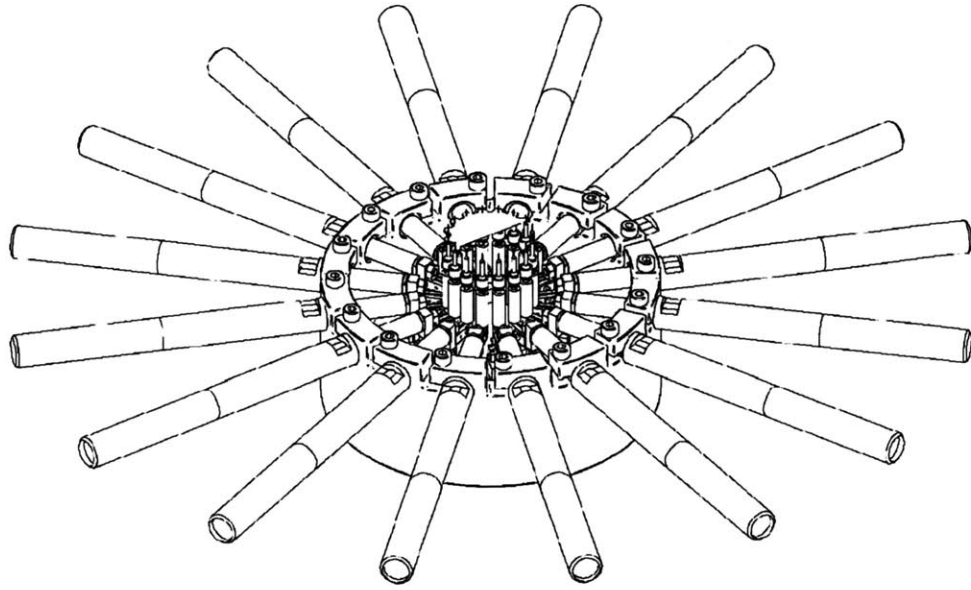


Figure 2-5. Diagram of biaxial testing apparatus for inhomogeneous membrane testing. Half a membrane is shown mounted on 8 of the 16 transducer pins. (Image taken from Nielsen *et al.* [12])

estimation technique was used. This involved defining a finite element model of the initial material geometry, fitting the model mesh to the real material geometry at each measurement step from the full-field deformation data, and subsequently performing an optimization on the parameters of a selected constitutive relationship form to minimize the difference between the finite-element model reaction forces and the measured loads at the attachment points [11, 42].

2.3.2 Nielsen / Auckland system

Nielsen *et al.* [12] developed a unique materials testing system explicitly for estimating the mechanical parameters of spatially inhomogeneous membranes. The physical instrument consists of sixteen micrometer actuators driven by DC motors, each of which carries a custom-built 2D force transducer at its tip to measure forces exerted on the membrane. A CCD camera captures images from a speckle pattern deposited on the membrane, and strain is measured directly from the material images using a Fourier transform cross-correlation technique [43].

The system described by Nielsen *et al.* accepts a 50 mm (minimum) diameter membrane with all 16 transducer/actuators, or 20 mm (minimum) with 8 actuators. Each force transducer has a capacity of 1.8 N in the configuration reported, with 2 mN resolution. The actuators have a travel range of 50 mm, step size of 60 nm, and maximum velocity of 0.71 mm/s. Testing was performed on a rubber membrane construct and sheep pericardium for displacement measurement [43], and parameter estimation was successfully used to determine assess spatially inhomogeneous material properties of the rubber construct [12].

Chapter 3

Design Considerations

The goal of the present work was to develop a flexible system for quantifying the material properties of inhomogeneous, anisotropic elastic membranes via planar biaxial testing, with particular applicability to polymers and biomaterials. This chapter discusses the components of the system from a theoretical standpoint, including the basic requirements for the system as a whole, the breakdown of the system into component parts, and the functional requirements and design strategies for individual components.

3.1 System concept

To model the mechanical behavior of materials, all mechanical testing seeks to determine the constitutive law of the material, that is, the intrinsic relationship between the stress state of the material and its resulting deformation. The previous chapter detailed a number of means to approach this problem for the specific case of biaxial testing of membrane materials, following instrumentation design toward the goal of quantifying the properties of anisotropic and inhomogeneous membranes. The system described in the present work builds on the previous approaches and offers a number of enhancements.

Three key functional requirements drove the development of the flexible mechanical testing device:

- The device should be capable of imposing arbitrary load and deformation patterns on the membrane under test.
- The applied loads must be quantifiable at the point of load application, not averaged over an area (a requirement for the finite element model used in parameter estimation).
- Full-field displacement measurement must be possible, with high spatial resolution and sensitivity.

The first requirement informs the arrangement and type of actuators used for imposing load on the test specimen. The second imposes constraints on the force transducer and attachment point arrangement. The third requirement dictates the need for an optical system incorporating full-field imaging.

3.1.1 Flexible loading schemes

Existing biaxial materials testing systems generally provide little flexibility in the loading modalities available. For the present device, we sought the ability to impose arbitrary deformation states on the material under test.

Material attachment points in planar biaxial systems have one controlled degree of freedom, with the orthogonal degree of freedom either fully constrained (in the case of pin-type or clamp-type attachments) or unconstrained (in the case of suture or staple attachments). In both cases, specific loading patterns are produced by varying the ratio of extensions (or of forces, if using force-feedback control) among the independent axes. Typical planar biaxial testing systems have only one variable defining the loading pattern—the ratio of extensions along two axes. For the multiple-actuator systems discussed in Section 2.3, a richer set of imposed deformations is possible. However, in all of the above devices the available loading modes are limited to the range of linear combinations of motions along one axis for each attachment point (Figure 3-1).

For the greatest flexibility in loading and control, the number of motion degrees of freedom at each attachment point should match the number of axes along which

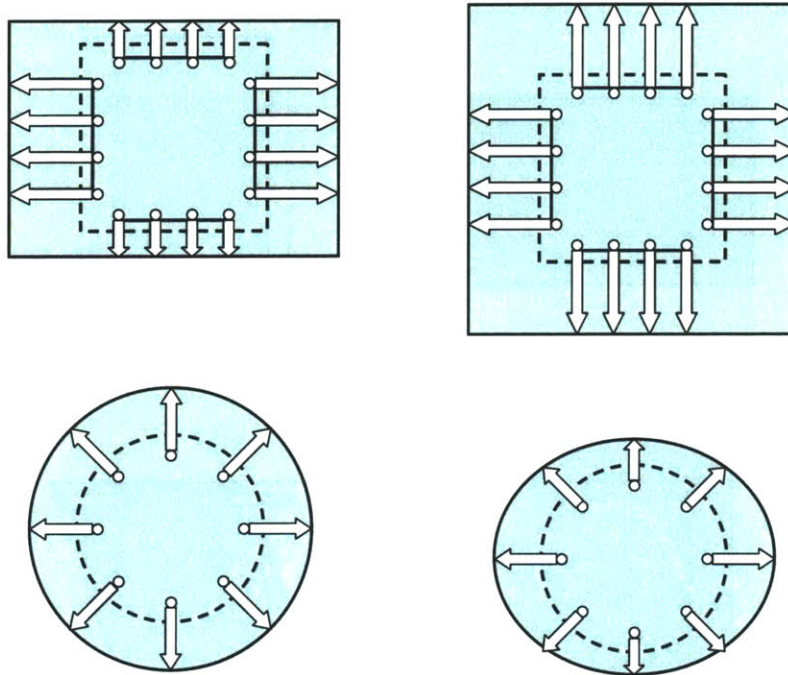


Figure 3-1. Sample deformations with existing biaxial material testing systems. *Top row*, suture attachments on square sample with unequal (*left*) and equal (*right*) extension ratios. *Bottom row*, single radial degree of freedom attachments on circular sample with equal (*left*) and unequal (*right*) extension ratios along x and y axes. For both actuator/attachment arrangements, motion of the attachment points is controlled only along the directions of the arrows.

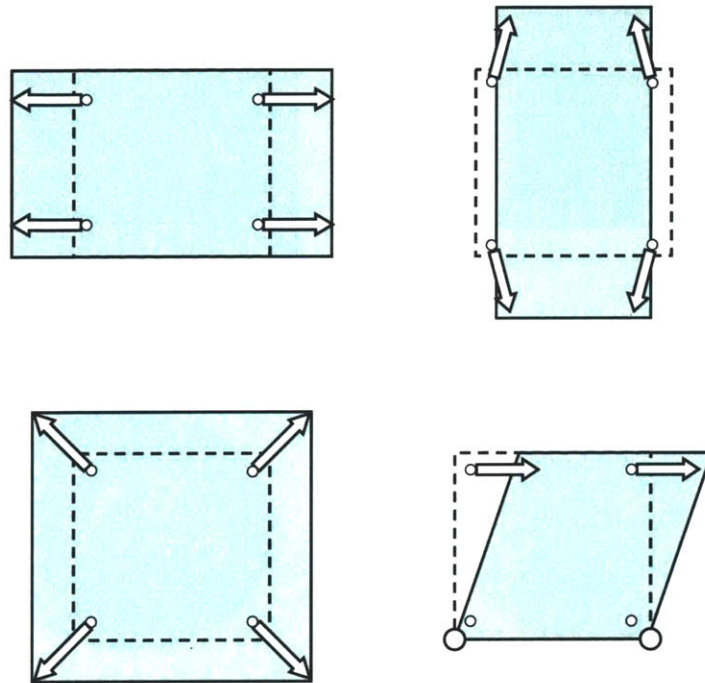


Figure 3-2. Sample deformations possible with two degrees of freedom at each attachment point. *Upper left*, extension along x -axis; *upper right*, extension along y -axis with contraction in x -axis; *lower left*, uniform expansion; *lower right*, in-plane shear.

force data is available. With a planar testing system, two in-plane degrees of freedom are available; with arbitrary force/displacement control of both degrees of freedom at each attachment point, a complete set of deformations may be imposed. Most notably, the same system configuration may be used both for extension testing and for imposing overall shear on the specimen (Figure 3-2). The same flexibility may be useful in testing composite structures (e.g. intact biological specimens), where the inhomogeneous internal structure contributes to preferred directions of stiffness and deformation of a larger specimen.

3.1.2 Full-field analysis

Whereas variation of material properties over an area is the rule in biological materials and may be desirable in engineered materials and systems, most existing biaxial testing systems are unable to accurately assess mechanical properties of spatially inhomogeneous materials. Membrane inflation (Section 2.1) and typical planar biaxial extension techniques (Section 2.2) rely on the assumption of homogeneity in analyzing the force and deformation data from individual tests. An element of uncertainty is introduced as the points of load application are removed from the edges of the area over which deformation is analyzed and the material properties computed.

To overcome the above shortcomings, a system designed explicitly for finite-element model based analysis is proposed, utilizing full-field imaging for the acquisition of deformation data and distributed parameter estimation for the analysis of spatially varying material properties. These techniques are presented in detail by Nielsen *et al.* and Malcolm *et al.* [12, 43].

3.2 Instrumentation components and parameters

Several major components are required in the apparatus to fulfill the general requirements discussed above. An arrangement of actuators attached to the material under test is required to meet the criterion of applying loads with various stress components. An optical system with a high-resolution camera and optics allows for full-field

imaging and the computation of strain data throughout the material. Precise force transducers measure the material reaction forces. An overview of the requirements for these components is provided below; further details on design and construction are found in Chapter 4

3.2.1 Actuator system

The actuator system must apply loads and deformations on the material under test. The range of specimen size was to be no larger than that of previous biaxial studies (50 mm diameter/square maximum) and similar force capacity was desired (2 to 5 N).

A number of actuator types and configurations were under consideration for the present device, including: parallel actuation with two separately mounted linear actuators for each attachment point; DC servo or stepper motor-based micrometer drive actuators; as well as the linear motor based stages that were selected.

Key parameters in the selection of an actuator technology and configuration include: resolution, precision, and accuracy of motion; load capacity; simplicity of feedback control; and static and dynamic tracking performance. The backlash-free operation of linear motor driven stages was attractive from the standpoint of controllability and dynamic performance, and several models were considered and tested for possible use.

3.2.2 Optical system

For full-field strain analysis across the entire membrane, a high-resolution digital imaging system is required. To capture images of the membrane under test, the system requires a camera incorporating a digital imaging sensor (CCD or CMOS); a lens matched to the sizes of the imaging sensor and the sample under test; and a focusing stage to adjust lens focus at various sample sizes and magnification ratios.

The ideal camera would have both high spatial resolution and high dynamic range; however the combination of the two is limited by a number of tradeoffs: bandwidth between the camera and computer is limited, which may become an issue at larger

resolutions, bit depths, and speeds; while electron well depth (which in conjunction with noise properties contributes to imaging system dynamic range) typically must be traded off against resolution for a given sensor size.

For accurate imaging at high resolution, the requirements on the lens include a large aperture to maximize spatial resolution; an imaging circle at least as large as the sensor diagonal; and minimal geometric distortion. To fill the sensor frame over a range of sample sizes, a lens capable of imaging at demagnification ratios from 1:4 to 1:1 is desired; for a 40 mm sensor diagonal, this allows for limiting sample dimensions at greatest extension of 28 mm to 113 mm square (40 mm to 160 mm on the diagonal).

The main components of the optical system were selected from commercially available products and are detailed in Section 4.2.

3.2.3 Force measurement system

To generate a complete description of the boundary conditions imposed on materials under test, the force acting at each material attachment point must be measured in two axes. Key design parameters for the force transducer include size, load capacity, sensitivity, accuracy, and repeatability. The transducer must measure loads in the active axes (in the plane of the sample) while rejecting off-axis loading, including in-plane moments and out-of-plane forces. Compact packaging is also a key requirement for testing of small samples and integration of the transducer with the sample attachment means.

Existing force transducer designs

Specifications of representative commercial force transducers with load capacities in the target range are presented in Table 3.2.3. No existing commercial two-axis force transducer or combination of single-axis transducers was identified that could meet the design requirements outlined above for the multiaxial testing system. Therefore the design of a custom transducer/attachment unit was pursued. Nielsen *et al.* [12], facing similar constraints, successfully developed their own transducers for their

	Futek L1070 [44]	Futek L2357 [45]	Units
Type	2-axis column	1-axis S-beam	
Body diameter	34.3	25.9(*)	mm
Height	75.7	13.6(*)	mm
Mass	255	18(*)	g
Minimum capacity	45	0.1	N
Output	2.0	2.0	mV/V
Nonlinearity	±0.25%	±0.1%	
Transverse sensitivity	(†)	(†)	

(*) Effective dimension of box-shaped transducer; height and mass consider two single-axis transducers stacked.

(†) not specified

Table 3.1. Specifications of low-capacity commercial force transducers.

testing system; their work served as conceptual support and inspiration.

Bending beam force transducer

The cantilever beam force transducer is among the simplest designs for measuring force; and most significantly, it lends itself readily to the construction of a small monolithic transducer that measures forces in two perpendicular axes and rejects the effects of other loads, while maintaining a minimum profile in the plane of sensitivity.

A schematic of a basic bending beam transducer instrumented with strain gages in a half Wheatstone bridge is shown in Figure 3-3. Two uniaxial strain gages on the surface of the beam are used, located symmetrically with respect to the neutral axis.

If the force is applied on an axis perpendicular to the gage mounting surfaces, the faces where the gages are mounted will be in pure compression and tension with no shear loading. The stresses, σ , at the gage mounting surfaces are then given by

$$\sigma = \pm \frac{Mc}{I}, \quad (3.1)$$

where M is the bending moment, c is the distance from the neutral axis of the beam, and I is the beam moment of inertia [46].

For a beam with constant cross section of dimensions $b \times h$, the moment of inertia,

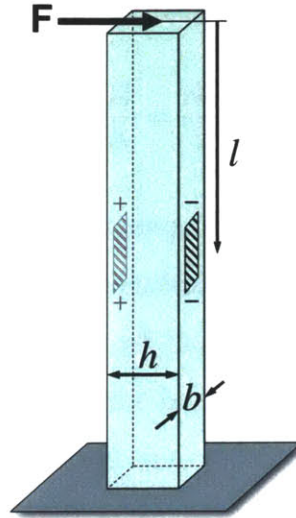


Figure 3-3. Simple bending beam transducer. Strain gages (cross-hatched) measure positive and negative strain as indicated in response to the applied force.

I , is equal to $\frac{1}{12}bh^3$. At a given distance l from the point of load application on the beam, the bending moment due to the applied force is simply $M = Fl$. With no additional loads on the beam and a linear elastic beam material of elastic modulus E ($\sigma = \varepsilon E$), the resulting strain, ε , on the gage mounting surfaces is then

$$\varepsilon = \pm \frac{6Fl}{Ebh^2}. \quad (3.2)$$

For a strain gage with gage factor G , the output V_o of the half-Wheatstone bridge circuit with excitation voltage V_e is given by

$$\frac{V_o}{V_e} = \frac{G\varepsilon}{2}, \quad (3.3)$$

so the voltage output of the instrumented bending beam transducer is given by

$$\frac{V_o}{V_e} = \frac{3GFl}{Ebh^2}. \quad (3.4)$$

Because the bridge output is typically in the mV range, an instrumentation amplifier

is commonly used. Given an amplifier gain of G_a , the final amplified output is then

$$V_{amp} = \frac{G\varepsilon}{2} = \frac{3GF_l}{Ebh^2} V_e G_a. \quad (3.5)$$

The bending beam transducer arrangement above is insensitive to loading in directions other than that indicated. Resistance changes caused by strains of like sign due to axial loading will be cancelled out by the bridge arrangement; thermal loads likewise will cause both gages to respond similarly and cancel out the effect at the bridge output [47]. Force loading in the axis perpendicular to the indicated force will result in symmetric strain distributions under the strain gages on adjacent arms of the Wheatstone bridge, with no net effect on the bridge output. In addition, torsional loading along the axis of the transducer will also lead to equal shear strains (and no net area change) at both gages, so the output is likewise unaffected.

Refinements to the bending beam transducer

To minimize the deflection at the point of load application due to bending of the beam, it is desirable to concentrate the stress and strain at the gaged area. From Figure 3-3 and Equation 3.2, it is clear that most of the beam length serves primarily to convert the applied force to a moment at the gaged area. Thus, to maximize transducer stiffness and minimize deflection under load, the beam may be made with a larger cross-section everywhere except at the gaged area, where the cross-section factors into the transducer output [48].

A refined bending beam transducer configured for two-axis force measurement is shown in Figure 3-4. The transducer body may be made from round stock for ease of machining, with the central portion tapering to a square cross-section where the strain gages are applied. The square cross-section gives equal sensitivity to loads in both axes perpendicular to the length of the beam. With $b = h$ in Equation 3.2, the strain at the gaged area due to a load F in either axis is governed by

$$\varepsilon = \pm \frac{6Fl}{Eh^3}. \quad (3.6)$$

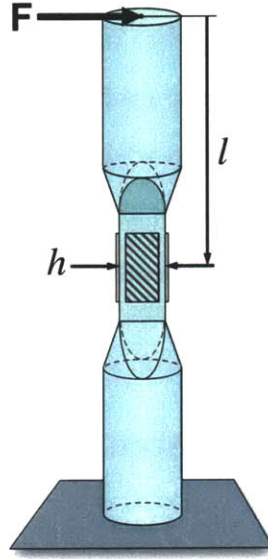


Figure 3-4. Two-axis cantilever beam transducer design. Narrowed central cross-section concentrates stress and strain at the gaged area (cross-hatched). A half-bridge for each axis is formed with strain gages on opposing sides of the central square section.

With the same half Wheatstone bridge arrangement for each axis as for the basic bending beam transducer, the bridge output voltage for each axis (substituting $b = h$ in Equation 3.4) is given by,

$$\frac{V_o}{V_e} = \frac{3GF l}{Eh^3}, \quad (3.7)$$

and again including an amplifier of gain G_a , the amplified output voltage is

$$V_{amp} = \frac{3GF l}{Eh^3} V_e G_a. \quad (3.8)$$

One limitation of the above design is that the distribution of bending moment, and thus of strain, is not uniform over the length of the strain gages. As the bending moment varies linearly with l , so the strain varies linearly across the gage length. This effect may be mitigated by tapering the sides of the beam to make the moment of inertia of the cantilever beam at the gage area vary proportionally with the applied moment [48]. This would be relatively simple to accomplish with the fabrication

techniques discussed in Section 4.4.4; however, it would not be appropriate for a modular transducer designed with variable moment arm lengths to accommodate a range of load capacities. Moreover, since each strain gage acts to average the strain over its area, the linear variation of strain with axial position only affects the effective strain through possible axial misalignment of the gages. Provided that the gages can be aligned with sufficient accuracy, the nonuniform strain field therefore should not compromise transducer performance.

3.2.4 Instrument control system

The mechanical testing instrument must incorporate a control system to integrate the various subsystems described above. A data acquisition system is required to record the data from the force transducers for analysis. The test parameters must be specified and translated into commands for the motion subsystem and timing parameters for the camera and data acquisition hardware. Data from the transducers, camera, and motion system feedback must be saved for further analysis. Finally, a user interface that allows easy access to all the instrument functions is a requirement for operation.

Chapter 4

System Design and Implementation

This chapter details the specific implementation of key components of the multiaxial materials testing system. The optical subsystem, consisting of the camera, lens, and positioning stage, is described first. The motion system that provides $x - y$ displacement at each transducer point is discussed next, followed by a detailed description of the design, analytical results, and manufacturing processes for the precision two-axis force transducer. Finally, an overview of the data acquisition system and the instrument control software is provided.

4.1 System overview

Figure 4-1 presents a schematic overview of the multiaxial materials testing system. The optical subsystem, motion subsystem, and force transducer subsystem (indicated with dashed outlines) each receive commands from and send data to the instrument control components that run on the computer. Key signal and data paths (analog and digital) are shown as lines on the diagram; for simplicity, power and physical connections (e.g., between the transducers and the motion stages on which they are mounted) are not shown.

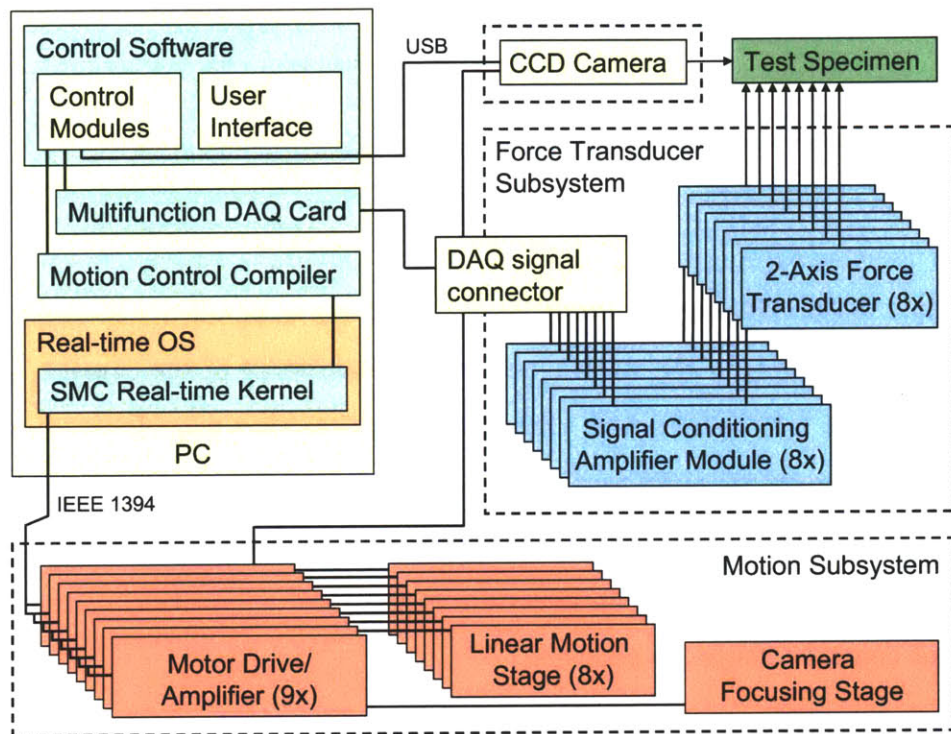


Figure 4-1. Testing system schematic overview.

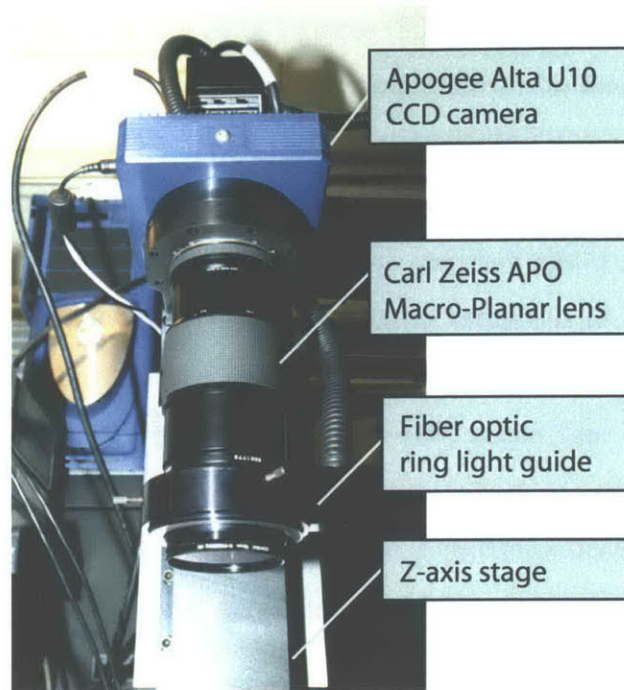


Figure 4-2. Components of the optical subsystem: camera, lens, and lighting.

4.2 Optical subsystem

The optical subsystem consists of a high-resolution digital astronomy camera and macro lens to capture images of the membrane under test, mounted on a vertical positioning stage for adjustment of magnification and focus (Figure 4-2).

The Apogee Alta U10 camera [49] was selected as the imaging device for capturing high-resolution full-field test data. The camera incorporates an Atmel THX7899 CCD sensor with $14\ \mu\text{m}$ square pixels in a 2048×2048 -effective-pixel array. The CCD has an electron well depth of $270\ \text{ke}^{-1}$, the largest available in a 4 Mpixel sensor at the time of construction, and offers $>80\ \text{dB}$ dynamic range. The U10 offers onboard cooling of the CCD using a regulated thermoelectric cooler and fan system with software control. The fans may be turned off if needed during an exposure to minimize vibration for precision measurement. The camera is connected to the PC system via a USB2 bus (480 Mb/s data rate) for data transfer; exposures may be triggered either through software commands or more precisely with timing pulses via the digital outputs of the data acquisition card.

The large format of the camera CCD sensor (40.55 mm imaging diagonal) demands a lens designed for a medium-format camera rather than the typical enlarger or 35 mm SLR lens. A Carl Zeiss APO-Makro-Planar 120 lens [50] was chosen for this purpose. The lens is designed for the Contax medium-format system, which has the largest lens flange-to-imaging plane distance among common medium-format cameras; this allowed for flexibility in designing a custom camera/lens mount. The lens covers demagnification ratios between $1:\infty$ and 1:1 when mounted at the specified flange-image plane distance, and has a near-flat modulation transfer function and $<0.5\%$ distortion to 20 mm image radius at 1:2 and 1:1 magnification and the maximum aperture of $f/4$ (numerical aperture = 0.125). A fiber optic ring light guide connected to a Stocker-Yale model 21DC regulated source is attached to the object end of the lens to provide specimen illumination.

The camera and lens are mounted with a two-piece custom-machined aluminum bracket assembly onto a vertically-oriented Aerotech ATS125 leadscrew-actuated stage driven by a stepper motor [51]. The bracket assembly incorporates a Contax lens mount and allows the camera and lens mounts to be independently interchanged. The stage has 300mm travel and $1.0\ \mu\text{m}$ positional repeatability, well below the minimum depth of field of the imaging system at 1:1 magnification. The stage is controlled by an Aerotech *nDrive* drive/amplifier that offers hardware and software commonality with the remainder of the motion system components (see Section 4.3).

4.3 Motion subsystem

Four pairs of Aerotech ANT-25 linear motor driven stages mounted in a stacked x - y configuration (Figure 4-3) are used to provide the linear motion for the material attachment points. The ANT-25 stage is driven by a brushless DC linear motor with constant force capacity of approximately 6.5 N [52].¹ A noncontact linear encoder is used with external interpolation to provide positioning resolution of 20 nm. A sample

¹Tested capacity. Nominal capacity according to specifications was 11 N; however, testing revealed that with servo parameters optimized the actual force capacity was less than 7 N.



Figure 4-3. Aerotech ANT-25 linear motion stage in stacked x - y configuration. Image taken from [52].

stage was tested with an interferometer system and the stage resolution verified; position noise when holding constant position under load was within ± 40 nm, or approximately two encoder counts. An Aerotech nDrive drive/amplifier unit provides power and closed-loop current control of each motion stage at 8 kHz, and all drive units communicate with control software running in a real-time environment on the host PC via the IEEE1394 (Firewire) bus at a 1 kHz update rate.

4.3.1 Motion stage parameter tuning

To obtain optimal performance, the control constants of the servo loop in the motion control hardware and software must be tuned with the working load on the motion stages. In the tuning process, stiffness of the stage and the ability to track commands at increasing acceleration (thus increasing force) demands are traded off against servo loop stability and the limited current available from the drive/amplifier. A basic manual tuning procedure is given in the Aerotech system reference [53]. The procedure involves limiting the number of influential servo loop parameters at the outset, adding and adjusting additional parameters one at a time until either the performance meets the desired criteria or instability is observed. In practice, it was found that manual tweaking of parameters in a sequential fashion was required to obtain the maximum dynamic response. (Details on the servo loop configuration and parameters are included in Appendix B.)

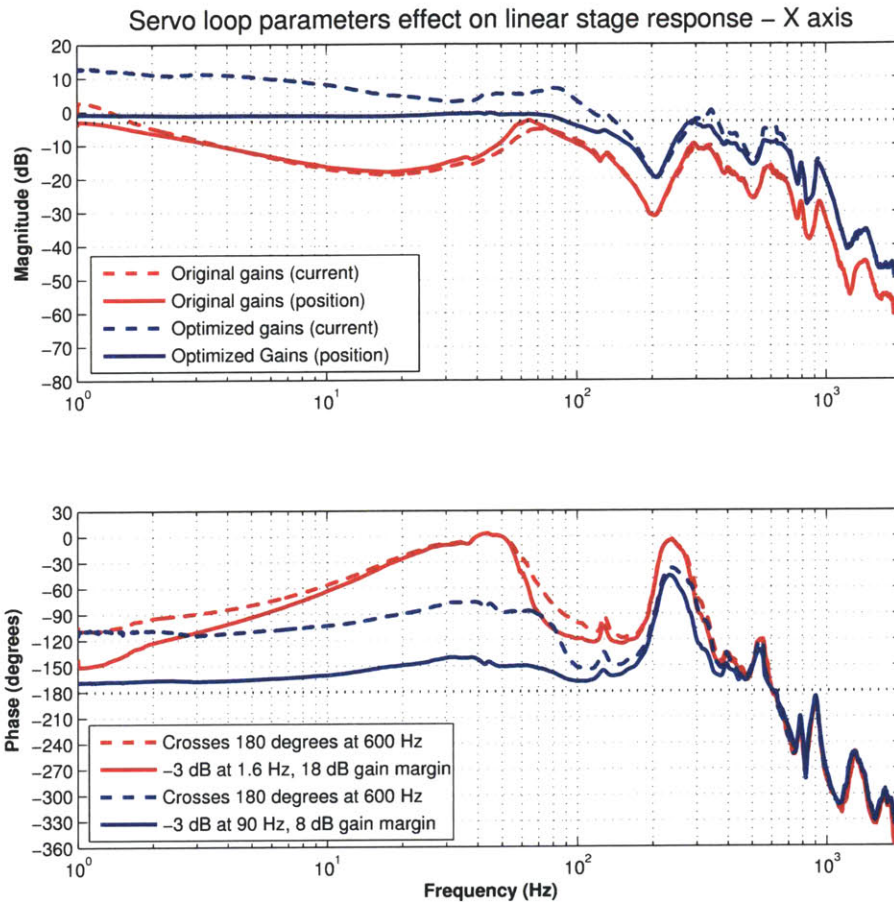


Figure 4-4. Frequency response of ANT-25 linear motion stage–*n*Drive drive/amplifier system before and after tuning of servo loop parameters. Dashed lines show current loop response; solid lines show computed position loop response. Parameter tuning results in improved frequency response with only limited reduction in system stability.

The response of the motion system current and position-tracking loops before and after parameter optimization is shown in Figure 4-4. Current loop gain and phase data were obtained from the Aerotech Loop Transmission utility, which computes the performance of the drive/amplifier's internal current-tracking loop. The position command is held at zero while a disturbance is injected into the current loop between the PID and servo amplifier stages, with the current before and after the disturbance monitored at 8 kHz, and the resulting magnitude and phase data saved [53]. Given the control loop configuration, the position loop response can be computed trivially from the current loop response (see Appendix B). Initial servo loop parameters are those supplied with the motion system. Parameters were adjusted sequentially to obtain maximum frequency response of the lower (x -axis) stage while suppressing instability. Manual tuning improved the frequency limit of position response substantially, with the -3 dB point moved from 1.6 Hz to 90 Hz, and a nearly flat system response to ~ 80 Hz after tuning.

4.4 Force transducers

A strain-gage based bending beam force transducer was designed to measure loads in two orthogonal directions at each material attachment point. The design considerations for a bending beam transducer as well as a derivation of the theoretical output are presented in Section 3.2.3. The specific implementation of a miniature precision bending-beam transducer for the present instrument is described below.

4.4.1 Transducer mechanical design

The force transducer was designed as a modular assembly consisting of three units: the transducer body, on which strain gages are mounted; a pin assembly that fits in a precision bore at the top of the body, and a threaded collet that keeps the pin firmly attached to the transducer body (Figure 4-5). This design allows the range of the transducer to be tailored to the requirements of a particular experiment simply by choosing a different length pin assembly. In addition, the pin assembly components

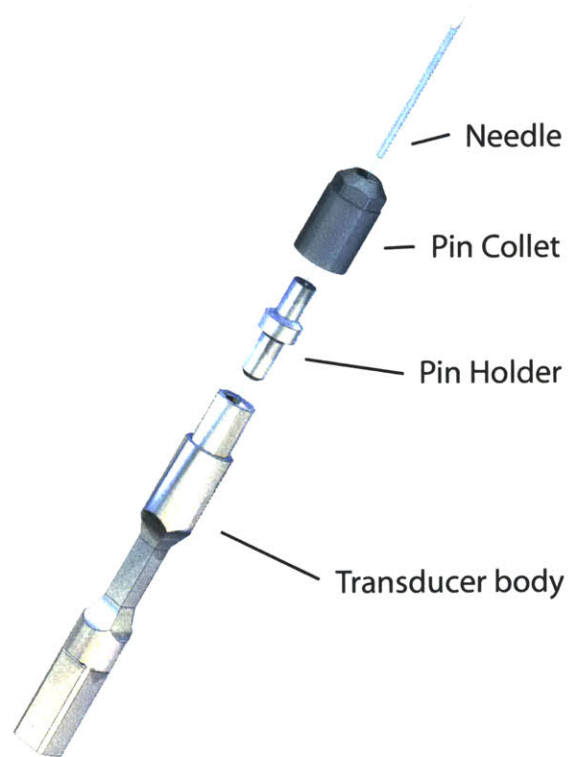


Figure 4-5. Force transducer assembly: exploded view.

	Metal Foil	Semiconductor	Units
Gage factor	2.0	-100 to +150	
Resistance	120–5000	1000–5000	Ω
Temp. Coeff. (Resistance)	10.6	90000	$1/(^{\circ}\text{C} \times 10^{-6})$
Temp. Coeff. (Gage factor)	$< 10^*$		$1/(^{\circ}\text{C} \times 10^{-6})$
Transverse sensitivity	2%	-20%	

Metal foil values are for constantan gages

(*) based on temperature compensation mismatch

Table 4.1. Comparison of typical foil and semiconductor strain gage properties. Data from [54, 55].

may be replaced should they become damaged or unusable, without disturbing the transducer body. The pin attachments could conceivably be exchanged for other means of specimen attachment for experiments where pinpoint loads are not desired.

4.4.2 Strain gage selection

Both metal foil and semiconductor (silicon) strain gages were considered for sensing strain on the bending-beam force transducer. Selected figures of merit for both gage families are presented in Table 4.4.2. Whereas silicon gages offer substantially enhanced sensitivity compared to metal foil gages, their output is much more strongly dependent on temperature. In addition, foil gages are typically available in a greater variety of grid patterns at lower cost. Temperature stability was reported to be an issue with silicon-gage-based transducers in an earlier biaxial testing system [12], and mounting of the gages was difficult; therefore foil gages were selected for use in the present transducer.

Vishay C2A constantan-foil gages with pre-attached leadwires [54] were selected for relative ease of assembly and to minimize the need for direct soldering to the delicate gage terminals. Sufficiently small size gages were readily available (to 2.0 mm width in 1.6 mm and 3.2 mm gage lengths) to allow the construction of a compact transducer. Nominal resistance was $350.0 \Omega \pm 0.6\%$, with a gage factor of $2.095 \pm 0.5\%$. Each gage was measured prior to installation and pairs matched for resistance to 0.1% were selected from larger lots for each transducer axis.

4.4.3 Analytical and numerical modeling

To determine appropriate dimensions for the transducer, analytical and finite element models were considered. The final design resulted from a consideration of the desired load capacity, available strain gages, and material properties of common transducer elements. An analytical model of the basic design was considered first to establish desired design dimensions, and a finite element model with the resulting geometry was used to model the expected performance of the transducer.

Analytical model

The design model of the transducer was based upon the analysis of the bending beam configuration presented in Section 3.2.3. For simplicity and to give equal sensitivity in two axes, a bending beam with square cross-section at the gaged area was considered. In this configuration, the strain at the gaged area is given by (Equation 3.6):

$$\varepsilon = \pm \frac{6Fl}{Eh^3}. \quad (4.1)$$

Transducer output is proportional to strain (Equation 3.3), so to maximize sensitivity (output/load) one seeks to maximize the numerator or minimize the denominator in Equation 4.1, subject to physical constraints. For a given force, the only free variables are beam length (l), width of the gaged area (h), and elastic modulus of the transducer material (E). Length is limited by constraints on the physical size of the transducer; width is limited by the size of available strain gages; and the elastic modulus is limited by available materials with appropriate strength and machining characteristics.

For simplicity of design, the transducer material was selected first; followed by a combination of beam length and width to accommodate the desired strain gages while allowing for a relatively compact overall package. An overview of common materials for transducer elements is given in [56]. For a low-capacity transducer, one seeks a material with relatively low elastic modulus (to convert limited stress into measurable strain) yet sufficient strength and machinability characteristics. 2024 aluminum meets

these requirements, has other desirable properties (e.g., low hysteresis), and is readily available from commercial suppliers. Numerous stainless steels (e.g., 17-4PH) also meet the criteria for a good transducer spring element; however, the modulus of steel is approximately 2.7 times that of aluminum; thus, a steel transducer would have required either a substantially thinner center section or a substantially longer transducer body to obtain sufficient strain at the gage area (see specific calculations in Appendix C). The former would have added to the difficulty of strain gage mounting, while the latter would be unwieldy in assembly. Therefore, aluminum was selected for the transducer body structure.

Given the material elastic modulus ($E = 73.1$ GPa for 2024 aluminum [57]), the transducer dimensions can be selected by considering strain gage characteristics and the desired load capacity. Strain gage cycle life determines the maximum allowable strain—for the C2A gages used in the transducer, fatigue life is 10^6 cycles at a strain (ε_{max}) of 1.5×10^{-3} . This puts an upper bound on ε for the maximum load. The desired load capacity and maximum strain can then be substituted into Equation 4.1 and the required length-width relation determined:

$$\frac{l}{h^3} = \frac{E\varepsilon_{max}}{6F}. \quad (4.2)$$

Used together with the output equation (Equation 3.3),

$$\frac{V_o}{V_e} = \frac{G\varepsilon}{2}, \quad (4.3)$$

the geometry and excitation voltage may be varied to give the desired response. A number of combinations of transducer dimensions, amplifier gains, and load capacities were considered in the design process; an analysis of various configurations is provided in Appendix C. To give a full-scale output voltage of 10 V at 10 N load with $V_e = 4.0$ V and amplifier gain (determined by the signal conditioning amplifier gain equation and the available resistors) of 2002, the selected dimensions were $l = 31.0$ mm and $w = 2.795$ mm. These dimensions were used in the finite element analysis presented below.

Finite element analysis

A finite element model of the transducer body was constructed to validate the analytical response calculations and to provide insight into the transducer static and dynamic mechanical response. Briefly, a half-model of the transducer was constructed with the design geometry of the full transducer assembly. The entire assembly was modeled as a solid unit; to take into account the additional mass of the steel pin holder, which would affect the dynamic response, the geometry was modified near the loaded end of the transducer to provide an equivalent total mass and center of mass location to that computed in the CAD model of the transducer assembly. Given the symmetric geometry of the design, a half-model was used with loading on the plane of symmetry.

The finite element analysis was performed in ANSYS 9.0. A linear elastic material model was used, with E as above and density of 2024 aluminum = 2780 kg/m^3 [58] for the dynamic analysis. The mounting end of the transducer model was constrained to zero displacement at the bottom face, with the load applied as a nodal force at the center of the transducer tip. The transducer response was computed for a series of load steps from 1.0 N to 5.0 N on the half-model, corresponding to 2.0 N to 10.0 N load on the full transducer. Displacement, axial strain on the gage mounting surface, and stress were examined for insight into the transducer performance.

Transducer tip displacement and Z-axis strain (along the axis of gage sensitivity) for the full-scale load of 10 N is shown in Figure 4-6; stress and equivalent total strain results are presented in Figure 4-7. The tip displacement was linear with applied force, and reached $325 \mu\text{m}$ at 10 N load; the resulting transducer stiffness was 30.8 kN/m . Axial strain on the gage mounting surface varied linearly with distance along the transducer axis, as predicted from theory.

The maximum stress on the transducer at 10 N load was 105 MN/m^2 , which occurred at the bottom of the narrow cross-section of the gage mounting area. This value is substantially less than the proportional limit of $\sim 235 \text{ MN/m}^2$ for 2024 aluminum alloy [57]. Dynamic response was also modeled, with modal analysis revealing the first resonant frequency at 855 Hz and no further modes below 1 kHz.

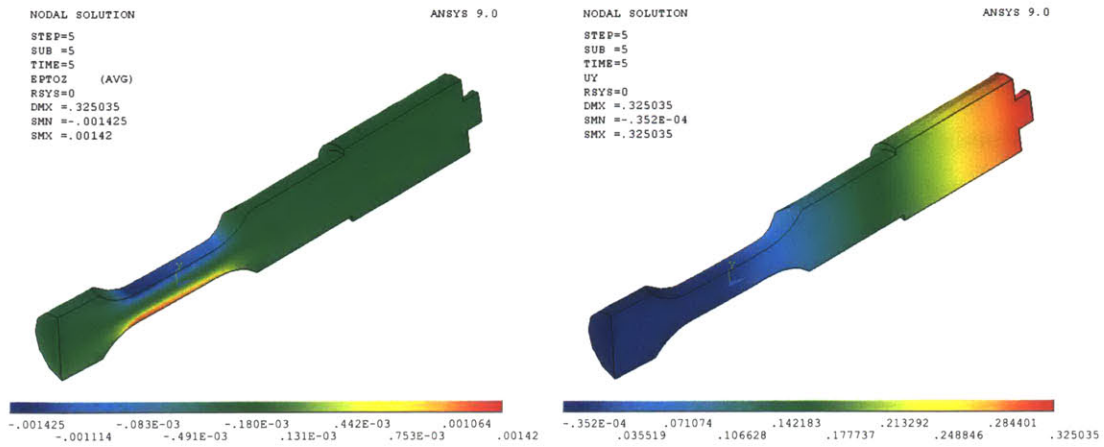


Figure 4-6. Axial strain (*left*) and y -component of tip displacement (*right*) for the force transducer model under 10 N load. Strain in engineering units, displacement in mm.

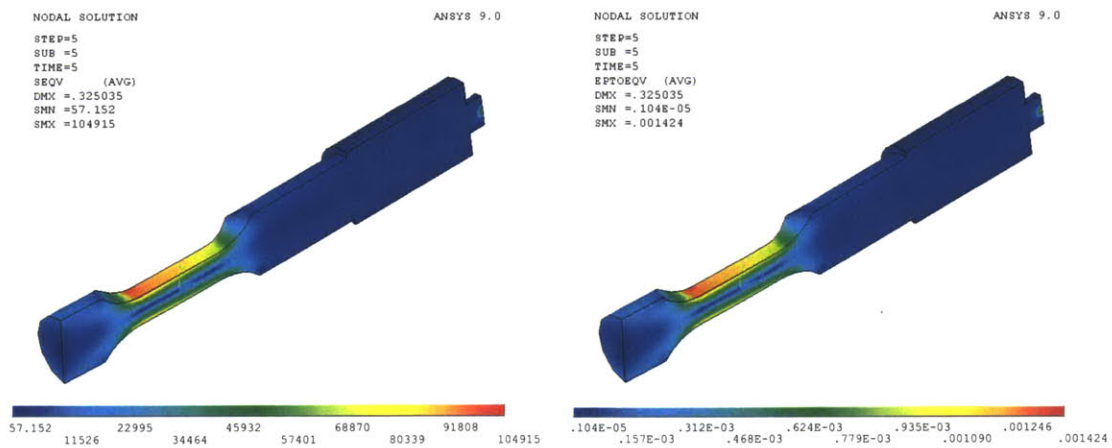


Figure 4-7. Von Mises stress (*left*) and equivalent strain (*right*) for the force transducer model under 10 N load. Stress in kN/m^2 , strain in engineering units.

4.4.4 Transducer construction details

The body of the force transducer is machined from 2024-T4 aluminum, a common material for low-load transducer applications. Aluminum is easily machined at low cutting loads with conventional tools; and it is readily finished to precise dimensions by electrical discharge machining (EDM) [59].

The pin assembly that mounts in the transducer body consists of the pin holder body and a 20 gauge (0.91 mm diameter) stainless steel hypodermic needle held captive in a hole on the specimen mounting surface of the pin holder. The pin holder body is machined from 17-4PH stainless steel on a Mazak Super Quick Turn 15MS turn/mill center (Mazak Corp., Florence, KY). A single set of pin holders with 7 mm effective length (for 10 N transducer range) was made. The syringe needles were cut by hand and deburred before insertion in the holder, and were secured in place with Loctite structural adhesive.

The collet that holds the pin assembly in place in the transducer body is machined from Delrin (acetal homopolymer) on the Mazak turn/mill center in a single process. The internal threads that mate with the threaded transducer body were tapped manually before the final cutoff operation.

Transducer body machining

All mechanical components of the force transducers were machined in house using CNC equipment. The transducer body was first machined in the Mazak turn/mill center; subsequently the narrow center profile and the mounting features at the base were machined using EDM. Before the transducer was cut off from the stock, the EDM was used to make shallow cuts (approximately 50 μm deep) in the center of the gage section to serve as alignment marks for gage mounting. Figure 4-8 illustrates the transducer body after machining.

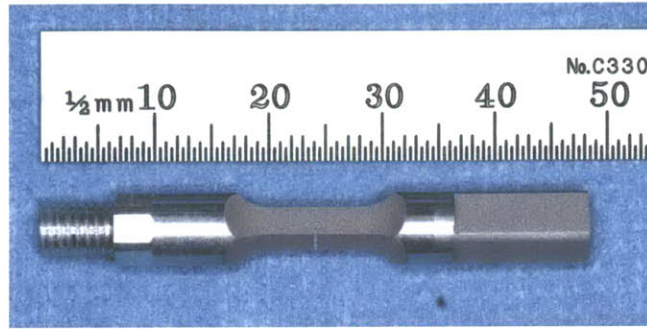


Figure 4-8. Force transducer body after CNC machining in the turn/mill and EDM, and before preparation for strain gage bonding.

Strain gage bonding

Mounting of strain gages on the transducer body generally followed the procedure outlined in the gage and epoxy manufacturer's guidelines. Surface preparation guidelines given in [60] were followed, including multiple sanding steps with fine sandpaper, a mild chemical etch, and thorough cleaning and drying before application of each strain gage. After surface preparation, the gage is aligned by hand and tacked in place using clear cellophane tape prior to application of epoxy. The gage and specimen are then clamped together with an elastomer pad to distribute the clamping force while the epoxy cures. A general-purpose 100%-solids epoxy (Vishay Measurements Group AE-15) was used for bonding, which offered a balance between low glue-line thickness (desired to minimize creep in the transducer) and ease of application [61].

Obtaining accurate alignment of the gages presented a challenge, as the gage backing was wider than the transducer body, leaving no surface for the tape to adhere and keep the gage in place after the application of epoxy. Initial trials with prototype transducers indicated the need for slight modifications to the typical procedure due to the limited space. A special jig (Figure 4-9) was manufactured and used to aid in alignment of the gages and maintaining the gage position while the epoxy cured. The jig incorporated a two-part clamp to hold the transducer at its base; a recessed portion for the transducer gage area, with raised ledges at the gage level to allow positioning of a thin strip of cellophane tape for alignment; and a pressure plate mounted on dowels that minimized side-to-side motion when clamping force was applied over the

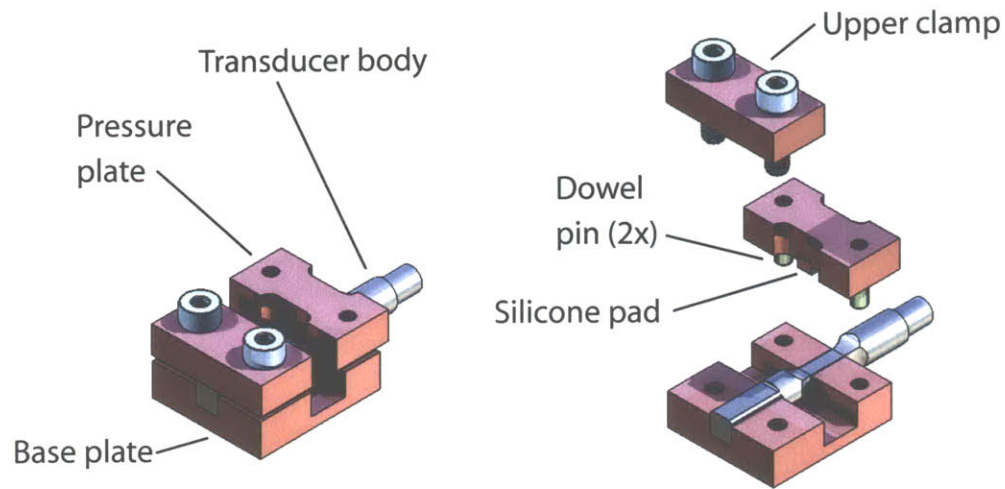


Figure 4-9. Assembled (*left*) and exploded (*right*) views of the strain gage bonding fixture assembly.

gage. Silicone rubber pads cut to match the gaged area were fit into recesses on the base and pressure plate, and Teflon tape was wrapped around the ledge areas perpendicular to the gage face to minimize the adhesion of excess epoxy.

Alignment of the gage and application of epoxy were performed manually under a surgical microscope. After the gage was secured with tape over the epoxy, the pressure plate was carefully lowered onto the gage face and the assembly clamped together with a spring clamp. The epoxy was cured by placing the assembly in a vacuum oven at 100° C for at least 60 minutes. Figure 4-10 shows a transducer in the bonding jig at this point after one gage has been bonded. The bonding process was repeated four times for each transducer, once for each gaged face. A surgical carbon steel blade was used to remove epoxy flash from adjacent un-gaged faces of the transducer before the remaining bonding runs; the full cleaning procedure, starting after the sanding steps, was performed immediately before gage bonding on each face. After all gages were bonded and electrical connectivity verified, the gaged areas of the transducers were sealed with two coats of solvent-thinned nitrile rubber (Vishay M-Coat B) to protect the strain gages and epoxy from physical damage and environmental degradation.

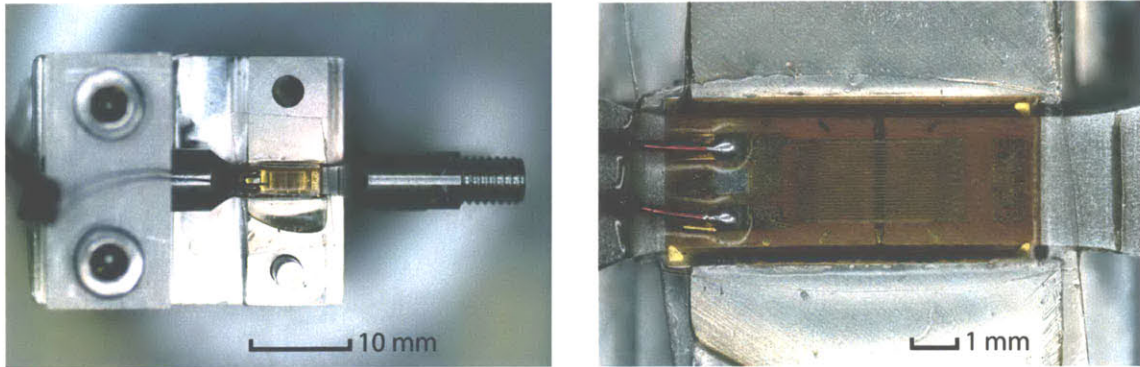


Figure 4-10. Strain gage bonding fixture and bonding results. *Left*, transducer body mounted in fixture with one gage bonded and cured. *Right*, Close-up of bonded gage. The dark line at center, approximately 200 μm wide, is the alignment reference machined on the EDM. The cellophane tape used to position and hold the gage in place during cure is visible.

4.4.5 Transducer electrical connections

The transducer strain gages were arranged to form two half-Wheatstone bridges, with precision bridge completion resistors (Vishay VHP202, $350.0 \Omega \pm 0.01\%$ [62]) for the inactive side of the bridge mounted on a small circuit board adjacent to the base of the transducer. Calex 162MK signal conditioning units (Calex Corp., San Jose, CA), one per axis, were used to provide a power source for each bridge and to amplify the low-level signal before transmission to the DAQ system. The signal conditioning/amplifier units incorporate a stable voltage source including remote sense lines for 6-wire connections, an instrumentation amplifier circuit with adjustable gain, and a second-order low-pass filter bank with selectable cutoff frequency (10 Hz / 100 Hz / 1 kHz) [63]. The filter cutoff frequency was set to 10 Hz to minimize noise in the static and quasi-static experiments reported below. Nominal gain for each amplifier was set at 835 with an external 120Ω precision high-stability metal foil resistor (Vishay PTF-56, tolerance = $\pm 0.05\%$, temperature coefficient = $5 \times 10^{-6}/^\circ\text{C}$ [64]).

All signal connections to the terminals of 162MK signal conditioning units were made with twisted wire pairs. A custom-made highly twisted (3.5 mm/twist, versus 35 mm/twist typical for instrument cable) shielded cable was used for the bridge

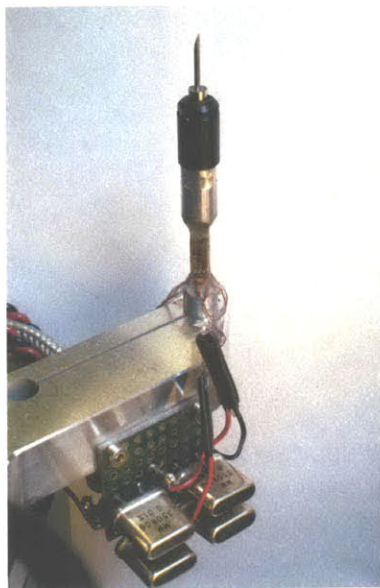


Figure 4-11. Transducer assembly with wiring in place. Precision bridge completion resistors are visible mounted on the circuit board at bottom.

output signal between the bridge and the amplifier input terminals, and commercial shielded, twisted-pair cable was used to connect the amplifier outputs to the data acquisition system. A completed transducer unit with all electrical connections made is shown in Figure 4-11, and with additional hardware visible in Figure 4-12.

Bridge excitation voltage was manually set to 5 V for each signal conditioning/axis unit. Although a higher excitation voltage would increase the bridge output, excessive power dissipation in the strain gages would lead to unacceptable self-heating with noticeable thermal effects on the transducer output. The 200 mW dissipation through each gage ($8.9 \times 10^3 \text{ W/m}^2$ for the $2.8 \text{ mm} \times 8 \text{ mm}$ gage dimensions) served as a conservative limit based on the self-heating recommendations presented in the literature [48].

4.5 Data acquisition hardware

A National Instruments PCI-6289 multifunction data acquisition (DAQ) system collects all transducer data and handles timing control signals for the overall synchronization of the imaging and motion control systems. The device offers 16 differential

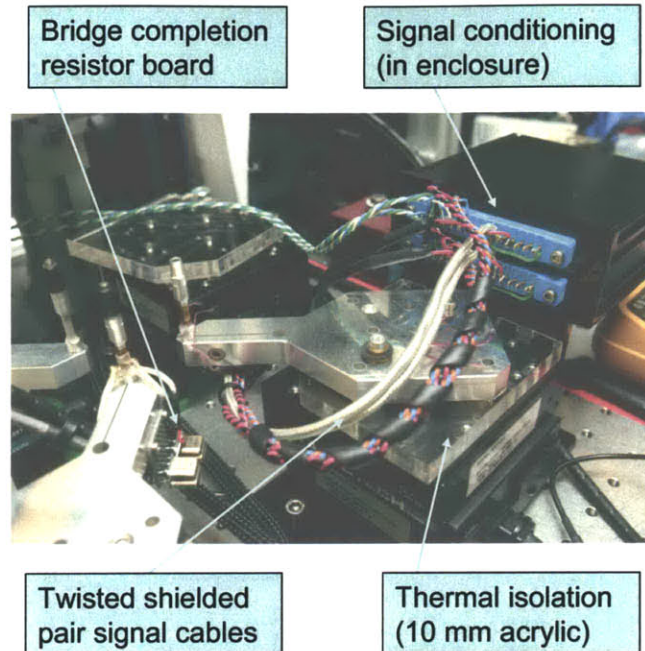


Figure 4-12. Overview of transducer assembly, mechanical components, and signal conditioning hardware mounted on motion stage.

analog input channels, sampling rates of up to 500k samples/s in multichannel acquisition mode, and 18-bit analog-to-digital conversion resolution [65].

Analog and digital connections between the individual instrument components and the PCI-6289 DAQ system are made through a National Instruments SCB-68 connector block, which interfaces to the first eight differential A/D channels of the DAQ device. The connector block provides shielded screw-terminal connections along with a prototyping breadboard area for addition of signal-conditioning circuitry. Additional connections (for the remaining eight A/D channels and additional digital I/O) are made through an SC-2345 configurable signal conditioning enclosure, which offers various plug-in signal conditioning modules for analog and digital input and output. SC-RTD01 signal-conditioning modules with integrated amplifiers were used to amplify RTD voltages for temperature readings during portions of the testing; and a variety of other modules and connections could be envisaged.

The data acquisition card is controlled directly from the instrument control software application using the NI-DAQmx device drivers and associated .NET classes.

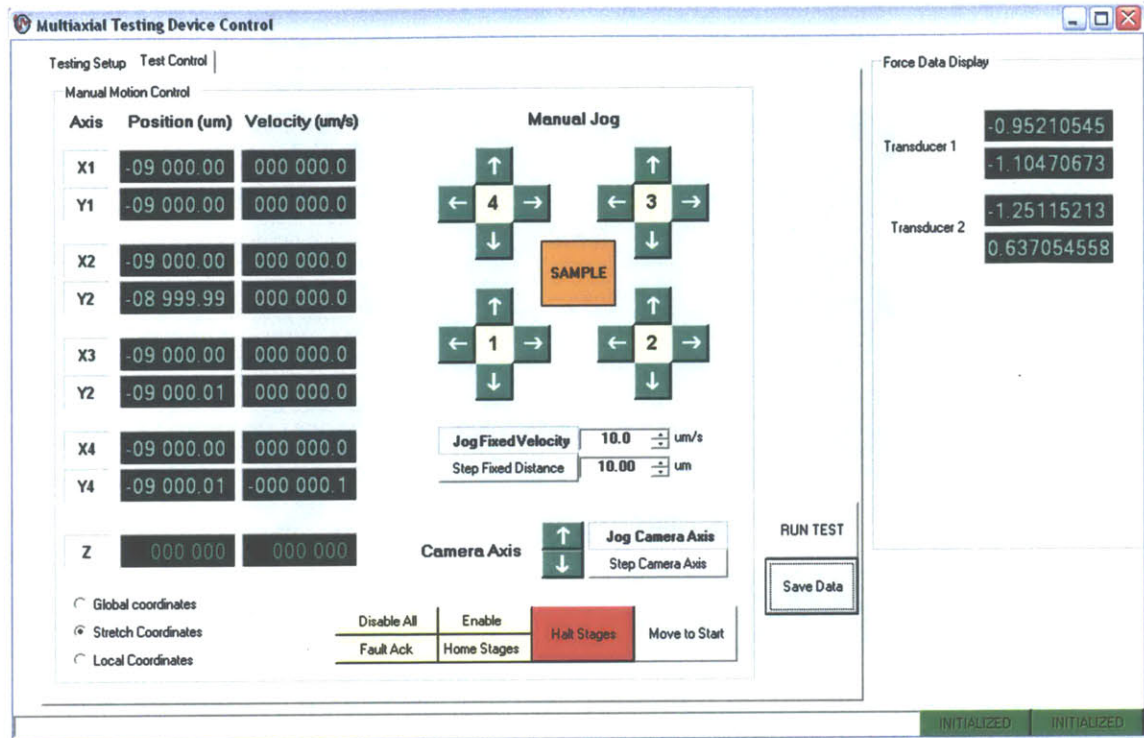


Figure 4-13. Control software user interface.

4.6 Software and integration

An instrument control application was written in Visual Basic .NET 2003 and was run on a PC workstation (Dell Dimension XPS, 3.2 GHz Pentium 4, 2 GB RAM). The control application provided an interface to every component of the testing system, through .NET classes provided by Aerotech, Apogee, and National Instruments for motion control, CCD camera, and data acquisition hardware, respectively.

The graphical user interface of the control application (Figure 4-13) provides an environment for specifying test mechanical and data acquisition parameters; manual motion control for pre-test positioning of the actuators; manual image acquisition to test focus and camera function; and monitoring of motion axis position and transducer output data before and during testing. The application coordinates data collection from the DAQ system during testing and saves force transducer and image data to text and binary files, respectively, for post-test analysis.

Chapter 5

Testing and Validation

Before using a new analytical system to examine properties of unknown materials, the individual components must first be characterized and the results from testing a known material confirmed. For the initial evaluation of the system, the performance of the two-axis force transducers was comprehensively quantified. Thereafter, a simple biaxial test could be performed on a material with known mechanical properties to assess the overall function of the system. In parallel, a finite-element simulation of the physical test was developed to provide a control for comparison to the initial experimental results.

5.1 Force transducer characterization

Each axis of two force transducers was calibrated to quantify the voltage-force relationship prior to the first mechanical testing experiments. Known loads were applied to the transducers at the base of the pins, where the material under test would be attached, by hanging known masses via a string and pulley system. Analysis of the transducer output gave key performance metrics including sensitivity, response vs. angle of applied force, and linearity of response. The sensitivity data also could be compared to the transducer design parameters (see Section 3.2.3) to provide a check on the design process.

In each force calibration test, commercial balance masses were used to provide

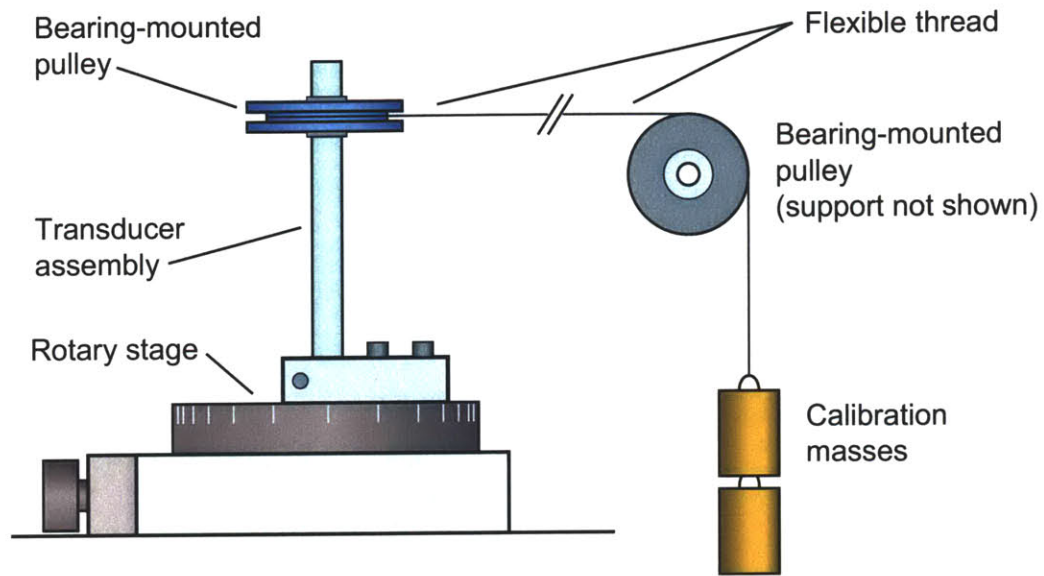


Figure 5-1. Schematic of transducer calibration assembly, set up for the first round of calibration experiments. The transducer assembly (details omitted for clarity) is rotated about the transducer axis on the rotary stage to vary the angle of application of force.

the known loads. Each mass was measured prior to the tests with a digital analytical balance (Mettler-Toledo AG204 DeltaRange, 210 g capacity / 1 mg resolution; Mettler-Toledo Inc, Columbus, OH). A custom-machined Delrin pulley mounted with a shielded ABEC-5 ball bearing carried the flexible braided gel-spun polyethylene thread (The Orvis Company; Roanoke, VA) that transmitted the hanging load (Figure 5-1). Initial experiments showed that bearing friction/stiction in the pulley assembly fell below the range of the lowest measured load.

Calibration was carried out in two steps to assess the full range of transducer performance in measuring static loads:

- Response of the x and y axis outputs to loads at varying angle in the plane of the transducer; and
- Response of x and y axis outputs of each transducer to in-plane loads along the transducer axes.

Both tests were performed initially on the first prototype version of the transducer (transducer V1), which was manufactured specifically as a performance testbed and proof of concept. This transducer was designed for mounting onto a rotary stage for the angular response testing, which required a slightly different mechanical configuration than in the final design; and had a simplified upper section without the pin and collet details of the final transducer units. With the fundamental concept proven in the first set of tests, the orthogonal load tests were performed on the final transducers as mounted in the testing system.

5.1.1 Calibration results: prototype transducer

The first calibration tests involved a prototype transducer mounted on a rotary stage to assess response to loading at all angles in-plane, as well as basic linearity and stability performance. The experimental setup is shown in Figure 5-1. A ball-bearing mounted pulley is mounted to the transducer body, and allows the transducer assembly to rotate freely while the thread that applies the load remains in place. The components described in Section 4.4.5 were used to amplify the output voltage of a full Wheatstone bridge for each axis. For the initial tests, amplifier output voltage was measured with a digital oscilloscope (Fluke 196C Scopemeter; Fluke Corporation, Everett, WA) rather than the PC-based data acquisition system.

A series of tests were first performed with varying load to assess the output response versus applied load for a range of force from 0.20 N to 7.85 N. The data confirmed the linearity of the transducer to within 0.3% of the full-scale output, including hysteresis and drift (Figure 5-2). Subsequently, tests were performed with a constant load of 1.96 N (200 g mass) applied at varying angle by rotating the rotary stage. The output voltage of both axes was measured at 10 degree increments as the stage was rotated through 360 degrees in both clockwise and counterclockwise directions.

A typical plot of the output voltage versus angle of applied load through one complete revolution for both axes of the transducer is shown in Figure 5-3. The output of both axes is described very well by a sinusoidal fit, with a maximum error

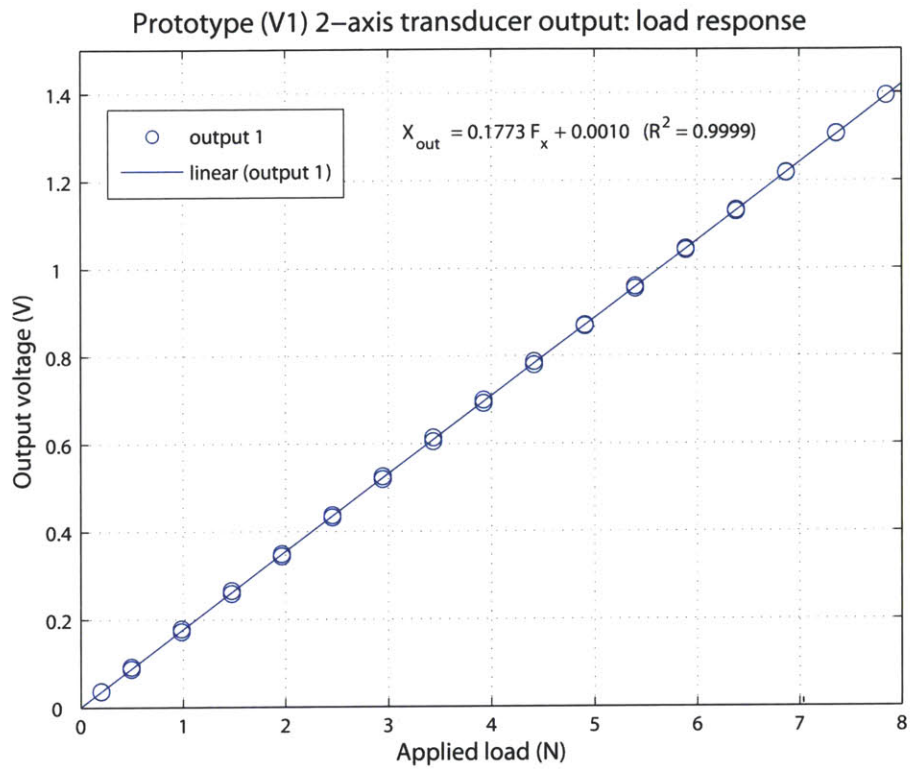


Figure 5-2. Prototype transducer calibration: output versus applied load. Data for increasing and decreasing load are shown and used for the linear fit.

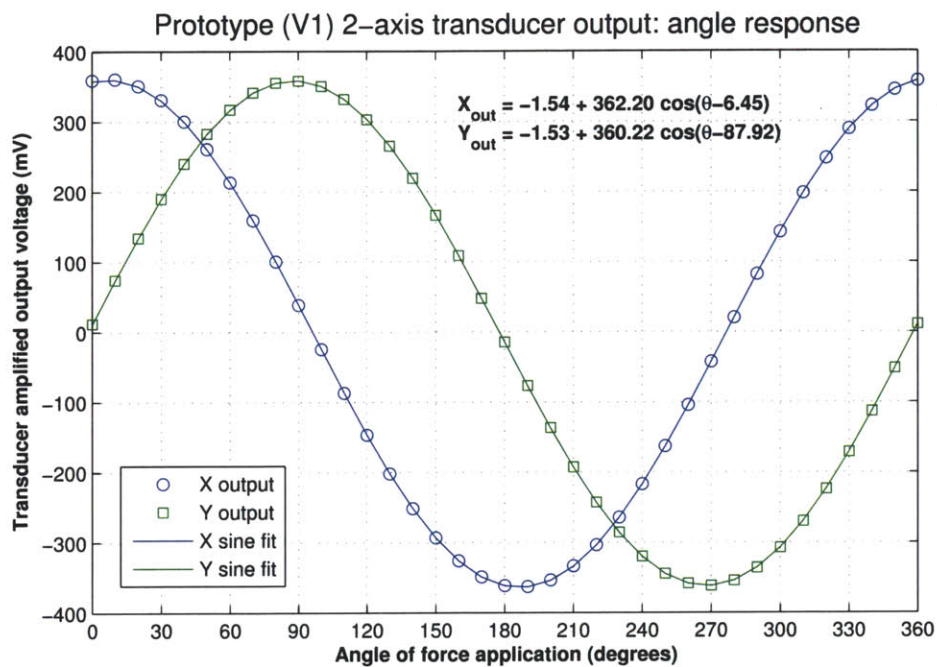


Figure 5-3. Two-axis response of first prototype transducer to constant load at varying angle of application. Experimental data are averages of 3 readings at each point (error bars too small to display). Sinusoidal fit equations shown minimize mean-square error.

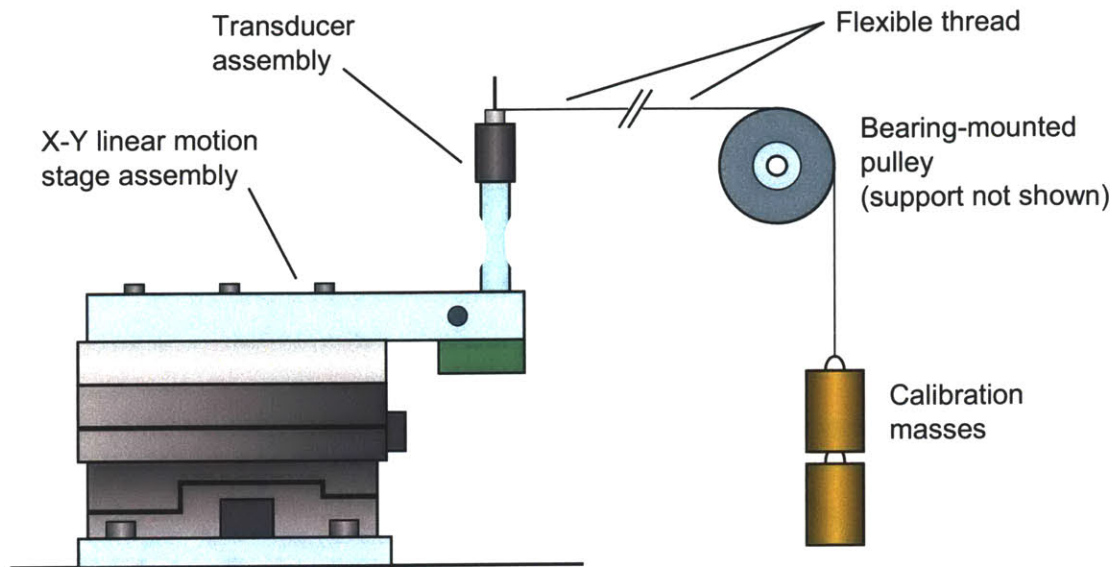


Figure 5-4. Schematic of calibration assembly for the final transducers. The transducer assembly is mounted in place on the linear motion stage assembly; this is repeated with the load applied in both x and y directions by moving the pulley and supports by 90 degrees about the transducer axis on the optical table. The linear motion assembly is used for fine alignment of the force axis.

of less than 0.45 mV (0.12% of sinusoid amplitude). However, the physical axes of maximum sensitivity of the transducer were found not to be orthogonal; rather the angle between them (from the angle offset in the sine fit equations) was approximately 81.5 degrees.¹ This latter effect was attributed to alignment errors in bonding the strain gages, and motivated the design and construction of the strain gage mounting jig described in Section 4.4.4 and used for the final transducers.

5.1.2 Calibration details and results: Final transducers

Calibration testing on the final transducers was performed as mounted in the testing system after alignment of the imaging system and the motion stages. The calibration arrangement was similar to the setup described above for the prototype transducer,

¹In principle, some deviation from orthogonality is allowable, and is trivial to correct for mathematically if accurate calibration and in-test data from both transducer axes is available. See Appendix D, Section D.1, for additional detail.

but with the transducer mounted in the transducer holder on the linear motion stage assembly (Figure 5-4). Each axis of each transducer was subject to a load ramp from zero to 4.9 N and back, with mass applied in larger steps at higher loads. Signal conditioning and data acquisition were performed with the final components described in Section 4.5. For each data point, the transducer amplified outputs were sampled at 2.4 kHz for 2 s, and the 4800 resulting samples averaged. Three data points were acquired at each load step on both ascending and descending legs of the load ramping. An application written in Visual Basic .NET 2003 was used to coordinate the data collection.

The outputs from both axes of both transducers were highly linear and repeatable in applied load, and demonstrated low sensitivity of the transducers to transverse loading (Figures 5-5,5-6). Total nonlinearity and hysteresis were $< 0.1\%$ of full-scale output for all axes. For completeness, higher-order fits of the data were performed as well but the improvement in fit was negligible, as the nonlinearity was almost exclusively dependent on time rather than applied load. Detailed analysis of the calibration data is presented in Appendix D, with selected performance metrics shown in Table 5.1.

Sensitivity vectors of the transducer outputs to in-plane loading are plotted in Figure 5-7. As with the V1 transducer, the outputs of the final transducer were not perfectly orthogonal nor perfectly aligned with the global axes of the system. However, there was a marked improvement from the original as the largest deviation from orthogonality for each transducer was less than 1.7° (1.69° and 0.63° for transducers 1 and 2, respectively), a greater than $5\times$ improvement over the first prototype. As the first prototype demonstrated that the transducer axes produce a near-perfect sine/cosine response with misalignment causing only a phase shift from 90 degrees between axes, the above are sufficient to fully characterize the transducer response—given the sensitivity vectors, the outputs from two axes of each transducer may be used to compute the true in-plane force using a linear transformation. The computation of the transformation matrix is presented in Appendix D.

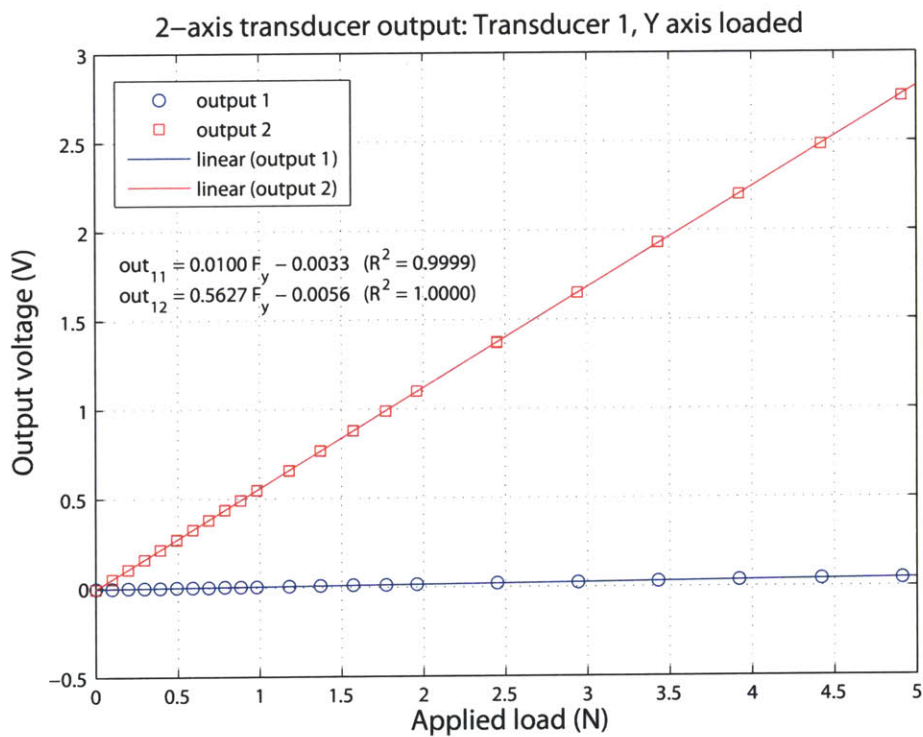
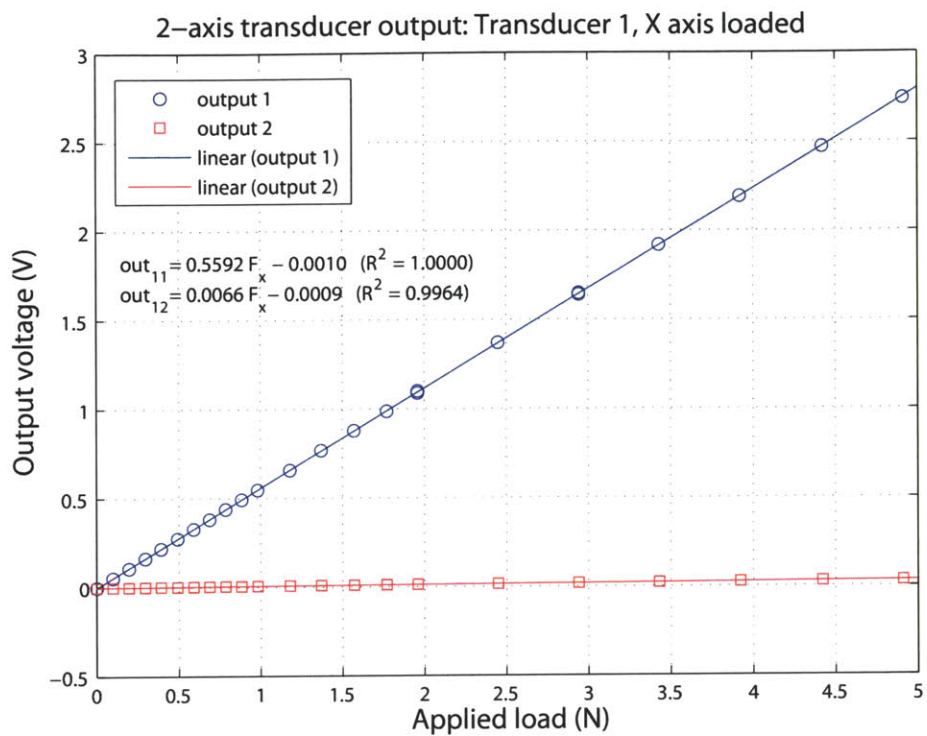


Figure 5-5. Final transducer unit 1 calibration: output versus applied load.

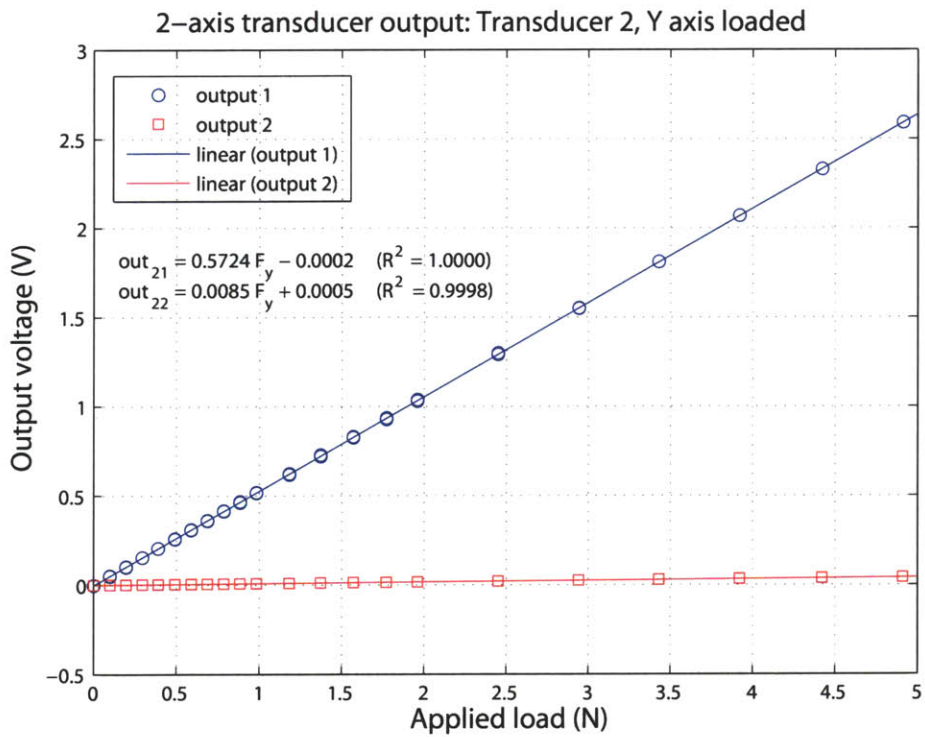
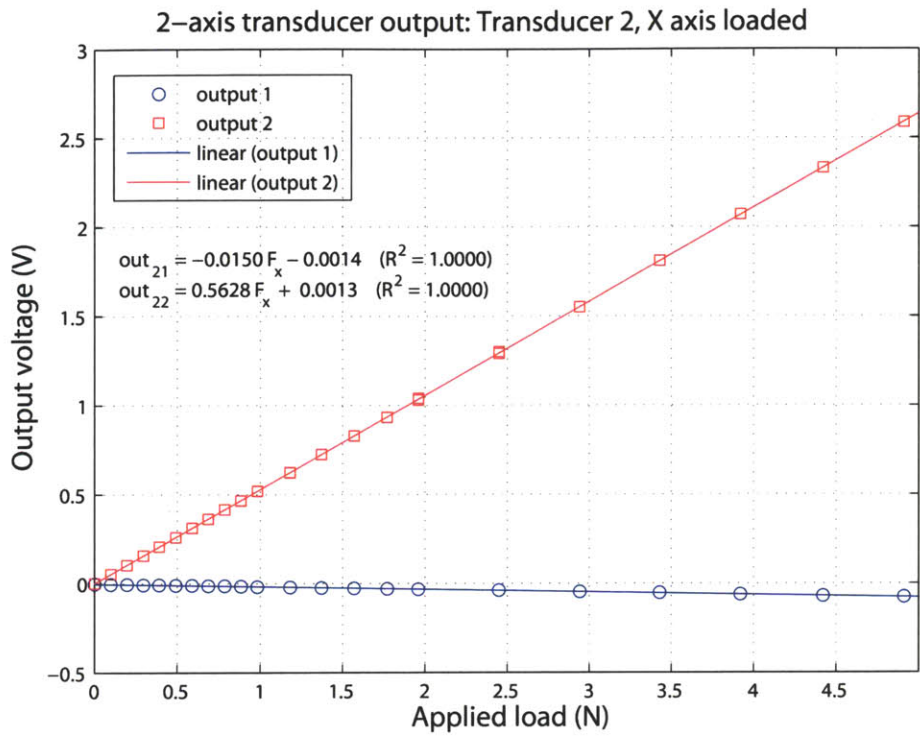


Figure 5-6. Final transducer unit 2 calibration: output versus applied load.

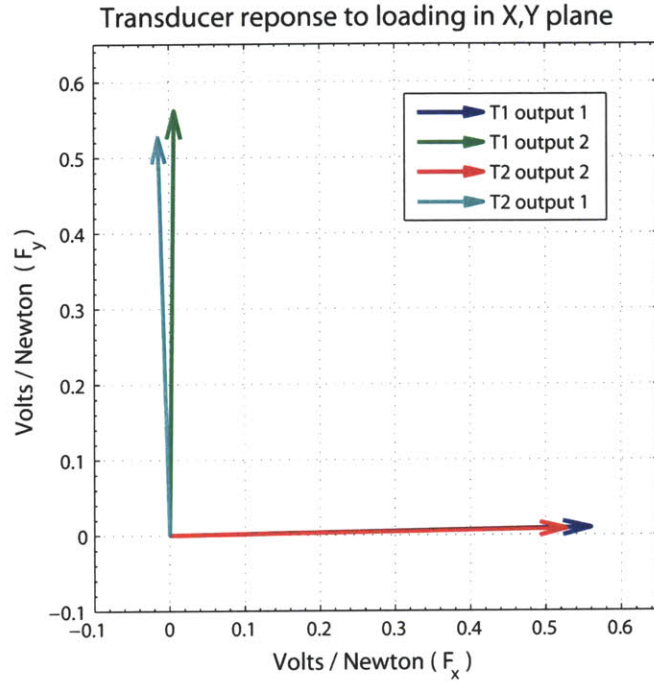


Figure 5-7. Final transducer calibration: response plotted in x - y plane.

Transducer output	Sensitivity (mV/N)		Angle	RMS noise (mV)
	X axis	Y axis		
T ₁₁	559.2	10.0	1.02°	0.51
T ₁₂	6.6	562.7	89.33°	0.49
T ₂₁	-15.0	572.4	91.50°	0.56
T ₁₂	562.8	8.5	0.87°	0.55

Table 5.1. Transducer performance parameters: Sensitivity components for on- and off-axis loading, resulting sensitivity axis, and sampling noise.

5.2 Biaxial testing experiment

To evaluate the initial capabilities of the biaxial materials testing system, the first experiments were carried out on a known elastomeric material with well-characterized mechanical properties. A finite-element model was then constructed to accurately reflect the test conditions (material geometry, boundary conditions, imposed loading) and the results of the finite element analysis compared to the experimental results from the testing instrument. Provided that the parameters of both real and simulated materials and of the real and simulated experiments were sufficiently close, the results of the experiment and the finite element model could be expected to agree.

For simplicity of modeling and interpretation, an isotropic elastic material was chosen for initial testing. To obtain large material deformations while maintaining applied loads within the instrument's force capacity, a soft elastomer was desirable. Natural latex rubber was chosen as the nonlinear mechanical property data available in the literature (e.g. [15]) fall within a narrow range, in contrast to synthetic rubbers and similar materials, which display a strong variability in mechanical properties with varying composition and for which detailed data on chemical composition is typically unavailable from general commercial suppliers.

5.2.1 Equibiaxial testing: physical experiment

For the physical experiment, a 40 mm \times 40 mm square sheet of 1.27 mm thick natural latex rubber (97.3% latex) obtained from a commercial supplier (McMaster-Carr Corporation, Dayton, NJ) was tested. On the central 20 mm \times 20 mm portion of the specimen, a grid of points at 5 mm intervals in the x and y directions was marked with an ink pen. The pin attachment points were initially set at 20 mm separation in the x and y directions, and the rubber sheet was lowered carefully onto the pins at the corner marks of the central 20 mm square.

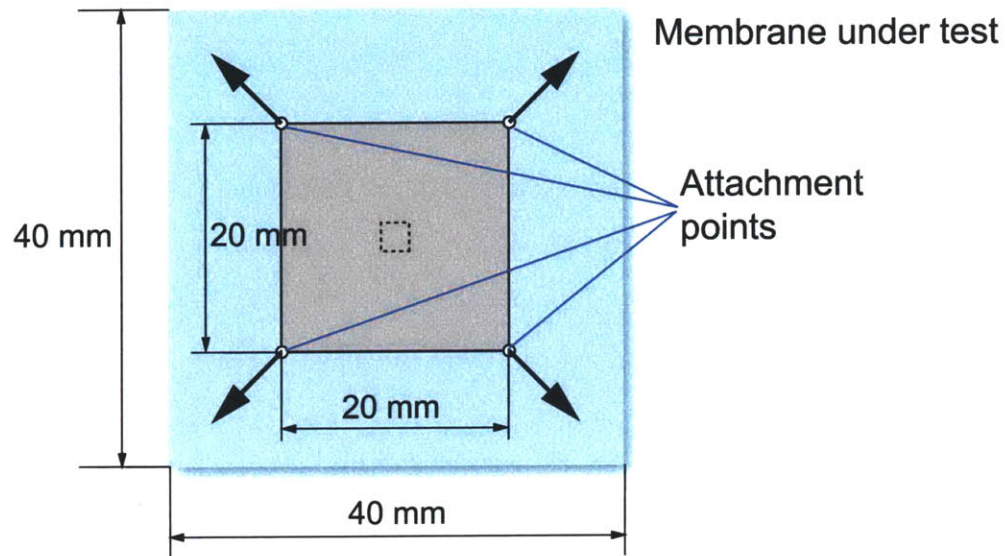


Figure 5-8. Layout of initial biaxial testing experiment. Thick arrows indicate direction of force application and attachment point displacement. The shaded region is the area of interest for assessing material properties; the central box illustrates the size of the area with minimal strain variation where non-full-field material deformations are typically measured in biaxial testing.

Test protocol

The membrane test involved stretching the rubber sheet from the initial reference state by displacing each attachment point 1 mm in both x and y directions away from the center of the membrane (Figure 5-8). All stages moved simultaneously under position control at a fixed rate of $10.0 \mu\text{m/s}$ (velocity of each attachment point = $14.1 \mu\text{m/s}$), for a total test duration of 100 s.

For the initial test, two of the four attachment points functioned as force transducers, with mechanically identical but uninstrumented assemblies at the remaining two attachment points. With an isotropic material tested under symmetric loading conditions, symmetry in force and displacement response was expected and the limited instrumentation deemed sufficient.

Data from both axes of each force transducer was collected at 2400 Hz, with sets of 40 consecutive samples averaged and the resulting data saved at 60 Hz. Full-field images were acquired with the camera and saved every 10 s, for a total of 11 images including the initial and final positions and nine intermediate steps.

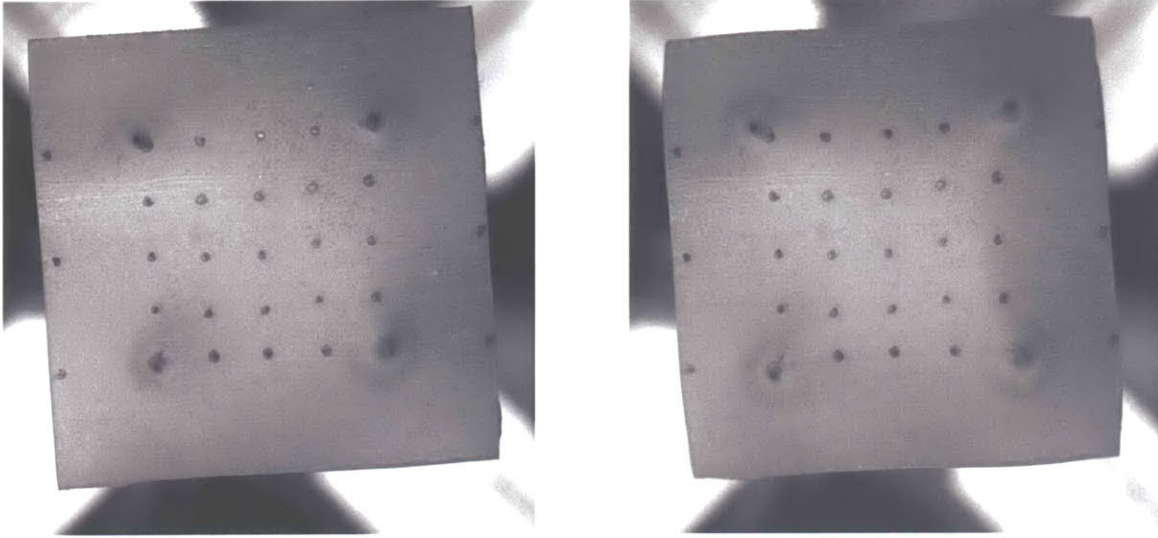


Figure 5-9. Images of the membrane under test in initial undeformed (*left*) and final (*right*) configurations. Dots on the membrane surface are ink markers tracked for comparison with the finite element model.

Force and displacement data were analyzed after the experimental run. Force transducer output voltage levels were converted to force units and plotted against time. Manual measurements were made of the marker positions on the membrane using commercial image-processing software (Adobe Photoshop 7; Adobe Inc, San Jose, CA). X and y pixel coordinates of the centers of the 16 marked points were collected from the initial and final images; the vector displacements between initial and final positions were computed for all points and converted into distance units by scaling from the initial known distances between attachment points.

Test results

Images of the rubber membrane in initial and final configurations are shown in Figure 5-9. Deformation of the membrane increases from the center toward the attachment points, as evidenced by the motion of the marker dots between images. (The motion of the markers through the course of the experiment is illustrated in Figure 5-10.) Some rotation of the specimen axes (as defined by the ink markers) relative to the image and global coordinate frame is clearly visible in both images, but the magnitude of rotation remained nearly constant throughout the experiment.

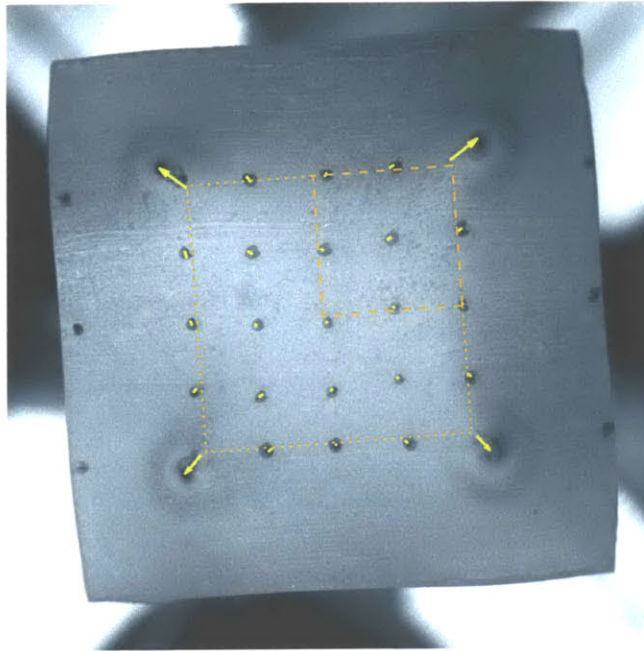


Figure 5-10. Vector displacement of marker points in the biaxial experiment, overlaid on the deformed membrane image. Arrows originate at the respective marker locations in the undeformed geometry and terminate at the marker locations in the deformed state. Dotted lines delineate the approximate locations of the central 20 mm \times 20 mm area (see Figure 5-8, and the 10 mm \times 10 mm section modeled in the finite element analysis (Figure 5-12).

The edges of the membrane also appear to contract at the corners with applied load; however this is an illusion due to the unsupported membrane bending out of plane where not subject to tension, as confirmed visually during the experiment.

Figure 5-11 shows the time history of the vector forces from the two instrumented attachment points through the duration of the test. The increasing trend for both attachment points displays some curvature, with two inflection points as expected for a hyperelastic material. The membrane was somewhat difficult to load onto the pin attachments at the start of the experiment, and the difference in force magnitude and direction between the two transducers may be due to the resulting alignment errors. The finite element model and results discussed below provide a basis for comparison.

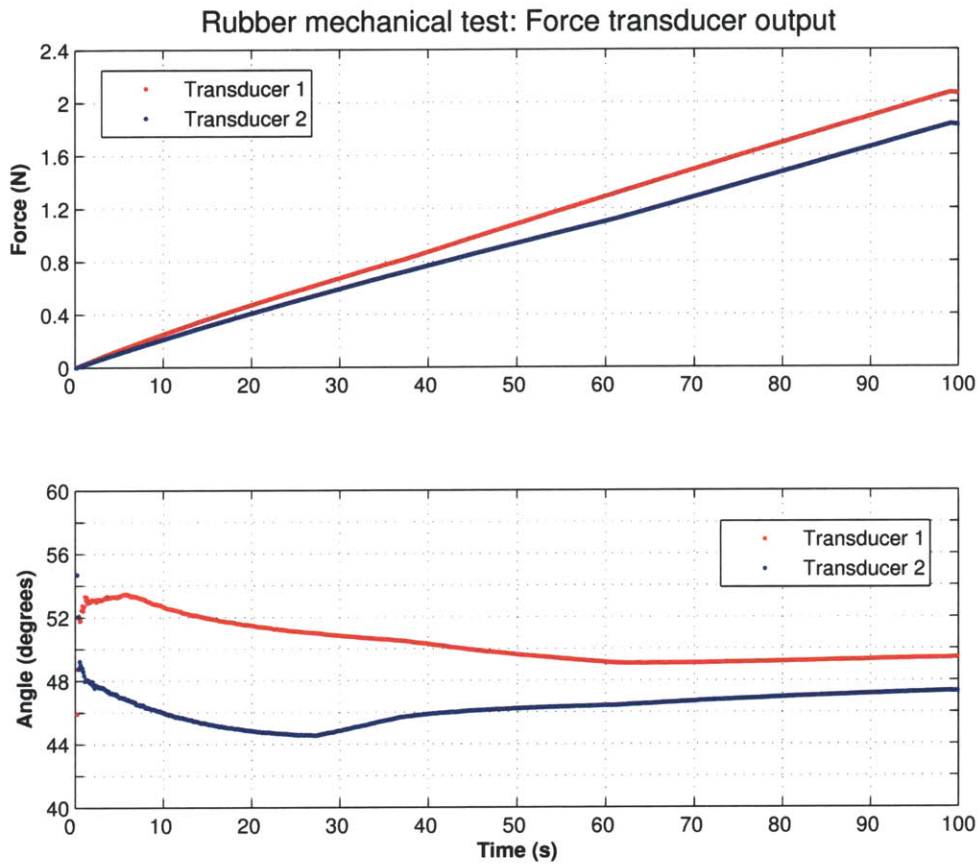


Figure 5-11. Force data from the rubber biaxial extension test. Force magnitude (*top*) and direction (*bottom*, angle relative to x axis) for each attachment point was computed from the 2-axis data from each transducer. (Angles have been rotated into the same quadrant for clarity of scale. In reality forces were approximately 90 degrees orthogonal; data from transducer 2 would be displaced by -90 degrees in this plot.)

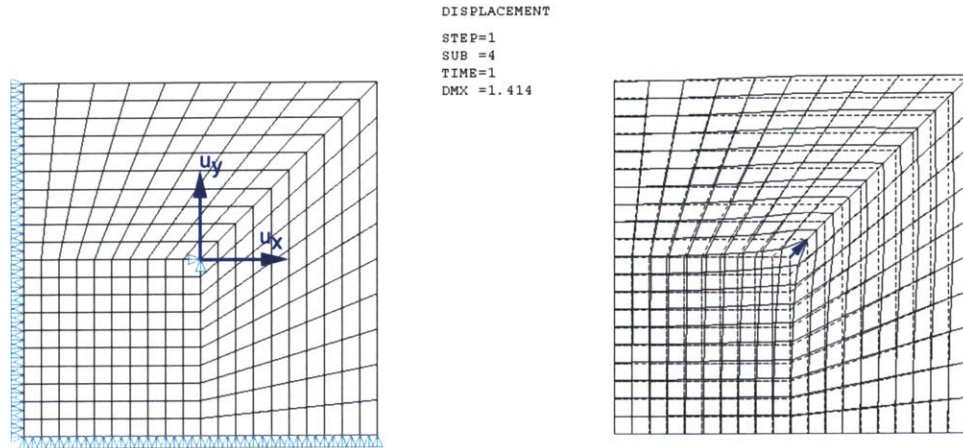


Figure 5-12. Finite element model: mesh, loading, and deformation. *Left*, undeformed mesh showing symmetry boundary conditions (left and bottom edges) and point of load application. *Right*, deformed geometry (solid lines) superimposed on undeformed geometry (dashed lines). Arrow at center illustrates displacement of the attachment point.

5.2.2 Finite element analysis

A finite-element model developed to parallel the physical test was implemented using ANSYS 9 (Ansys Inc, Canonsburg, PA). Because of the assumed material isotropy, geometric symmetry, and symmetry of applied loading, one quarter of the sheet under test was modeled with appropriate boundary conditions used to impose the symmetry constraints. The pin attachment was modeled as a point load. The geometry, constraints, and loading along with the element mesh are shown in Figure 5-12.

Eight-node biquadratic plane stress elements (ANSYS element type PLANE183 [66]) were used in the finite element simulation. The rubber sample material properties were specified using a two-term Mooney-Rivlin hyperelastic material model, with properties taken from [15] and shown in Table 5.2. Rubber exhibits substantial material nonlinearity, so for an accurate model including realistic response to stress concentration at the loading points, large-deformation effects must be included, using an iterative nonlinear solver (NLGEOM solution option in ANSYS). For this simulation, four substeps were required for convergence to a solution.

Source	C_{10}	C_{01}
Makino <i>et al.</i> [15]	134.36×10^3	12.49×10^3
Oden and Kubitzka [67]	111.79×10^3	13.73×10^3

All values in N/m^2

Table 5.2. Mooney-Rivlin material constants for natural latex rubber, computed from inflation testing data by separate groups. The coefficients from [15] were used in the finite element model.

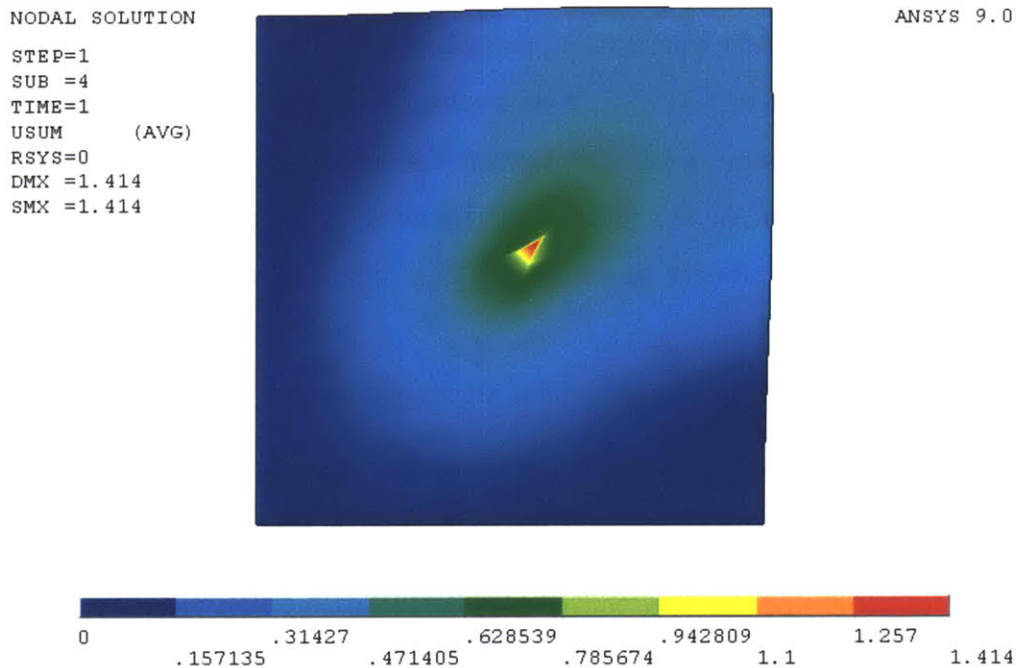


Figure 5-13. Finite element simulation results: Displacement magnitude field. Displacement tapers off from the maximum of 1.41 mm (the imposed boundary condition at the center) to <0.15 mm at the model edges.

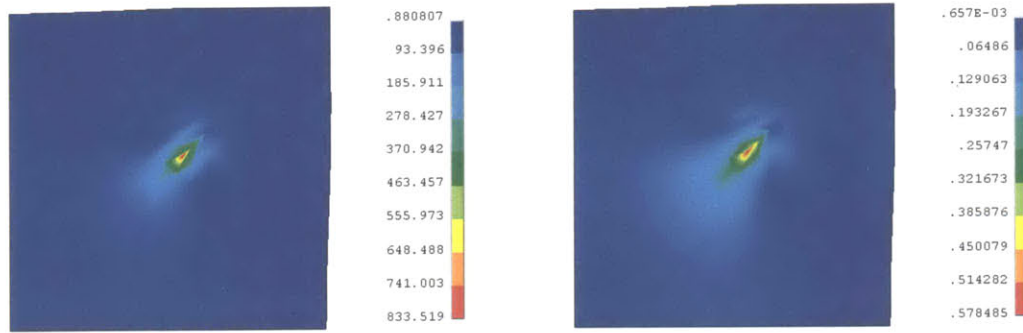


Figure 5-14. Von Mises stress (*left*) and first principal strain (*right*) in the finite element experimental simulation. A prominent stress concentration exists at the pin attachment point (point displacement constraint). Stress in kN/m^2 , strain in engineering units.²

The results of the finite element simulation are shown in Figures 5-13 and 5-14. The displacement boundary condition on the attachment point enforces the maximum displacement magnitude of 1.41 mm, with displacement tapering off sharply near the attachment point and more gradually toward the center of the sample. The peak stress of $8.3 \times 10^5 \text{ N/m}^2$ in the vicinity of the attachment point is well below the $2.8 \times 10^7 \text{ N/m}^2$ tensile strength of natural rubber.[68]

5.2.3 Experiment / analytical comparison

The displacement response predicted by the finite element analysis corresponded closely with the observed experimental response (Figure 5-15). For points excluding the model boundary, the mean measured displacements and the finite element model agreed to within 12% ($30 \mu\text{m}$), with the model boundary points showing slightly larger absolute discrepancies ($< 50 \mu\text{m}$), although this was on the order of the displacements themselves at these points.

At the attachment point, the measured displacement was nearly 40% greater than the true displacement. (For the attachment point, the finite element model dis-

²In large-deformation analysis, the principal strains ϵ_i are defined from the principal *stretches* λ_i ($i = 1, 2, 3$) which are the eigenvalues of the right stretch matrix \mathbf{U} (equivalent to the deformation gradient when rotation is absent): $\epsilon_i = \lambda_i - 1$. [66]

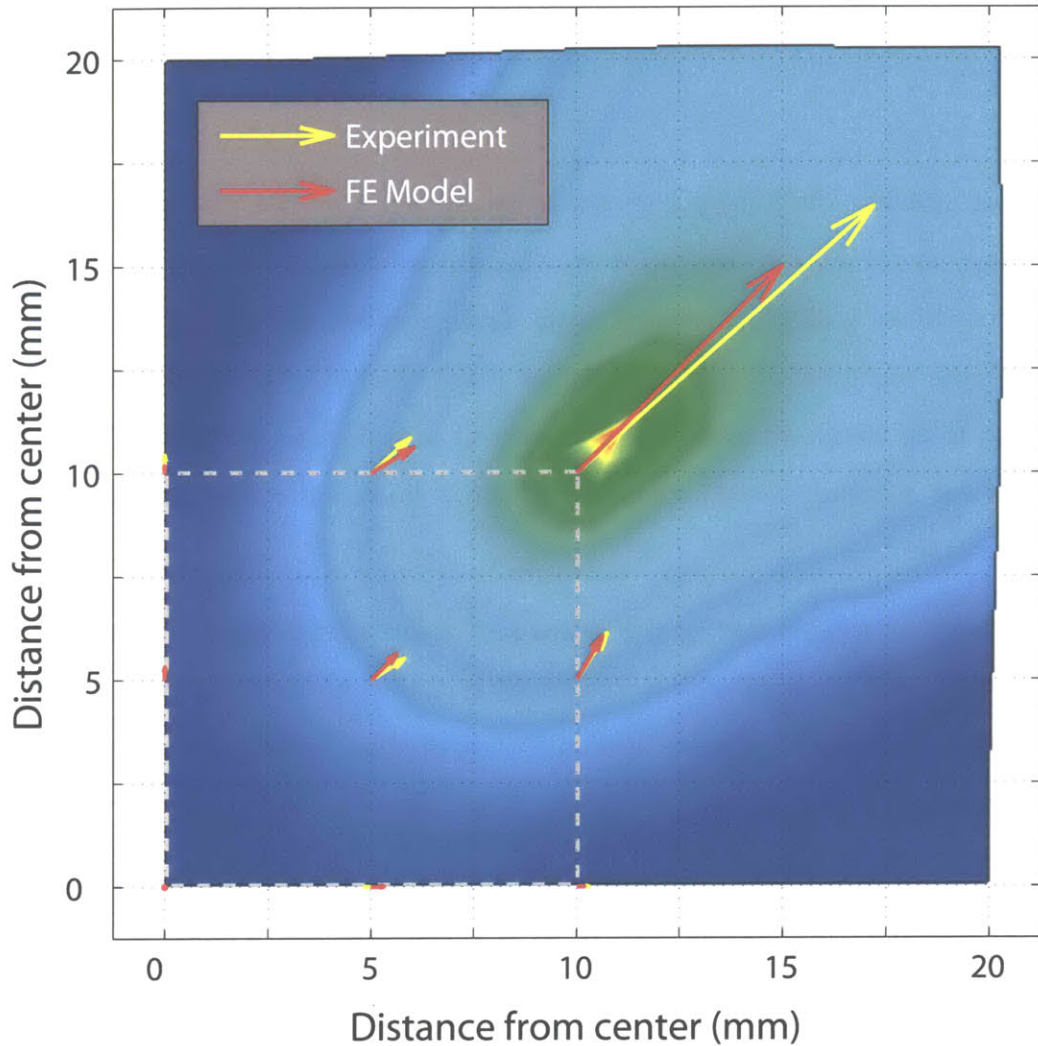


Figure 5-15. Vector displacement of markers in biaxial experiment, superimposed on a contour plot of deformation magnitude from the finite element model. Experimental displacements are averaged from corresponding points across all four quadrants of the test specimen. Arrows have been scaled by $5\times$ relative to the distance scale to exaggerate contrast between model and experiment. (Dashed box corresponds to the small dashed box in Figure 5-10.)

	Experimental Data		Finite Element Analysis
	Transducer 1	Transducer 2	
Reaction force magnitude	2.07 N	1.83 N	0.975 N
Reaction force angle	49.8°	42.7°	45.0°

Table 5.3. Reaction forces at the transducer attachment points, as measured experimentally and as predicted by the finite element model.

placement matches the known true displacement fixed by the motion stages.) The discrepancy at the attachment point may be due to difficulty of accurately locating the ink marks in a highly distorted area of the membrane, not only from the imposed stretch but from the pin attachment itself. The full-field strain measurement algorithm to be implemented in the next step of development is expected to improve measurement accuracy overall compared to the tedious and coarse manual technique used presently.

Reaction forces computed by the model and observed experimentally are shown in Table 5.3. Despite the similarity in deformation data between model and experiment, the experimental force results are approximately double the finite-element model predictions for both transducers.

A number of explanations could account for the discrepancy in force data between the model and the experiment. First, it is likely that the 2-term Mooney-Rivlin material model does not sufficiently take into account strain stiffening of the rubber membrane at large strain. Stretch ratios of $\lambda \sim 1.5$ are typical upper bounds of validity for the 2-term model, with higher-order models necessary at larger strains. In addition, the limited spatial resolution of the finite element model may prevent the model from accurately capturing the severe stress concentration effects at the loading point. Finally, the difference in attachment conditions between the experiment and the analytical model (a pin piercing the membrane versus the artificially imposed point constraint) means that the initial conditions are not equivalent—the model has zero initial loading whereas the prestress caused by the pin in the membrane is likely to stiffen the real material under test.

5.3 Finite element considerations

Prior to the above simulation, a number of attempts were made to model the effects of the pin attachment with a central hole in the mesh at the loading point. Several tactics were attempted, including defining a circular hole of the pin diameter with displacement constraints placed on various parts of its edges; and imposing a sliding contact constraint on the membrane against a rigid cylinder in such a hole. None of these attempts brought success in accurately reflecting the physical response of the rubber deforming around the pin in the experiment. Simulations were also performed to ascertain the circumferential and radial pre-stress in the material at the attachment point due to the pin, but no way was found to transfer the results of these analyses as initial conditions to the planar model. As the overall material response beyond the immediate vicinity of the attachment point showed little difference between these complicated attempts and the point constraint in the analytical solutions, the latter was favored for simplicity.

Chapter 6

Conclusion and Further Work

The present thesis describes the design and construction of a flexible multiaxial materials testing system. This instrument provides the foundation for a sophisticated biaxial testing platform for probing the properties of anisotropic, inhomogeneous membrane materials, including biological specimens and novel synthetic materials. Initial testing has demonstrated the basic functionality of the design and provided a thorough characterization of its components.

Specific capabilities demonstrated and detailed in this thesis include high resolution force measurements from custom-built two-axis transducers, flexible 2D motion profile definition of the attachment points with high-velocity linear motion stages, and the potential to acquire full-field strain data from sensitive high-resolution imaging of the material under test. The two-axis force transducers developed for the present system offer a higher load/sensitivity ratio than any comparable device reported in the literature.

6.1 Limitations

In the course of testing and validating the performance of the present system, several limitations have come to light. These are discussed below as a basis for improving upon aspects of the present instrument in upcoming design iterations.

The camera presently employed for full-field imaging, while offering excellent dy-

dynamic range at high resolution, is hampered by a relatively slow shutter mechanism which limits the maximum velocity of the material under test and effectively restricts its use to quasi-static testing or measuring creep phenomena. Every other component of the system—the transducers, linear motion stages, data acquisition, and control software—all support orders of magnitude faster operation.

To overcome the limitation on camera speed, the present camera would ideally be replaced with one that offers an electronically-shuttered CCD sensor rather than requiring a separate mechanical shutter. While mechanical shutters in single-lens-reflex cameras offer several times the speed of the present mechanism (8 ms full opening or 125 μ s moving curtain, versus 30 ms minimum opening for the present camera), electronic shutters offer exposures of as little as 50 μ s in presently available high-resolution (2048 \times 2048) CCD cameras.[69] The only drawback in this case is reduced dynamic range compared to the slower, large-pixel camera presently in use.

Additionally, if the requirement on resolution and dynamic range could be relaxed somewhat, high-speed buffered cameras are available that offer continuous frame rates in the 10,000 frames/s range for short bursts, albeit at lower resolution and substantially reduced dynamic range. At present, analyzing thousands of full-field images to extract strain data, and subsequently using each imaged configuration as an input to a parameter estimation routine for estimating material properties, would present a prohibitive cost in computational time and resources. However, the raw high-speed images and force data certainly could lend themselves to the investigation of various rate-dependent phenomena using alternate analytical methods.

One additional and substantial design issue with any biaxial testing system is the development of stress concentrations in the membrane at the loading points or elsewhere in the membrane due to the specimen geometry. There is an inherent trade-off between the point loading that is required for accurate knowledge of the applied loads and an accurate model of the material under test, and the degree of stress concentration at and near the loading points.

6.2 Extensions and future work

A number of extensions to the present work are envisaged that would bring the present instrument to full functionality and expand its capabilities. These are presented below in brief.

6.2.1 Full-field strain measurement

Full-field strain measurement is a prerequisite for fitting a finite element model to the observed material deformations across the entire specimen. The device at present has all the components and framework required for full-field strain analysis; all that remains is implementing an existing algorithm (e.g. the technique presented by Malcolm *et al.* [43]) in code and integrating it into the control software.

6.2.2 High-speed testing

Most existing biaxial testing systems are used for quasi-static or low-rate testing, in part due to limitations in their components. The present system incorporates transducers, motion stages, and data acquisition hardware that are all capable of highly dynamic testing, which could provide exciting new insights into the behavior of various materials. To realize this goal, the control software would need to be modified in some locations and a high-speed camera installed in place of the high-dynamic-range unit. In addition, it would be desirable to modify the signal conditioning/amplifier circuitry for the force transducers—for instance, including using purpose-built low-noise amplifiers with higher dynamic performance and implementing bandpass filtering in the amplifier hardware—to optimize the system for dynamic testing.

6.2.3 Environmental control

The present testing system is designed with the application to the difficult constitutive laws of biological materials and novel polymers in mind. For a variety of applications, environmental control—either in the form of a fluid environment, or a

controlled humidity and/or temperature chamber—would be desirable. The transducers themselves would function in a fluid environment, but a number of design changes would be necessary, including the addition of the fluid bath or chamber, inverting the transducers for an immersed test, and possibly reorienting the camera to measure from below a window in a fluid bath, as in the apparatus shown in Figure 2-3.

6.2.4 Integrated modeling and testing

In the long run, the “holy grail” of mechanical testing with full-field strain measurement and finite-element-based computations of material properties would be a device with the ability to perform system identification to determine the constitutive law of the material and to perform optimization on the constitutive law definition while the experiment is in progress. With this capability, the experimental parameters could be adjusted on the fly and the test tailored to the specific material sample even without any of its mechanical properties being well characterized beforehand. Such a system would be prohibitively costly in terms of computational power at present, but might in the future become a viable option, perhaps based on similar physical components to the present instrument.

References

- [1] Y. C. Fung. *Biomechanics: mechanical properties of living tissues*. Springer, 1997.
- [2] V. P. Novak, F. C. Yin, and J. D. Humphrey. Regional mechanical properties of passive myocardium. *Journal of Biomechanics*, 27(4):403–12, April 1994.
- [3] R. K. Krishnaswamy and M. J. Lamborn. Tensile properties of linear low density polyethylene (LLDPE) blown films. In *ANTEC 2000 Plastics: The Magical Solution, Volume 1: Processing*. Society of Plastics Engineers, 2000. Available from: <http://www.knovel.com/knovel2/Toc.jsp?BookID=67&VerticalID=0>.
- [4] S. Jin, S. Cong, G. Xue, H. Xiong, B. Mansdorf, and S. Z. D. Cheng. Anisotropic polythiophene films with high conductivity and good mechanical properties via a new electrochemical synthesis. *Advanced Materials*, 14(20):1492–1496, October 2002.
- [5] N. Mateeva, H. Niculescu, J. Schlenoff, and L. R. Testardic. Correlation of seebeck coefficient and electric conductivity in polyaniline and polypyrrole. *Journal of Applied Physics*, 83(6):3111–3117, March 1998.
- [6] Y. Lanir and Y. C. Fung. Two-dimensional mechanical properties of rabbit skin. I. Experimental system. *Journal of Biomechanics*, 7(1):29–34, January 1974.
- [7] Y. Lanir and Y. C. Fung. Two-dimensional mechanical properties of rabbit skin. II. Experimental results. *Journal of Biomechanics*, 7(2):171–82, March 1974.

- [8] W. Sun and M. S. Sacks. Finite element implementation of a generalized Fung-elastic constitutive model for planar soft tissues. *Biomechanics and Modeling in Mechanobiology*, In Press:, 2006. Published online August 2005. Available from: <http://www.springerlink.com/openurl.asp?genre=article&id=doi:10.1007/s10237-005-0075-x>.
- [9] W. Sun, M. S. Sacks, and M. J. Scott. Effects of boundary conditions on the estimation of the planar biaxial mechanical properties of soft tissues. *Journal of Biomechanical Engineering*, 127(4):709–15, August 2005.
- [10] S. D. Waldman and J. M. Lee. Effect of sample geometry on the apparent biaxial mechanical behaviour of planar connective tissues. *Biomaterials*, 26(35):7504–13, December 2005.
- [11] P. G. Charette. *A method for full-field mechanical testing of biological membranes based on electronic speckle pattern interferometry (ESPI)*. PhD thesis, McGill University, 1995.
- [12] P. M. Nielsen, D. T. Malcolm, P. J. Hunter, and P. G. Charette. Instrumentation and procedures for estimating the constitutive parameters of inhomogeneous elastic membranes. *Biomechanics and Modeling in Mechanobiology*, 1(3):211–8, December 2002.
- [13] M. S. Sacks. Biaxial mechanical evaluation of planar biological materials. *Journal of Elasticity: Soft Tissue Mechanics*, 61(1-3):199–246, 2000.
- [14] K.-J. Bathe. *Finite Element Procedures*. Prentice-Hall, 1995.
- [15] A. Makino, W. R. Hamburgren, and J. S. Fitch. Fluoroelastomer pressure pad design for microelectronic applications. Technical Report WRL-93/7, DEC Western Research Laboratory, Palo Alto, CA, November 1997. Available from: <http://www.hpl.hp.com/techreports/Compaq-DEC/WRL-93-7.pdf>.
- [16] J. Hildebrand, H. Fukaya, and C. Martin. Stress-strain relations of tissue sheets

- undergoing uniform two-dimensional stretch. *Journal of Applied Physiology*, 27:758–762, 1969.
- [17] A. Wineman, D. Wilson, and J. W. Melvin. Material identification of soft tissue using membrane inflation. *Journal of Biomechanics*, 12(11):841–50, 1979.
- [18] D. Mohan and J. W. Melvin. Failure properties of passive human aortic tissue. II—biaxial tension tests. *Journal of Biomechanics*, 16(1):31–44, January 1983.
- [19] J. N. Kinkaid, S. P. Marra, F. E. Kennedy, and M. F. Fillinger. Inflation testing as a means of measuring failure strength of aortic tissue. *Advances in Bioengineering, ASME Bioengineering Division BED Series*, 55:111–112, 2003.
- [20] L. Treloar. *The physics of rubber elasticity*. Oxford University Press, 1948.
- [21] R. Rivlin and D. Saunders. Large elastic deformations of isotropic materials, vii. Experiments on the deformation of rubber. *Philosophical Transactions of the Royal Society*, A243:251–288, 1951.
- [22] P. H. Chew, F. C. Yin, and S. L. Zeger. Biaxial stress-strain properties of canine pericardium. *Journal of Molecular and Cellular Cardiology*, 18(6):567–78, June 1986.
- [23] F. C. Yin, P. H. Chew, and S. L. Zeger. An approach to quantification of biaxial tissue stress-strain data. *Journal of Biomechanics*, 19(1):27–37, 1986.
- [24] F. C. Yin, R. K. Strumpf, P. H. Chew, and S. L. Zeger. Quantification of the mechanical properties of noncontracting canine myocardium under simultaneous biaxial loading. *Journal of Biomechanics*, 20(6):577–89, 1987.
- [25] Y. J. Zeng, D. Yager, and Y. C. Fung. Measurement of the mechanical properties of the human lung tissue. *Journal of Biomechanical Engineering*, 109(2):169–74, May 1987.
- [26] J. C. Debes and Y. C. Fung. Biaxial mechanics of excised canine pulmonary arteries. *American Journal of Physiology*, 269(2 Pt 2):H433–42, August 1995.

- [27] R. P. Vito. The role of the pericardium in cardiac mechanics. *Journal of Biomechanics*, 12(8):587–92, 1979.
- [28] J. D. Humphrey and F. C. Yin. On constitutive relations and finite deformations of passive cardiac tissue: I. a pseudostrain-energy function. *Journal of Biomechanical Engineering*, 109(4):298–304, November 1987.
- [29] H. S. Choi and R. P. Vito. Two-dimensional stress-strain relationship for canine pericardium. *J Biomech Eng*, 112(2):153–9, May 1990.
- [30] J. H. Jun, J. L. Harris, J. D. Humphrey, and S. Rastegar. Effect of thermal damage and biaxial loading on the optical properties of a collagenous tissue. *J Biomech Eng*, 125(4):540–8–, August 2003.
- [31] J. L. Harris, P. B. Wells, and J. D. Humphrey. Multiaxial thermal damage of collagenous membranes. In *Annual International Conference of the IEEE Engineering in Medicine and Biology - Proceedings*, volume 1, pages 713–714–, Houston, TX, United States, 2002. Institute of Electrical and Electronics Engineers Inc.
- [32] J. L. Harris, P. B. Wells, and J. D. Humphrey. Altered mechanical behavior of epicardium due to isothermal heating under biaxial isotonic loads. *J Biomech Eng*, 125(3):381–8, June 2003.
- [33] S. H. Lu, M. S. Sacks, S. Y. Chung, D. C. Gloeckner, R. Pruchnic, J. Huard, W. C. de Groat, and M. B. Chancellor. Biaxial mechanical properties of muscle-derived cell seeded small intestinal submucosa for bladder wall reconstitution. *Biomaterials*, 26(4):443–9, February 2005.
- [34] M. S. Sacks. A method for planar biaxial mechanical testing that includes in-plane shear. *Journal of Biomechanical Engineering*, 121(5):551–5, October 1999.
- [35] W. Sun, M. S. Sacks, T. L. Sellaro, W. S. Slaughter, and M. J. Scott. Biaxial mechanical response of bioprosthetic heart valve biomaterials to high in-plane shear. *Journal of Biomechanical Engineering*, 125(3):372–80, June 2003.

- [36] Instron Corporation. Planar biaxial soft tissue test system (Data sheet), 2004. Available from: <http://www.instron.com/wa/library/streamFile2.aspx?sdoc=461>.
- [37] S. P. Marra, K. T. Ramesh, and A. S. Douglas. Characterization and modeling of compliant active materials. *Journal of the Mechanics and Physics of Solids*, 51:1723–1743, 2003.
- [38] P. M. Nielsen, P. J. Hunter, and B. H. Smaill. Biaxial testing of membrane biomaterials: testing equipment and procedures. *J Biomech Eng*, 113(3):295–300, August 1991.
- [39] S. D. Waldman and J. M. Lee. Boundary conditions during biaxial testing of planar connective tissues. part 1: Dynamic behavior. *Journal of Materials Science: Materials in Medicine*, 13(10):933–938, 2002.
- [40] S. D. Waldman, M. S. Sacks, and J. M. Lee. Boundary conditions during biaxial testing of planar connective tissues: Part ii. fiber orientation. *Journal of Materials Science Letters*, 21(15):1215–1221, 2002.
- [41] P. G. Charette, I. W. Hunter, and P. J. Hunter. Large deformation mechanical testing of biological membranes using speckle interferometry in transmission. I: Experimental apparatus. *Applied Optics*, 36(10):2238–2245, April 1997.
- [42] P. G. Charette, I. W. Hunter, and P. J. Hunter. Large deformation mechanical testing of biological membranes using speckle interferometry in transmission. II: Finite element modeling. *Applied Optics*, 36(10):2246–2251, April 1997.
- [43] D. T. Malcolm, P. M. Nielsen, P. J. Hunter, and P. G. Charette. Strain measurement in biaxially loaded inhomogeneous, anisotropic elastic membranes. *Biomechanics and Modeling in Mechanobiology*, 1(3):197–210, December 2002.
- [44] Futek Advanced Sensor Technology, Inc. Futek Model MAU300 stick shift / gear shift knob load cell (Data sheet), 2005. Available from: <http://futek.com/files/acrobat/11070.pdf>.

- [45] Futek Advanced Sensor Technology, Inc. Futek Model LSB200 S-Beam Junior load cell (Data sheet), 2005. Available from: <http://futek.com/files/acrobat/12357.pdf>.
- [46] W. Young and R. Budynas. *Roark's Formulas for Stress and Strain*. McGraw-Hill, New York, 7 edition, 2002.
- [47] Vishay Micro-Measurements. Force and Torque Measurement, 2000. Available from: <http://www.measurementsgroup.com/guide/ta/ftm/ftm.htm>.
- [48] Vishay Micro-Measurements. Strain gage based transducers: their design and construction, 2005. Available from: http://vishay.com/brands/measurements_group/guide/ta/sGBT/sGBTindex.htm.
- [49] Apogee Instruments. Alta U10 high performance cooled CCD camera system. Data sheet, 2005. Available from: <http://www.ccd.com/U10.pdf>.
- [50] Carl Zeiss (Photoobjektive). Apo-Makro-Planar T* 4/120 (Data sheet), 1999. Available from: <http://www.zeiss.de/>.
- [51] Aerotech Inc. ATS125 Series Mechanical Bearing, Ball-Screw Stage (Data sheet), 2005. Available from: <http://www.aerotech.com/products/pdf/ats125.pdf>.
- [52] Aerotech Inc. ANT-25L/-50L Mechanical Bearing, Linear Motor Stage (Data sheet), 2005. Available from: <http://www.aerotech.com/products/pdf/ANT25L.pdf>.
- [53] Aerotech Inc. *A3200 Nview Help (Online documentation)*, October 2005.
- [54] Vishay Micro-Measurements. C2A Series Strain Gages (Data sheet), 2004. Available from: <http://www.davidson.com.au/products/strain/mg/gauges/pdf/c2a.pdf>.
- [55] J. Fraden. *Handbook of modern sensors*, page 325. AIP Press, 2 edition, 1997.
- [56] Measurements Group, Raleigh, NC. *Strain gage based transducers*, 1988.

- [57] US Department of Defense. *Military Handbook - MIL-HDBK-5H: Metallic Materials and Elements for Aerospace Vehicle Structures*, Knovel Interactive edition, July 2003. Available from: <http://www.knovel.com/knovel12/Toc.jsp?SpaceID=88&BookID=754>.
- [58] J. G. Kaufman. *Aluminum Alloy Database*. Knovel, 2004. Available from: <http://www.knovel.com/knovel12/Toc.jsp?BookID=844&VerticalID=0>.
- [59] T. A. Fofonoff. Brain microelectrode array systems. Master's thesis, Massachusetts Institute of Technology, February 2003.
- [60] Vishay Micro-Measurements. Surface preparation for strain gage bonding, 2004. Available from: http://www.vishay.com/brands/measurements_group/guide/ib/b129/129index.htm.
- [61] Vishay Micro-Measurements. M-Bond AE-15 Adhesive (Data sheet), 2005. Available from: http://www.vishay.com/brands/measurements_group/guide/a110/acc/mbae15.htm.
- [62] Vishay Foil Resistors. H Series Bulk Metal Foil Technology hermetically sealed resistors, metrology/laboratory (Data sheet), 2005. Available from: <http://www.vishay.com/docs/63006/hmetlab.pdf>.
- [63] Calex Corporation. Model 162MK Bridgesensor (Data sheet), 2001. Available from: <http://www.calex.com/pdf/162mk.pdf>.
- [64] Vishay Dale. PTF Metal Film Resistors (Data sheet), 2005. Available from: <http://www.vishay.com/doc?31019>.
- [65] National Instruments. High Accuracy M Series Multifunction DAQ. (Data sheet), 2005. Available from: http://www.ni.com/pdf/products/us/04_4064_628x_MSeries.pdf.
- [66] ANSYS, Inc., (Canonsburg, PA). *ANSYS, Inc. Theory Reference: ANSYS Release 9.0*, 2004. Available from: http://www1.ansys.com/customer/content/documentation/90/ansys/a_thry90.pdf.

- [67] J. Oden and W. Kubitza. Numerical analysis of nonlinear pneumatic structures. In *Proc. 1st Int. Colloquium on Pneumatic Structures*, pages 87–107. Technische Hochschule, Stuttgart, May 1967.
- [68] McMaster-Carr online catalog product detail. Part Number: 85995K32. Last accessed, 2005. Available from: <http://www.mcmaster.com/>.
- [69] Apogee Instruments. Alta U4000 High-Performance Cooled Camera System. (Data sheet), 2005. Available from: <http://www.ccd.com/U4000.pdf>.

Appendix A

Mechanical drawings

The following pages provide mechanical drawings of selected custom-machined components of the multiaxial testing system. Complete details, including dimensions of components not shown here, may be found in electronic files archived with the thesis.

<i>Transducer Body</i>	
Material:	Aluminum 2024 T4
Drawing Scale:	2:1
All Dimensions in mm	

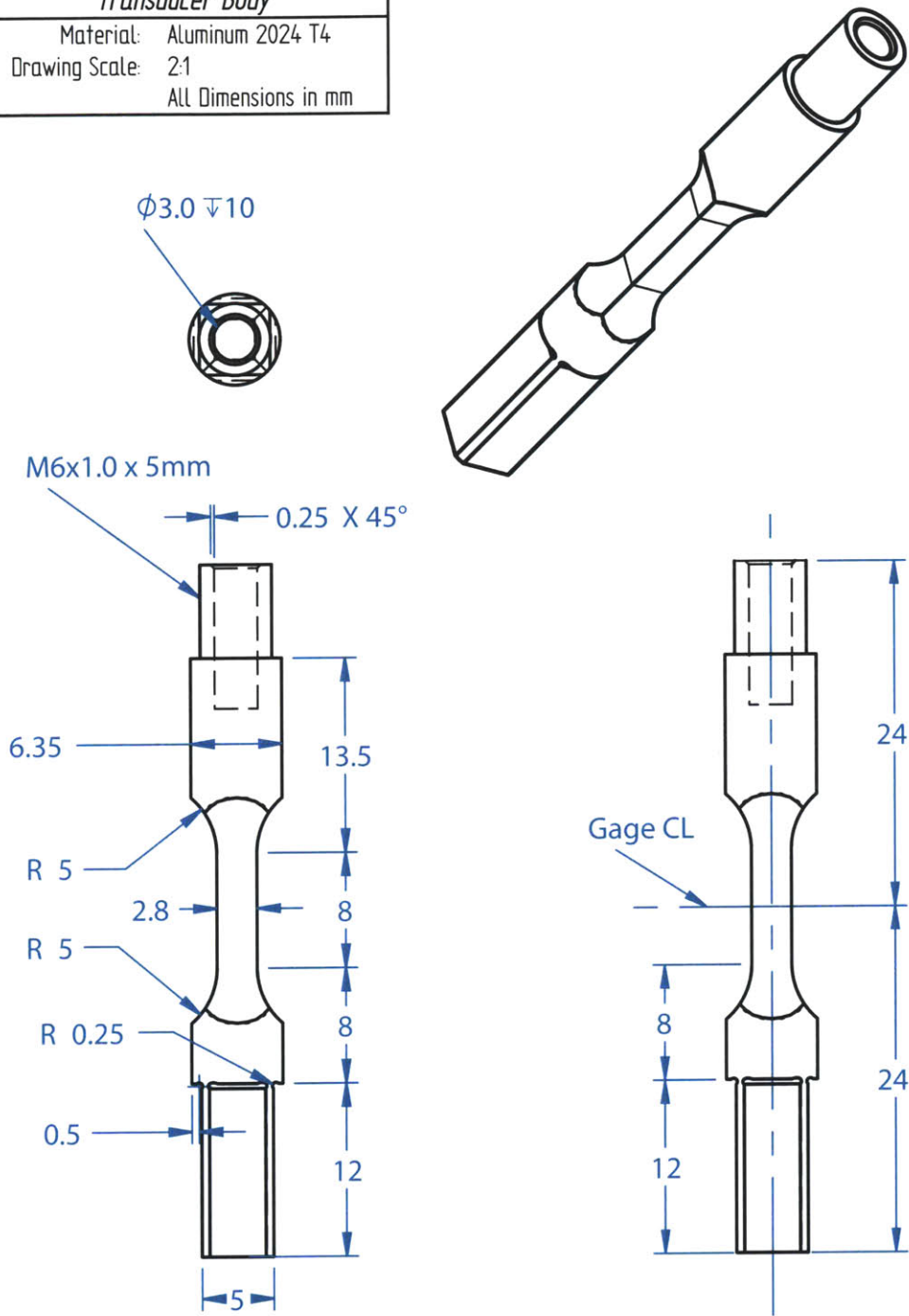


Figure A-1. Mechanical schematic: transducer body.

<i>Pin Holder — 7 mm</i>	
Material:	Stainless Steel 17-4PH
Drawing Scale:	5:1
All Dimensions in mm	

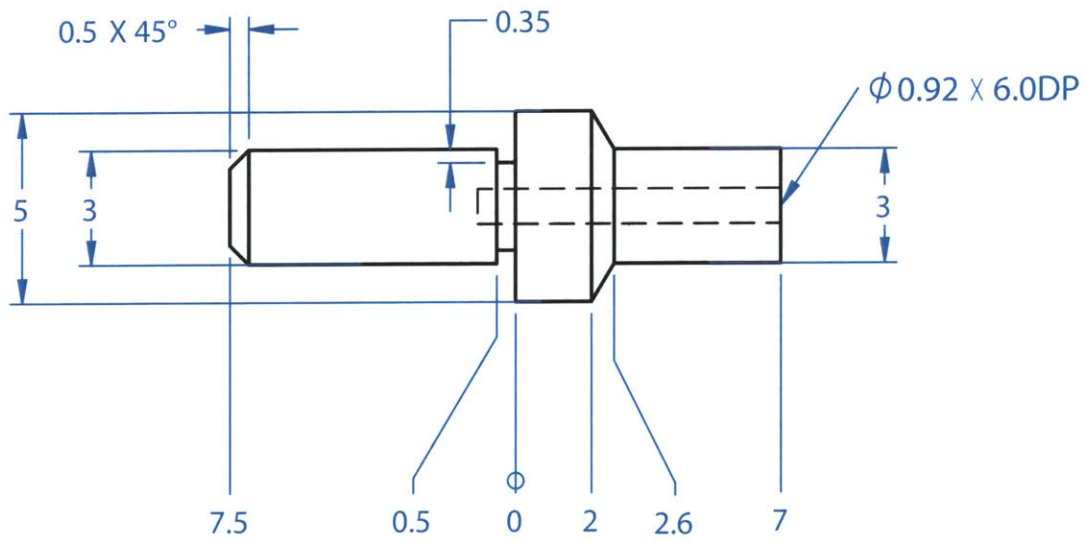
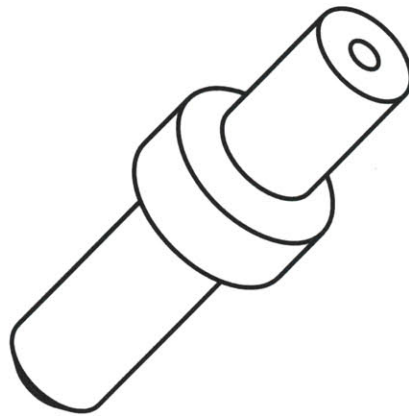


Figure A-2. Mechanical schematic: pin holder (7mm height).

<i>Pin Holder Collet</i>	
Material:	Black Delrin
Drawing Scale:	5:1
All Dimensions in mm	

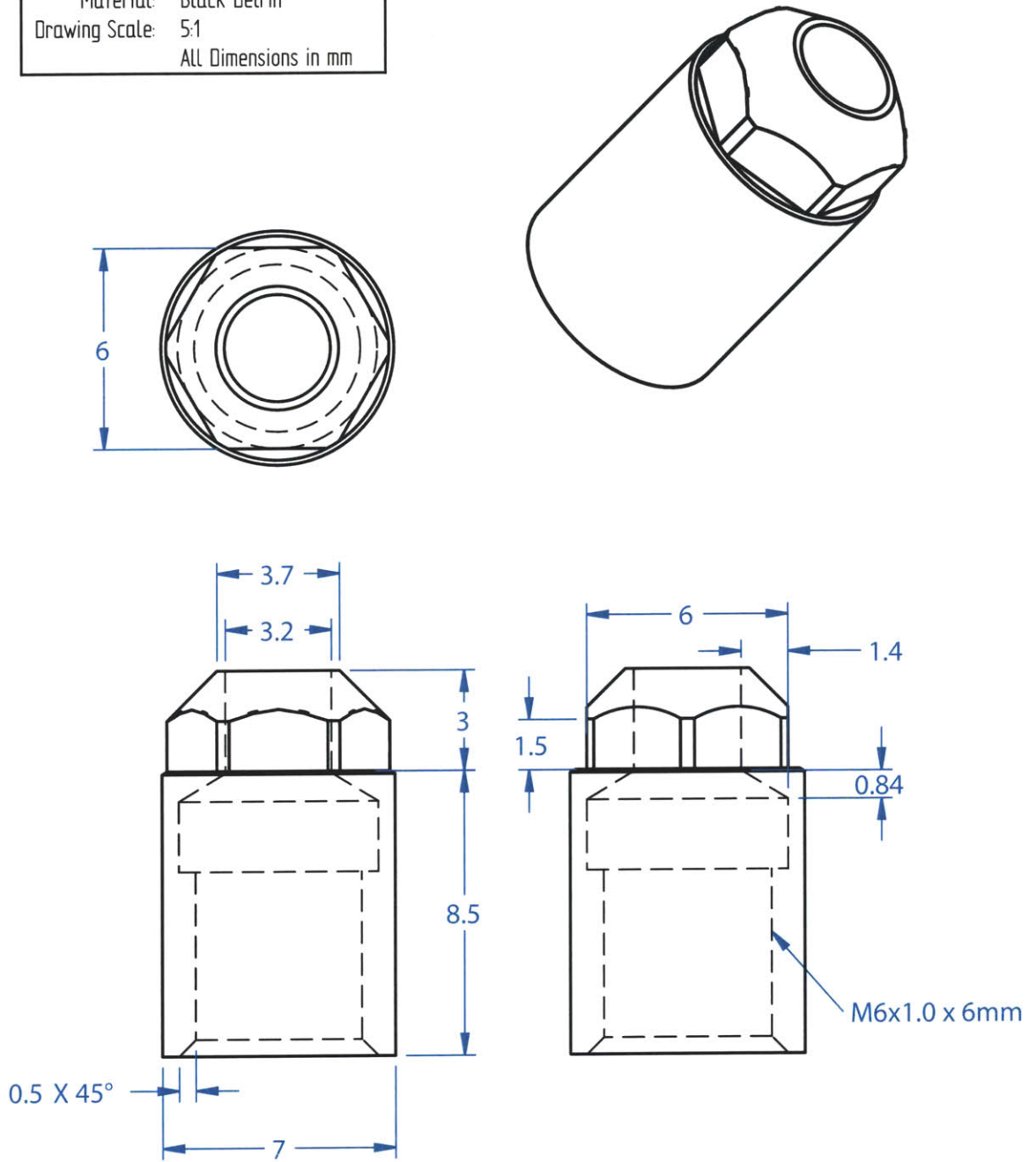


Figure A-3. Mechanical schematic: pin holder collet.

<i>Transducer Holder</i>	
Material:	Aluminum 6061
Drawing Scale:	1:2
ALL Dimensions in mm	

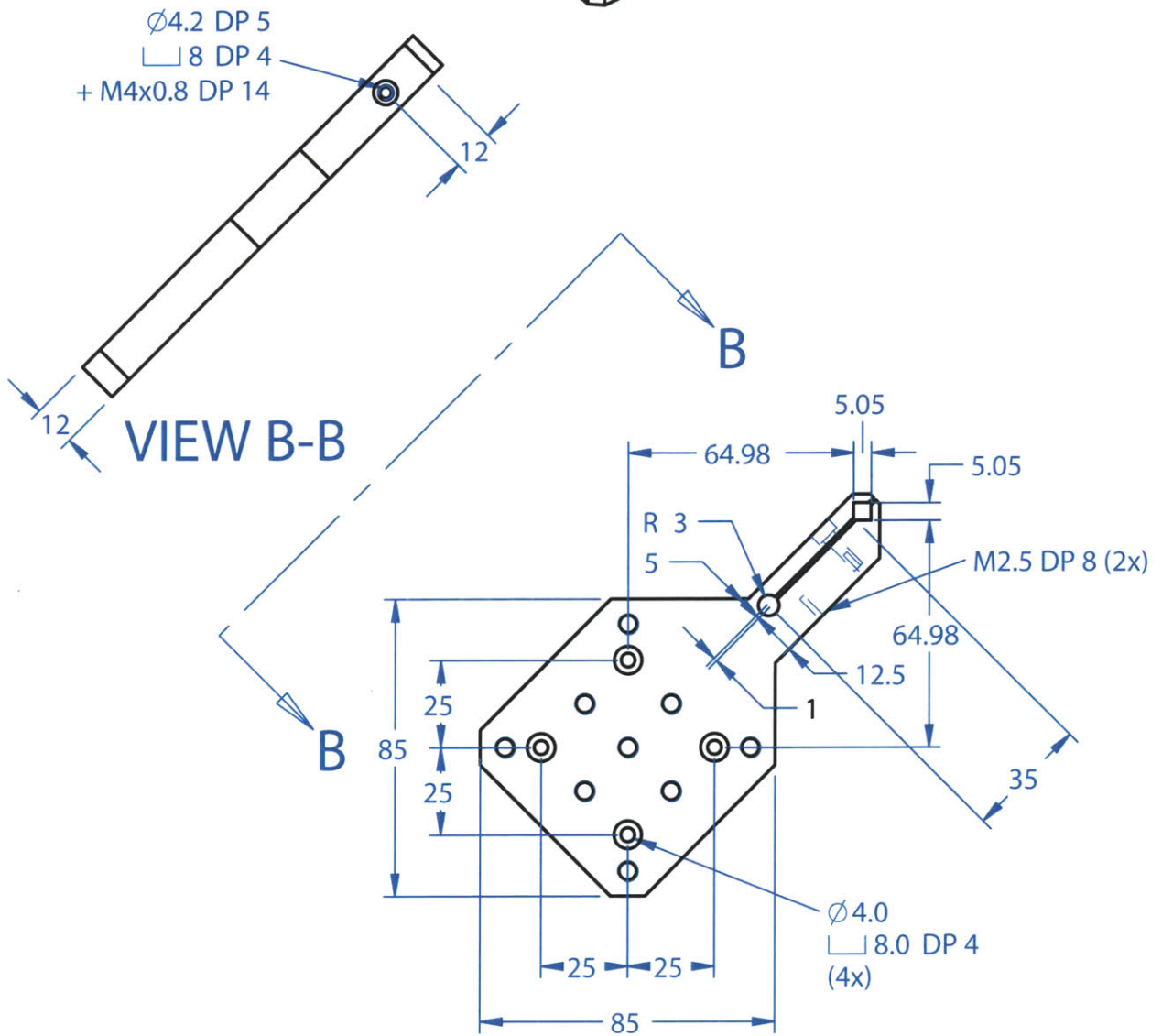
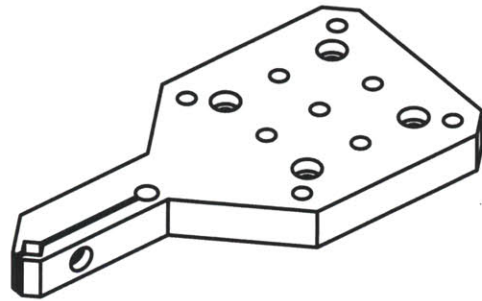


Figure A-4. Mechanical schematic: transducer holder.

<i>Gage Mounting Assembly Base</i>	
Material:	Aluminum 6061
Drawing Scale:	2:1
ALL Dimensions in mm	

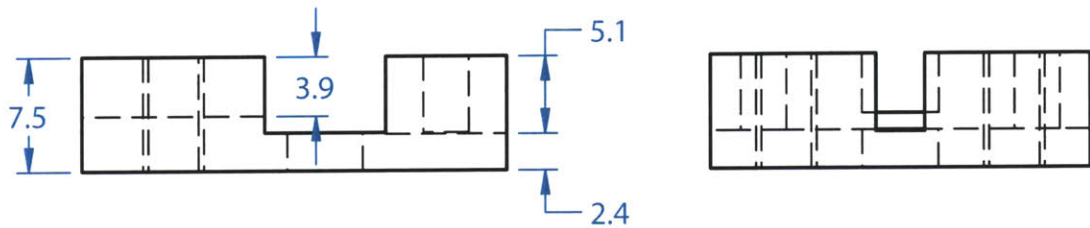
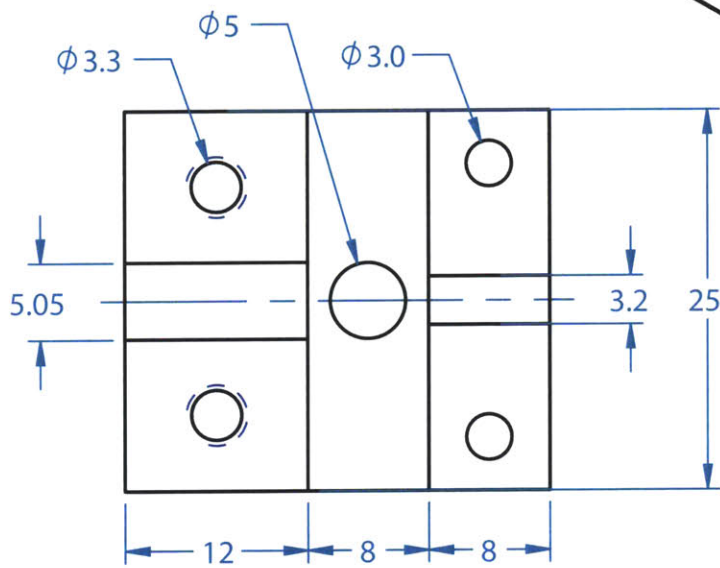
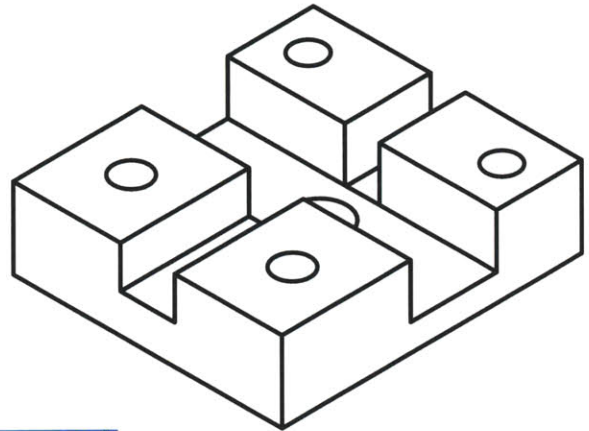
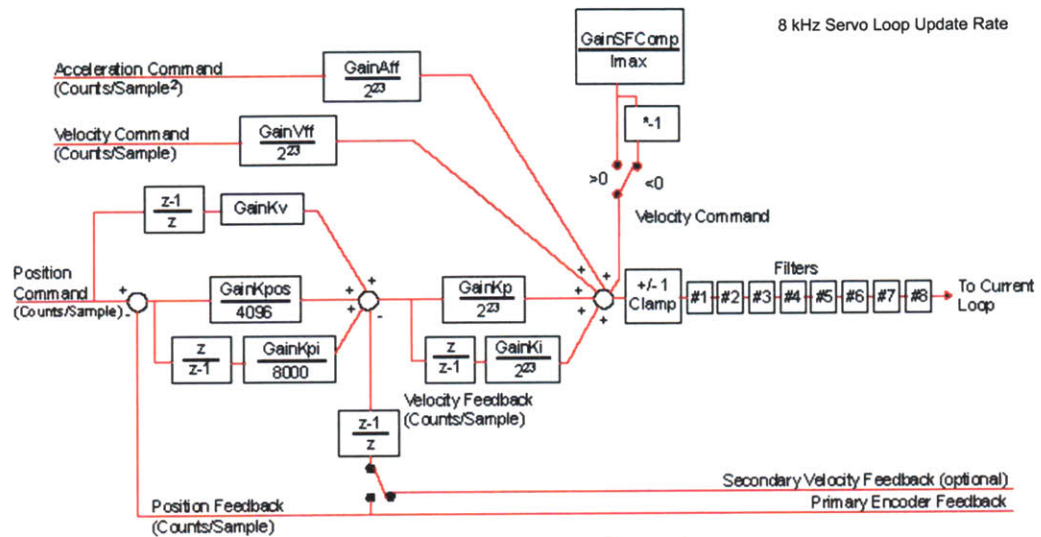


Figure A-5. Mechanical schematic: strain gage mounting jig-base.

Appendix B

Motion system control loop



Servo Loop

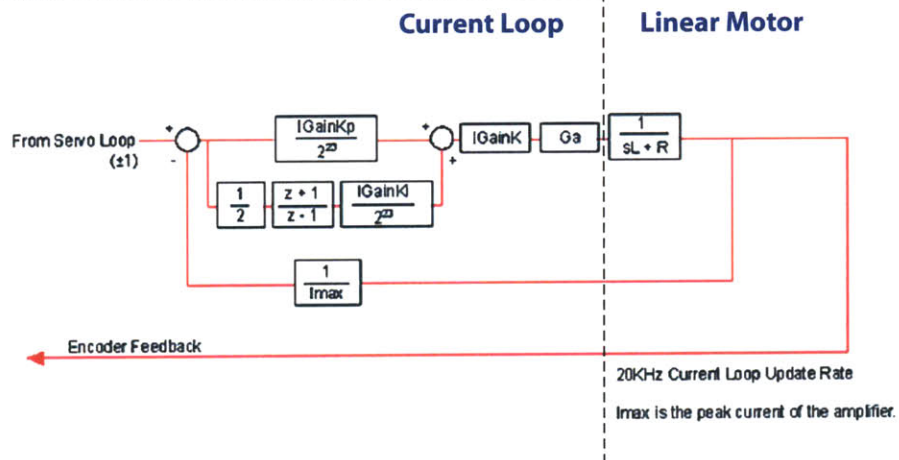


Figure B-1. Detail of control loop configuration for the motion stages. The servo loop computes an output current from motion profile and feedback data and updates at 8kHz; the faster current loop within the amplifier tracks the commanded current from the servo loop stage. Figure components from [53].

Servo Parameter	As delivered	Nparam wizard output(*)	After manual tuning
K_{pos}	67	72.8	124
K_i	120	160	2400
K_p	7300	8800	24000
K_v	2700	—	12000
A_{ff}	2700	—	8800
V_{ff}	0	—	0

(*)Nparam wizard inputs:

1.8 kg mass; 100 Hz crossover, 30° phase margin goal

All parameters for x axis.

Table B.1. Motion control servo loop parameters before and after tuning for improved dynamic performance. *Wizard* values output from the Aerotech utility software failed to deliver the requested performance. 1.8 kg mass = 400 g moving stage + 800 g complete y -axis linear stage + 600 g load (transducer, signal conditioning unit, and associated hardware).

Appendix C

Transducer design calculations

The following page contains a table of selected combinations of transducer element dimensions, amplifier gain, bridge excitation voltage, and transducer load capacity to produce full-scale amplified outputs corresponding to several input ranges available on the data acquisition card ($\pm 1, 2, 5, 10$ V). Highlighted rows indicate the parameters used for the final transducer element design, with the initially targeted gain value ($G = 2002$ with $R_g = 50 \Omega$) and with the gain available with the lowest temperature-coefficient resistor eventually used ($G = 835$ with $R_g = 120 \Omega$). Note that for a steel transducer with ~ 2.7 times the elastic modulus (E) of aluminum, the transducer width (h) must be nearly 30% less to maintain the same strain at a given transducer length (bottom group of rows). The governing equations are given in Section 3.2.3.

Amplifier output (full scale) (V)	Bridge excitation voltage (V)	Transducer material modulus (N/mm ²)	Maximum strain	Gage factor	Half bridge output at full scale (V)	Stress at full scale (N/mm ²)	Transducer element width (mm)	Bending moment from applied load (N-mm)	Moment arm for applied load (mm)	Transducer load for full-scale output (N)	Gain setting resistor (Ω)	Amplifier gain
V_{amp}	V_{exc}	E	ϵ_{max}	G	V_{out}	σ_{max}	h	M	l	F	R_g	G_a
2.0	5.00	7.31E+04	1.91E-04	2.095	9.99E-04	1.39E+01	2.50	3.63E+01	36.31	1.00	50.00	2002.0
5.0	5.00	7.31E+04	4.77E-04	2.095	2.50E-03	3.49E+01	2.50	9.08E+01	45.39	2.00	50.00	2002.0
10.0	5.00	7.31E+04	9.54E-04	2.095	5.00E-03	6.97E+01	2.50	1.82E+02	36.31	5.00	50.00	2002.0
10.0	5.00	7.31E+04	9.54E-04	2.095	5.00E-03	6.97E+01	2.50	1.82E+02	18.16	10.00	50.00	2002.0
2.0	5.00	7.31E+04	1.91E-04	2.095	9.99E-04	1.39E+01	3.00	6.27E+01	62.74	1.00	50.00	2002.0
5.0	5.00	7.31E+04	4.77E-04	2.095	2.50E-03	3.49E+01	3.00	1.57E+02	78.43	2.00	50.00	2002.0
10.0	5.00	7.31E+04	9.54E-04	2.095	5.00E-03	6.97E+01	3.00	3.14E+02	62.74	5.00	50.00	2002.0
10.0	5.00	7.31E+04	9.54E-04	2.095	5.00E-03	6.97E+01	3.00	3.14E+02	31.37	10.00	50.00	2002.0
1.0	5.00	7.31E+04	1.91E-04	2.095	9.98E-04	1.39E+01	2.855	5.40E+01	54.02	1.00	100.00	1002.0
2.0	5.00	7.31E+04	3.81E-04	2.095	2.00E-03	2.79E+01	2.855	1.08E+02	54.02	2.00	100.00	1002.0
5.0	5.00	7.31E+04	9.53E-04	2.095	4.99E-03	6.96E+01	2.855	2.70E+02	54.02	5.00	100.00	1002.0
5.0	5.00	7.31E+04	9.53E-04	2.095	4.99E-03	6.96E+01	2.855	2.70E+02	27.01	10.00	100.00	1002.0
1.0	5.00	7.31E+04	2.29E-04	2.095	1.20E-03	1.67E+01	2.795	6.08E+01	60.80	1.00	120.00	835.3
2.0	5.00	7.31E+04	4.57E-04	2.095	2.39E-03	3.34E+01	2.795	1.22E+02	60.80	2.00	120.00	835.3
5.0	5.00	7.31E+04	1.14E-03	2.095	5.99E-03	8.35E+01	2.795	3.04E+02	60.80	5.00	120.00	835.3
5.0	5.00	7.31E+04	1.14E-03	2.095	5.99E-03	8.35E+01	2.795	3.04E+02	30.40	10.00	120.00	835.3
1.0	4.00	7.31E+04	2.86E-04	2.095	1.20E-03	2.09E+01	2.795	7.60E+01	76.00	1.00	120.00	835.3
2.0	4.00	7.31E+04	5.71E-04	2.095	2.39E-03	4.18E+01	2.795	1.52E+02	76.00	2.00	120.00	835.3
5.0	4.00	7.31E+04	1.43E-03	2.095	5.99E-03	1.04E+02	2.795	3.80E+02	76.00	5.00	120.00	835.3
5.0	4.00	7.31E+04	1.43E-03	2.095	5.99E-03	1.04E+02	2.795	3.80E+02	38.00	10.00	120.00	835.3
1.0	4.00	7.31E+04	1.19E-04	2.095	5.00E-04	8.71E+00	2.795	3.17E+01	31.00	1.02	50.00	2002.0
2.0	4.00	7.31E+04	2.38E-04	2.095	9.99E-04	1.74E+01	2.795	6.34E+01	31.00	2.05	50.00	2002.0
5.0	4.00	7.31E+04	5.96E-04	2.095	2.50E-03	4.36E+01	2.795	1.59E+02	31.00	5.12	50.00	2002.0
10.0	4.00	7.31E+04	1.19E-03	2.095	5.00E-03	8.71E+01	2.795	3.17E+02	31.00	10.23	50.00	2002.0
1.0	5.00	7.31E+04	2.29E-04	2.095	1.20E-03	1.67E+01	2.795	6.08E+01	31.00	1.96	120.00	835.3
2.0	5.00	7.31E+04	4.57E-04	2.095	2.39E-03	3.34E+01	2.795	1.22E+02	31.00	3.92	120.00	835.3
5.0	5.00	7.31E+04	1.14E-03	2.095	5.99E-03	8.35E+01	2.795	3.04E+02	31.00	9.81	120.00	835.3
10.0	5.00	7.31E+04	2.29E-03	2.095	1.20E-02	1.67E+02	2.795	6.08E+02	62.00	9.81	120.00	835.3
1.0	5.00	1.96E+05	2.29E-04	2.095	1.20E-03	4.48E+01	2.005	6.02E+01	31.00	1.94	120.00	835.3
2.0	5.00	1.96E+05	4.57E-04	2.095	2.39E-03	8.96E+01	2.005	1.20E+02	31.00	3.88	120.00	835.3
5.0	5.00	1.96E+05	1.14E-03	2.095	5.99E-03	2.24E+02	2.005	3.01E+02	31.00	9.71	120.00	835.3
10.0	5.00	1.96E+05	2.29E-03	2.095	1.20E-02	4.48E+02	2.005	6.02E+02	62.00	9.71	120.00	835.3

Table C.1. Transducer dimensioning calculations

Appendix D

Transducer calibration details

D.1 Computation of the transformation matrix

From theoretical considerations of the transducer response and as shown experimentally in Section 5.1.1, the response of each transducer axis to an in-plane force F may be described as a sinusoid:

$$V_{out} = AF \cos(\theta - \phi), \quad (\text{D.1})$$

where A is the sensitivity amplitude, θ is the angle of the force with respect to the x axis, and ϕ is the angular offset of the sensitivity vector from the x axis.

Each transducer output may also be represented as the linear combination of responses to the components of applied force in the plane:

$$T_{ij} = c_{ijx}F_x + c_{ijy}F_y, \quad (\text{D.2})$$

where T_{ij} is the voltage output of axis j of two-axis transducer i ; F_x and F_y are the components of the applied load in the x and y axes; and c_{ijx} and c_{ijy} are the sensitivity terms for x and y axis loading, respectively. Considering both axes of the transducer, we have a system of linear equations:

$$\begin{bmatrix} T_{i1} \\ T_{i2} \end{bmatrix} = \begin{bmatrix} c_{i1x} & c_{i1y} \\ c_{i2x} & c_{i2y} \end{bmatrix} \begin{bmatrix} F_x \\ F_y \end{bmatrix}, \quad (\text{D.3})$$

where the matrix of c_{ijw} terms may be called the *sensitivity matrix*, C_i , for transducer i . Restated in matrix form,

$$T_i = C_i F. \quad (\text{D.4})$$

The terms of C_i are the linear coefficients computed from the calibration data of both outputs in response to loads in both axes. Knowing all the terms, one may solve this linear system or simply invert the C_i matrix to compute the force given the transducer outputs:

$$F = C_i^{-1}T_i. \tag{D.5}$$

In practice, the matrix $S = C_i^{-1}$ only needs to be computed once from the calibration coefficients. The elements of S may then be used to multiply the transducer outputs for real time control with no practical impact on performance.

D.2 Calibration data

The following pages present complete calibration data for the two final transducers that were characterized and used in the initial experiments. Response at each output to loads in both x and y axes is presented and analyzed separately. Graphical analysis of the residuals is included for both linear and quadratic fits to the data. In no case does the quadratic form substantially improve the quality of fit to the data over the linear form; therefore the use of a single linear sensitivity value for each transducer output–loading axis combination is justified.

Note: in the output term T_{ij} , i indexes the transducer unit; j indexes the output (among two outputs per transducer). For example, T_{12} is the output from the second channel of the first transducer, which is sensitive primarily in the y axis as seen from the data presented here and (in more compact form) in Section 5.1.2.

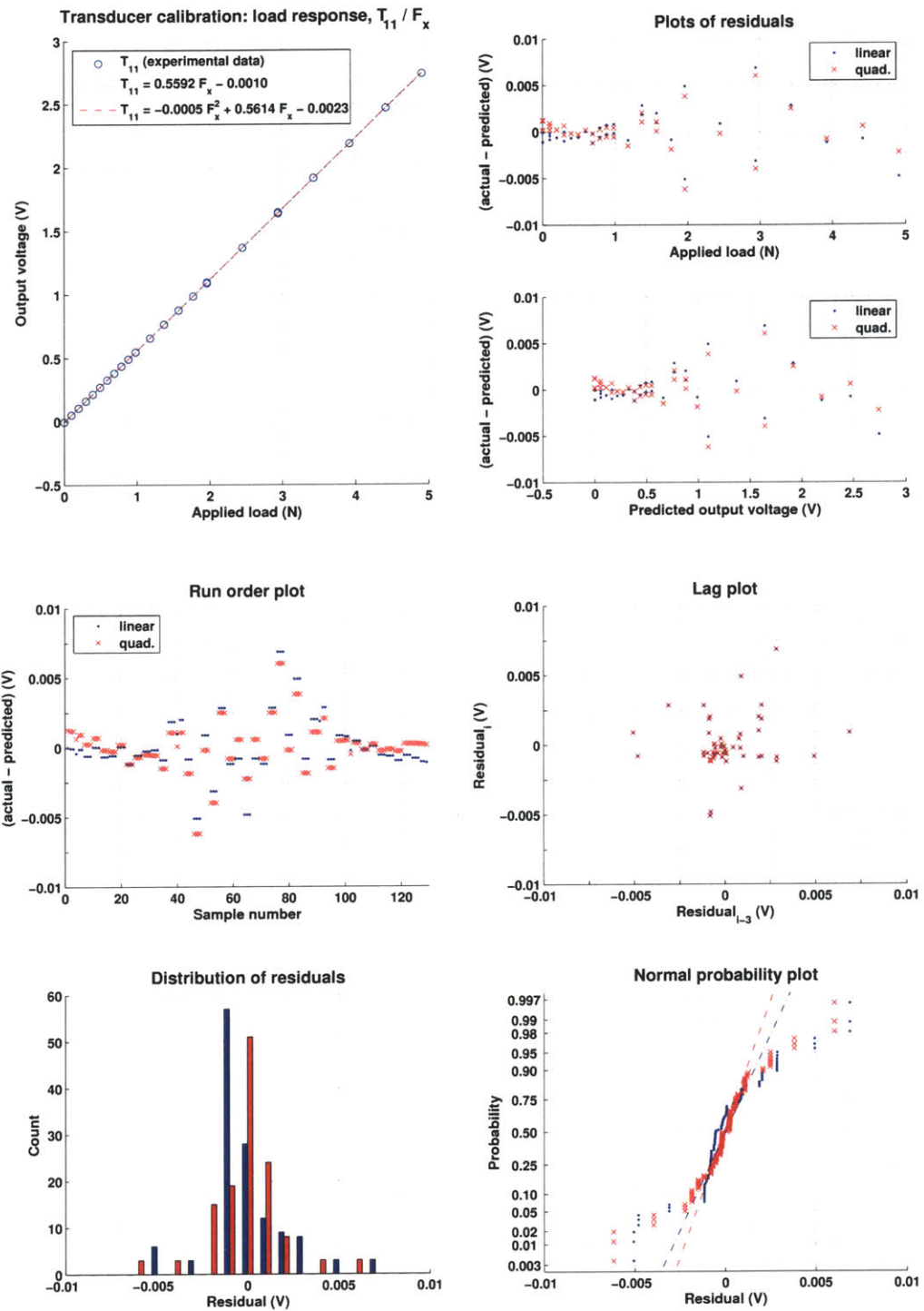


Figure D-1. Calibration data details: transducer 1, output 1, X axis load.

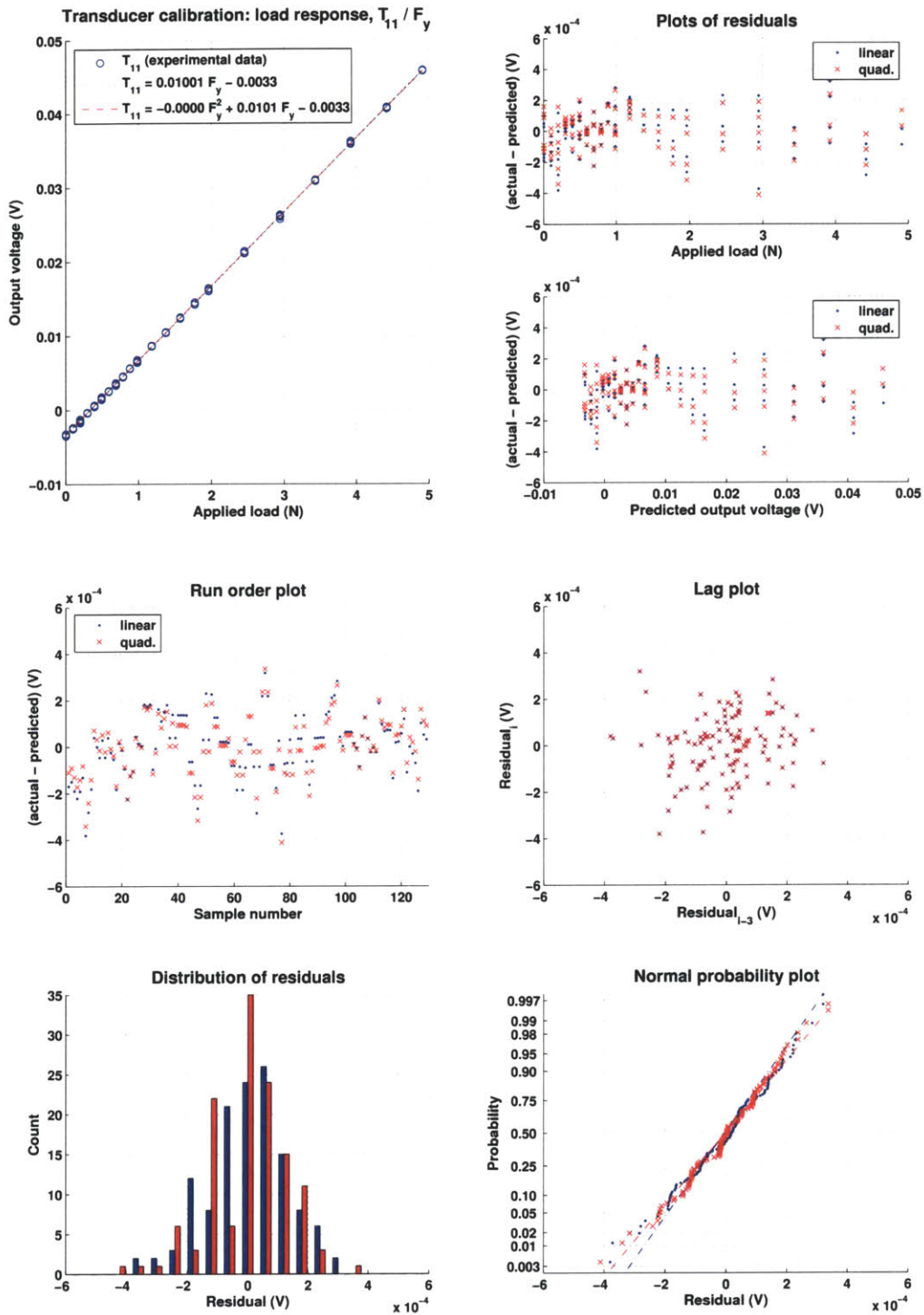


Figure D-2. Calibration data details: transducer 1, output 1, Y axis load.

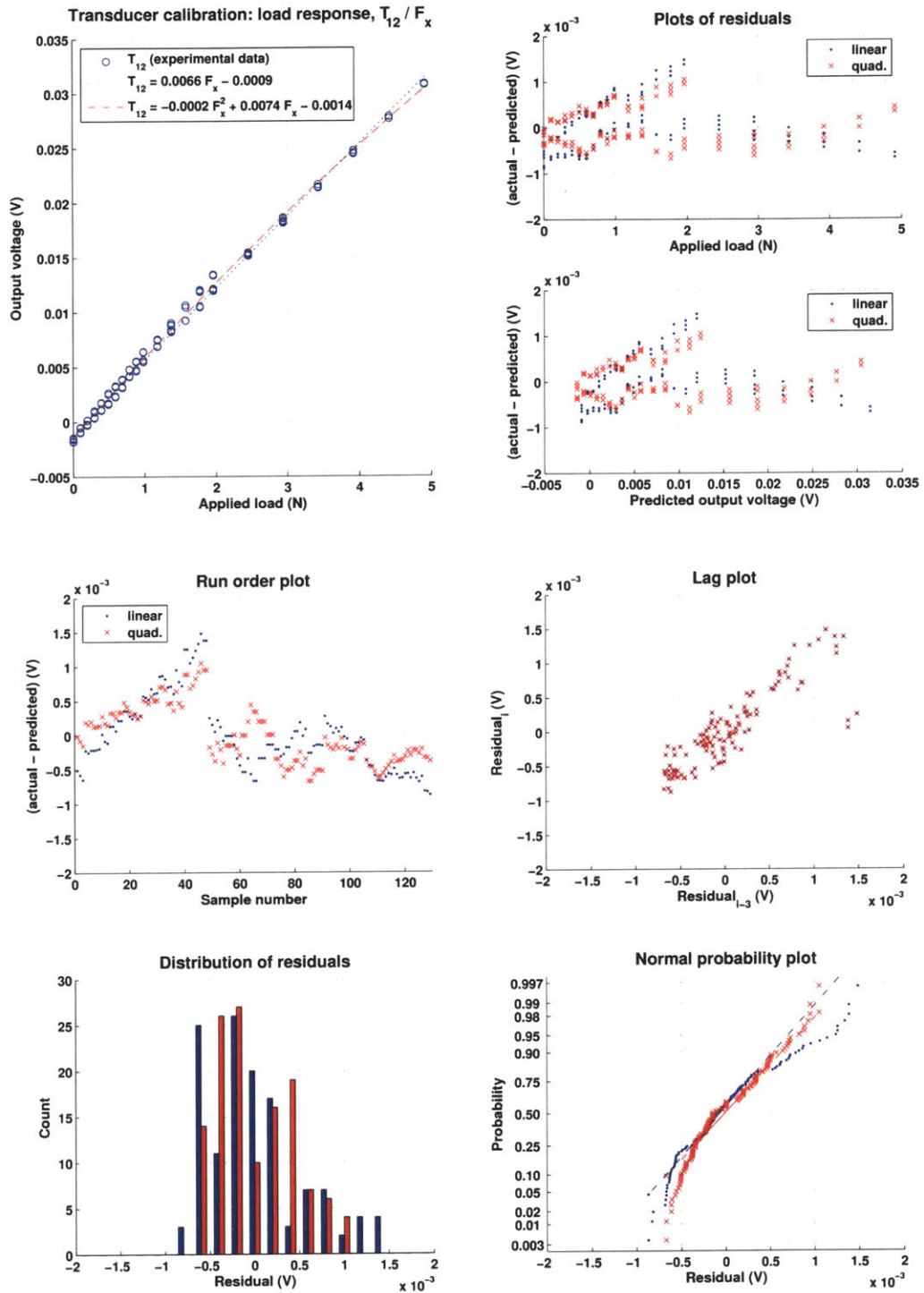


Figure D-3. Calibration data details: transducer 1, output 2, X axis load.

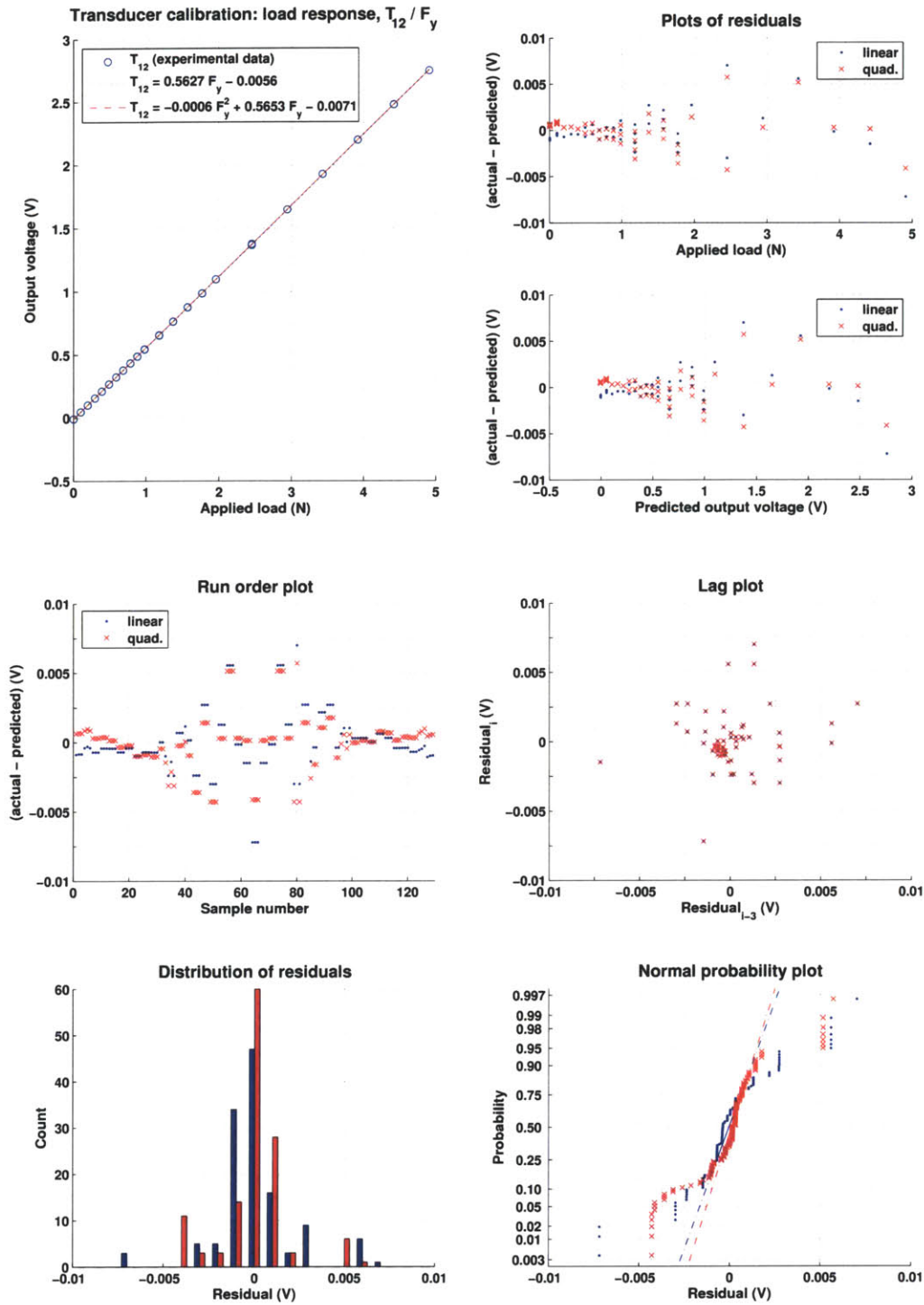


Figure D-4. Calibration data details: transducer 1, output 2, Y axis load.

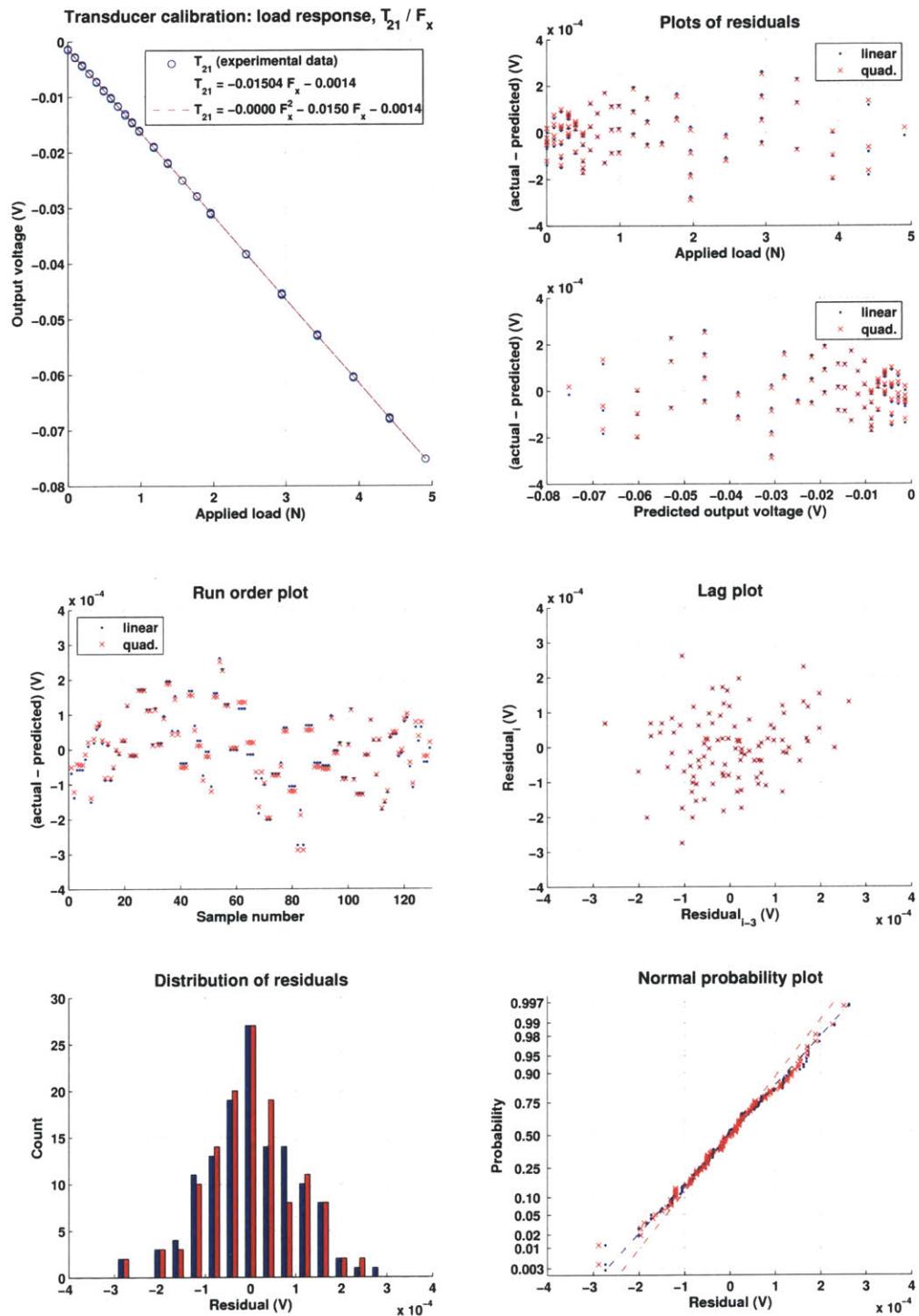


Figure D-5. Calibration data details: transducer 2, output 1, X axis load.

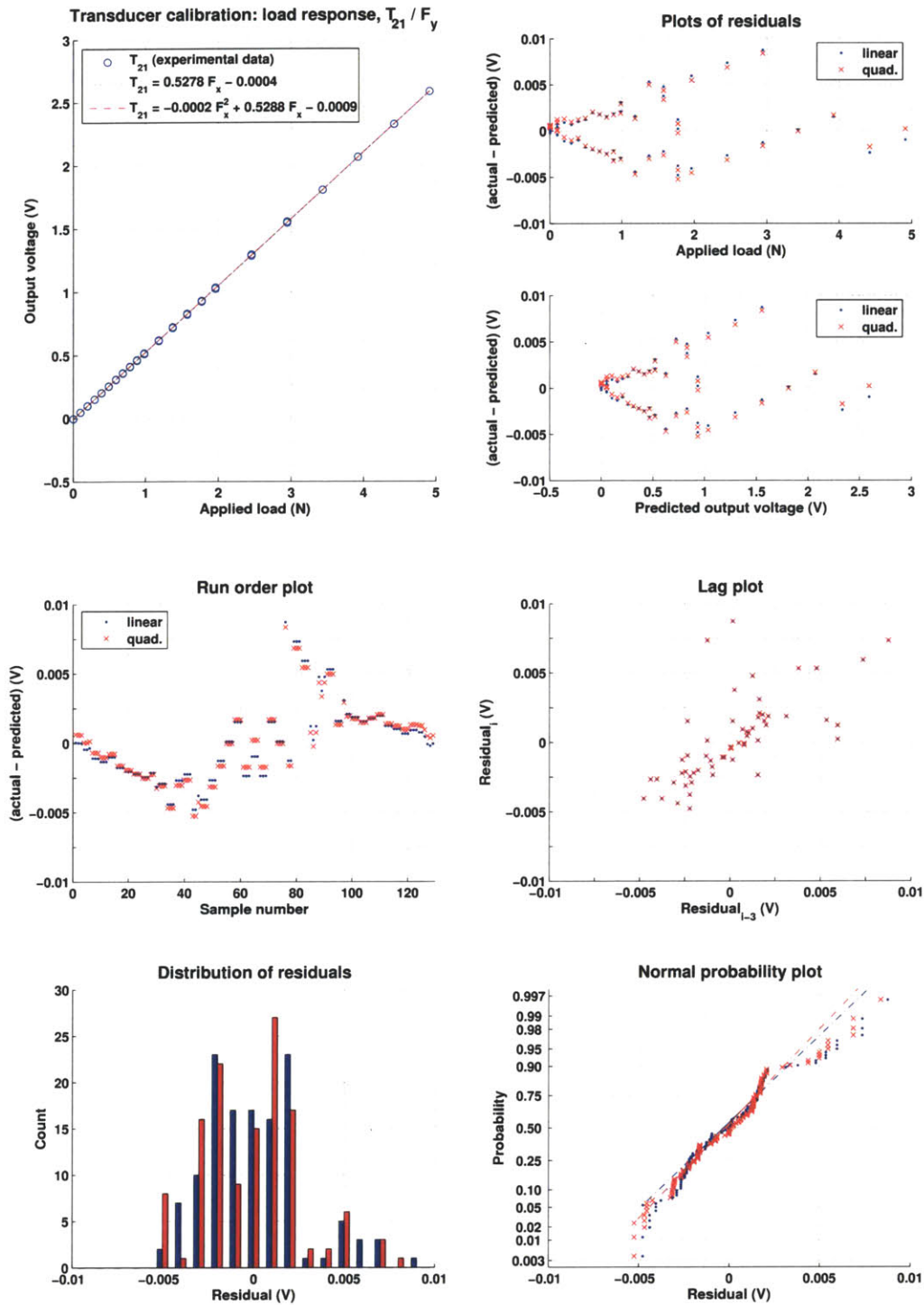


Figure D-6. Calibration data details: transducer 2, output 1, Y axis load.

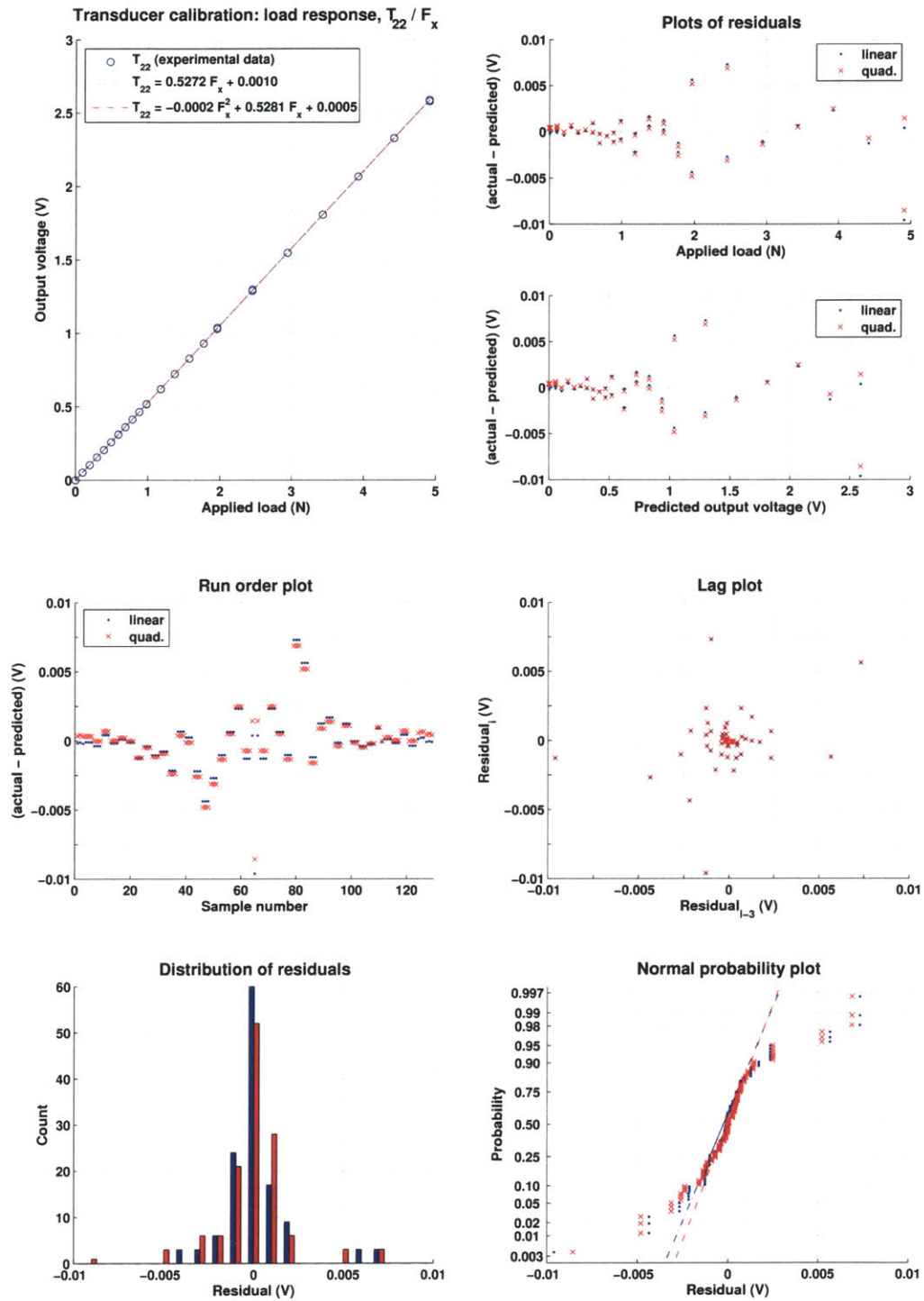


Figure D-7. Calibration data details: transducer 2, output 2, X axis load.

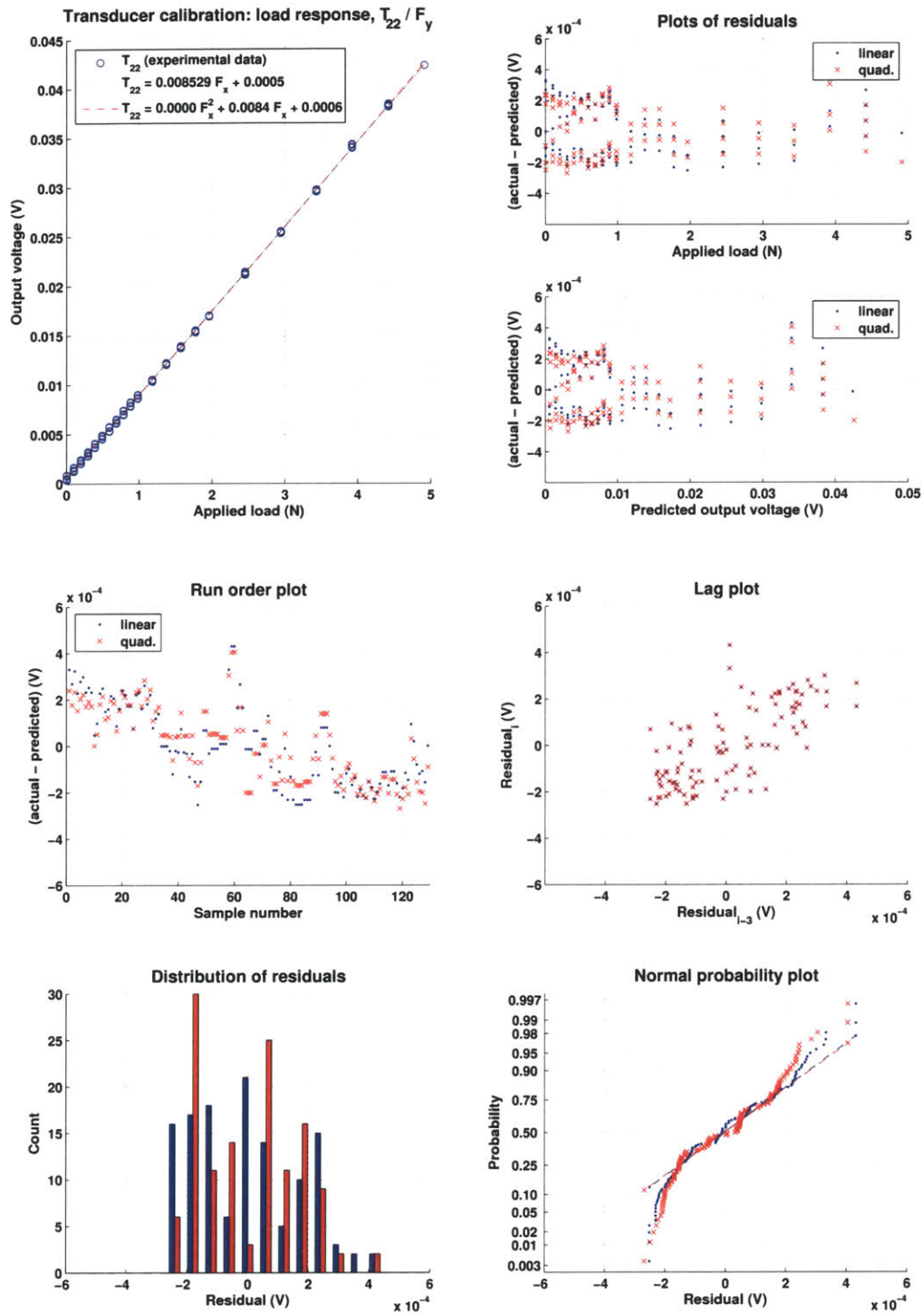


Figure D-8. Calibration data details: transducer 2, output 2, Y axis load.

Appendix E

Camera system comparison

Appendix F

Software code

F.1 Position transfer function computation

The following MATLAB function computes the magnitude and phase of the position loop response for the Aerotech linear motion stages, from the magnitude and phase of the current loop response. The latter is output from the A3200 Loop Transmission utility, while the former is desirable from a physical perspective (Section4.3.1).

```
function [posTF,CposTF] = positionTF(inputTF)

% POSITIONTF - Computes magnitude and phase of position loop
% transfer function from current loop transfer function data.
%
% posTF = positionTF(inputTF)
% [posTF,CposTF] = positionTF(inputTF)
%
% Inputs:   inputTF - N-by-3 array with following columns:
%           1: frequency
%           2: magnitude (dB)
%           3: phase (degrees)
%
% Outputs:  posTF - N-by-3 array with same fields as inputTF
%           CposTF (optional) - complex-valued vector of output TF

% Check input vector size
%
s = size(inputTF);
if length(s) ~= 2 | s(2) ~= 3
    error('input should be N-by-3 array')
end

% Initialize output array, break out input vectors
%
posTF = zeros(s);
mag0 = inputTF(:,2);
phase0 = inputTF(:,3);

% Construct complex response from magnitude and phase inputs
%
mag = 10.^(mag0./20);
reM = mag.*cos(phase0*pi/180);
imM = mag.*sin(phase0*pi/180);
zMag = complex(reM,imM);
```

```
% Construct closed-loop transfer function value, extract magnitude + phase
%
CposTF = zMag./(zMag-1);
magPosTF = abs(CposTF);
magPosTF = 20*log(magPosTF)./log(10);    % magnitude (dB)
phasePosTF = angle(CposTF)*(180/pi);    % phase angle (degrees)
phasePosTF = phasePosTF - 180;          % should have -360<phase<0...

% Construct output array
posTF(:,1) = inputTF(:,1);
posTF(:,2) = magPosTF;
posTF(:,3) = phasePosTF;
```
